Studying individual magnetic nanoparticles with X-ray PEEM

Inauguraldissertation

zur

Erlangung der Würde eines Doktors der Philosophie

vorgelegt der

Philosophisch-Naturwissenschaftlichen Fakultät

der Universität Basel

von

Ana-Maria Balan

aus Iaşi (Rumänien)

Basel, 2014

Genehmigt von der Philosophisch-Naturwissenschaftlichen Fakultät

auf Antrag von

Fakultätsverantwortlicher: Prof. Dr. Frithjof Nolting

Korreferent: Prof. Dr. Ernst Meyer

Basel, 16.09.2014

Prof. Dr. Jörg Schibler

Abstract

The thesis addresses a subject with broad implications in various scientific and technical areas. It presents unique direct observations of the magnetic state of *single* particles of iron (Fe), cobalt (Co) and nickel (Ni) with nanoscopic dimensions by means of spatially-resolved X-ray magnetic circular dichroism (XMCD). The X-ray photoemission electron microscopy (PEEM) data are complemented with *in situ* reflection high energy electron diffraction (RHEED) investigations, *ex situ* scanning electron microscopy (SEM) and atomic force microscopy (AFM) measurements. This approach enabled to correlate the magnetic character of the particles with their individual size. The experimental findings are compared with calculated magnetic anisotropy contributions of the three different types of deposited nanoparticles (NPs). It was found that despite their different atomic structure, the body-centered cubic (bcc) iron and face-centered cubic (fcc) cobalt nanoparticles have a similar behavior and can exist in a state which demonstrates an unexpected ferromagnetic (FM) behavior with sizes down to 8 nm at room temperature (RT), while nickel particles only exhibit the expected superparamagnetic (SPM) behavior. This ferromagnetic state is assigned to an energetically excited, metastable structure which has a remarkably long life time before it decays into the expected superparamagnetic state. Combining PEEM with XMCD measurements allowed for the first time to follow the spontaneous transition from ferromagnetic to superparamagnetic behavior in *single* nanoparticles.

Detailed calculations of all magnetic anisotropy contributions for different sizes and types of particles indicate that the reported high anisotropy state can be associated with a meta-stable structural state due to the presence of local defects within the NPs, independent of the particle atomic structure and size.

These observations shed new light on the mechanisms which establish the size-dependent evolution of magnetic properties at the nanoscale.

Contents

Chapter 1

Introduction

A journey of a thousand miles begins with a single step.

Lao Tzu

Interest in magnetism developed since ancient times when it was observed that certain rocks (like those found in the island of Magnesia) had the property to attract metals containing iron (Fe), cobalt (Co) or nickel (Ni) and that these metals, when kept for a while in contact with materials that had this property, assimilate themselves the property to attract other metals. The current trend in technology [1-3] to minimize device size has led to the need of understanding the properties of materials at the nanoscale – from semiconductors to magnetic materials [4,5]. Due to their unique properties, the last few years have seen a rapidly growing interest in magnetic nanoparticles (NPs), which can find application in many fields ranging from medicine to data storage [6,7]. Also, the rapid development of new experimental techniques for producing the magnetic NPs and for probing and detecting them has resulted in a phenomenal increase in our knowledge of these systems today. Magnetic NPs show a variety of unusual magnetic phenomena when compared to the bulk materials, such as enhanced magnetic moments and magnetic anisotropies, mostly due to the large role played by surface/interface and finite-size effects [8,9]. A detailed understanding of these properties is however not a trivial task, since even mono-disperse nanomagnet ensembles can show considerable particle-to-particle variations in their properties either due to size and shape effects or inter-particle interactions [10-12]. Experiments with single particle sensitivity can address this problem, since the properties of isolated particles can be studied. This is the

approach of this dissertation, the experimental study of magnetic properties of individual nanoparticles. The first *step* in the *journey* of understanding, controlling and manipulating particles in the nanoscale regime is to observe the behavior of a single nanoparticle [13-15]. Recently, X-ray photoemission electron microscopy (PEEM) has been established as a unique tool to investigate the properties of individual NPs [16] and to correlate their magnetic properties with their morphology and sizes [17]. For practical application, the reduced size is of particular interest for magnetic storage technology [1-3], while at a basic science level, it enables an understanding of magnetism at the nanoscale [4,5]. In this context, the aim of this study is to investigate the role of the particle size on the magnetic properties, at nanoscale, in particular, to determine whether there is a breakdown in the usual scaling laws linking magnetic properties to size.

To have a clear overview, 3d transition metal nanoparticles with sizes ranging from 8 to 25 nm, deposited onto different non-magnetic substrates, were investigated by means of PEEM and the X-ray magnetic circular dichroism (XMCD) effect. By determining the magnetic response of such systems to magnetic fields and temperature, and by probing the systems from different orientation to determine the precise orientation of the magnetization, we establish the magnetic energy barriers for magnetization reversal and attempt frequencies of individual particles. Detailed calculations and theoretical simulations are used to fit the experimental data for a better understanding of the magnetic behavior of nanoparticles.

1.1. Outline of the thesis

In order to be able to follow this journey of understanding the magnetic properties at nanoscale, a general theoretical overview of magnetism will be given first. Structured into two main sections, **Chapter 2** gives an introduction to the general properties of magnetic nanoparticles, where terms such as ferromagnetic, monodomain, magnetic anisotropy are defined by explaining the important issues that arise when reaching the nanoscale: what superparamagnetic limit is and how magnetization reversal occurs in single domain particles depending on the temperature and applied field. In **Chapter 3**, various experimental techniques used to prepare and characterize the samples will be described. First the sample preparation process is presented. Since the particles are generated in an arc cluster ion source (ACIS) and deposited *in situ* onto different substrates, general details about how the particles

2

are formed, what are the landing parameters and the methods used for preparing the substrates for deposition, will be presented. The structural properties of the particles are investigated by transmission electron microscopy (TEM), reflection high energy electron diffraction (RHEED), scanning electron microscopy (SEM) and atomic force microscopy (AFM) measurements, which will be shortly presented in the second part of this chapter. X-ray photoemission electron microscopy combined with X-ray magnetic circular dichroism is the key technique used to study the magnetic properties of individual nanoparticles, and is the focus of the third part of this chapter. In **Chapter 4** a detailed description of the data analysis process will be given. Since the magnetic properties of the particles are extracted from white-black XMCD images, different Matlab program codes to identify, select and extract the precise contrast and intensity of the particles from the XMCD images are used. **Chapter 5** presents the structural and magnetic properties of single domain Fe nanoparticles deposited onto silicon (Si) substrates. It was found that these particles can show an unusually high magnetic anisotropy as compared with bulk Fe [18]. The high anisotropy state was found to be metastable and was assigned to a structurally excited state, but its detailed nature could not be resolved [18]. To clarify if the observed phenomenon of high anisotropy is restricted to this particular system or whether it might be also observed in other nanoparticle/substrate systems, in **Chapter 6** a comparison between different magnetic NPs deposited onto passivated Si substrates is presented. The magnetic properties of individual Fe, Co, and Ni NPs with sizes ranging from 20 down to 8 nm are compared. Despite their different atomic structure, the body-centered cubic (bcc) iron and face-centered cubic (fcc) cobalt particles demonstrate a similar magnetic behavior, displaying both ferromagnetically blocked (FM) or superparamagnetic (SPM) states at room temperature (RT), irrespective of their size, in contrast to the anticipated size-related scaling laws, while fcc Ni particles only exhibit the expected superparamagnetic behavior. The experimental findings are compared with calculated magnetic anisotropy contributions. The experimentally observed modifications of the magnetic anisotropy energy are assigned to localized structural defects of the particles, which are strong enough to cause ferromagnetic states in the case of iron and cobalt nanoparticles, but not in the case of nickel. To complete the picture of metastability of Fe, on **Chapter 7** the magnetic properties of Fe nanoparticles on different substrates (tungsten (W), nickel oxide (NiO), and copper (Cu)) are presented. Fe nanoparticles deposited under the same conditions onto W(110) show no magnetic contrast at RT. In the final **Chapter 8** a summary of the main conclusions of this dissertation will be presented.

Chapter 2

Magnetism at the nanoscale

This chapter gives a brief introduction to the properties of ferromagnetic nanoparticles. The first part is focused on the properties of ferromagnetic materials, explaining terms such as ferromagnetic order, magnetic anisotropy, magnetic domains, domain walls and the single domain state. In the second part the focus is on the magnetization reversal in case of single domain particles. The phenomenon of superparamagnetism and thermal relaxation along with the magnetization reversal process in single domain nanoparticles via coherent rotation described by the Stoner-Wohlfarth model will be discussed.

2.1. Ferromagnets and domains

2.1.1. Ferromagnetic order in solids

It is of great interest to understand magnetism in condensed matter systems including ferromagnets, spin glasses and low dimensional systems [6-9,19-27]. Macroscopic systems exhibit magnetic properties which are fundamentally different from those of atoms and molecules, despite the fact that they are composed of the same basic constituents, because magnetism is a collective phenomenon involving the mutual cooperation of a large ensemble of spins [28,29]. The key concept that allows one to describe the behavior of magnetizable

substances is the atomic magnetic moment, which is the sum of the orbital and spin moments of the electrons. The magnetization is defined as the magnetic moment per unit volume. For the 3d transition metals as Fe, fcc Co and Ni, the orbital angular momentum is much smaller than the spin, so the orbital contribution is small due to "quenching" of the orbital moment induced by the cubic crystal field and the magnetic moment is, to a first approximation, the same as the spin angular momentum. Still, due to the spin-orbit interaction, the orbital contribution is responsible for the magnetic anisotropy in the system and has to be considered.

Magnetic solids consist of large number of atoms with magnetic moments which can interact and act together in a cooperative way, which leads to behavior that is quite different from what would be observed if all the magnetic moments were isolated from one another. Magnetic interactions give rise to magnetic properties in real systems such as ferromagnetism, in which all the magnetic moments are aligned parallel, or antiferromagnetism, in which adjacent magnetic moments are found with antiparallel alignment. The characteristic for ferromagnetic materials (Fe, Co, Ni, Gd, alloys, etc.) is that they can possess a spontaneous net magnetization without an applied external magnetic field.

2.1.2. Magnetic anisotropy

Magnetic anisotropy describes the dependence of the internal energy of a material on the direction of the magnetization with respect to the crystal lattice. The spin-orbit interaction and the long-range dipolar coupling of magnetic moments give rise to an anisotropic energy landscape which produces *easy* and *hard* directions of magnetization and determines, in this way, in which directions the spins will align spontaneously. The magnetization will prefer to lie along the easy axes. The two opposite directions along an easy axis are usually equivalent. In systems exhibiting the so-called "exchange-bias" effect, one direction has lower energy than the other. The spin-orbit coupling is responsible for the intrinsic magnetocrystalline anisotropy (MCA), surface anisotropy, and magnetostriction, while the shape anisotropy is a magneto-static, dipolar contribution [30]. The magnetocrystalline anisotropy energy is larger in lattices of low symmetry and smaller in lattices of high symmetry. While in bulk materials

the main source of magnetic anisotropy are magnetocrystalline and magnetostatic energies, in the case of nanostructures, in addition to these anisotropies, the surface anisotropy is relevant and will be discussed in general terms below in this chapter and in detail for Fe NPs in Chapter 5 and for fcc Co and Ni particles in Chapter 6.

2.1.2.1. Magnetocrystalline anisotropy

The magnetocrystalline anisotropy [31] is a magnetic anisotropy energy (MAE) contribution with the same or higher symmetry as that of the crystal lattice. Phenomenologically, for crystals with cubic structure, the magnetocrystalline anisotropy energy is given by:

$$E_{MCA}^{cubic} = K_1 V (\alpha_1^2 \alpha_2^2 + \alpha_2^2 \alpha_3^2 + \alpha_3^2 \alpha_1^2) + K_2 V \alpha_1^2 \alpha_2^2 \alpha_3^2 \qquad \text{(Eq. 2.1)},$$

where K_1 and K_2 are the anisotropy constants, V is the crystal volume and α_1, α_2 and α_3 are the direction cosines of the magnetization. Neglecting the second term (i.e. $K_2 = 0$), when $K_1 > 0$, there are six equivalent energy minima along the x, y and z directions (i.e. <100>) [See Fig. 2.1(a)], while for $K_1 < 0$, the easy magnetization directions (eight equivalent minima) point along the vertices of the cube (i.e. along <111>) and the coordinate axes directions become now hard axes [See Fig. 2.1(b)]. This is the case for Fe, fcc Co and Ni [32], whose bulk values are presented in Table 2.1.

System (bulk)	Crystal structure	Lattice parameter (nm)	Magnetic anisotropy	Magnetic moment (μ_B/atom)	Curie temperature (K)	Anisotropy constant (μeV/atom)
Fe	Bcc	0.287	<100>	2.17	1044	3.3
Co	Fcc	0.355	<111>	1.72	1403	-3.8
Ni	Fcc	0.352	<111>	0.6	631	-0.28

Table 2.1. Crystal structure, lattice parameter, magnetic anisotropy direction, magnetic moment, Curie temperature and anisotropy constant values of bulk Fe, fcc Co, and Ni.
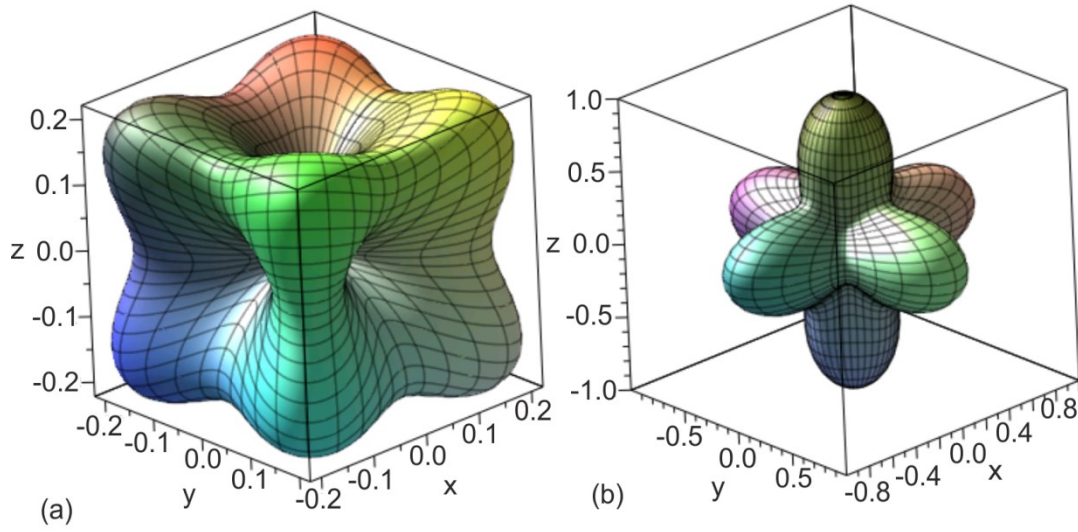
FIGURE 2.1. Cubic anisotropy energy density E_{MCA}^{cubic}/V in case of (a) $K_1 > 0$, where the cubic crystal axes are easy magnetization axes and (b) $K_1 < 0$ where the coordinate axes are hard axes.

2.1.2.2. Surface anisotropy

In small magnetic nanoparticles the surface can be a major source of anisotropy by breaking the symmetry and reducing the nearest neighbor coordination [33,34]. Upon decreasing the particle size, the strength of the magnetic contributions from the surface can become comparable with those from the volume of the particle. To describe the surface anisotropy, the Néel surface anisotropy (NSA) model [35] is often considered. This phenomenological model takes into account the magnetic anisotropy contribution for surface atoms with different local environments. For the surface anisotropy, two different cases have to be considered: (i) perfectly symmetric particles and (ii) particles with a deviation from that shape.

In the first case the NSA results in zero net surface anisotropy, since the anisotropy contributions of the surface facets cancel each other [10]. However, it has been shown that due to non-collinearities of the spins at the surface a noticeable contribution can arise [33]. The magnitude and character of this contribution to the effective anisotropy depends on the radius, the internal lattice of the nanoparticle [36] and also on the local surface anisotropy. In

the second case, an NSA contribution results already for collinear spin configuration [10], and is further modified by possible spin non-collinearities.

2.1.2.3. Shape anisotropy

The shape of the particles is another source of magnetic anisotropy, due to the demagnetizing field which can vary when aligning the magnetization along different directions in the particle and induce a uniaxial magnetic anisotropy term due to deviations from the perfect spherical shape [37]. The demagnetizing factors are isotropic only in the case of a uniformly magnetized single domain particle with ellipsoidal shape (e.g. spherical). In the case of a non-spherical particle, it will be easier to magnetize along a long axis than along a shorter axis. For example, in case of a uniformly magnetized ellipsoid, the shape anisotropy energy can be written as $E_{shape} = KV\sin^2\theta$ with the shape anisotropic constant $K = \frac{1}{2}\mu_0 M_S^2(N_x - N_z)$, assuming that the demagnetization factors along the short axes are equal $N_x = N_y$, where θ is the angle between the magnetic moment and the long axis of the ellipsoid, M_S is the saturation magnetization and N_z is the demagnetization factor along the long axis. For a prolate ellipsoid it follows $K > 0$ and the effective anisotropy is of *easy axis* type, since there exist two minima of the anisotropy energy along the polar $\pm z$ axis. For an oblate ellipsoid it follows $K < 0$ and the anisotropy energy has its minimum in the equatorial (x, y) plane. In this case the anisotropy is of *easy plane* type.

2.1.2.4. Magneto-elastic anisotropy

Strain can yield a sizeable magneto-elastic anisotropy contribution in nano-sized magnets [38]. In the case of a single stress σ in cubic crystal systems considering isotropic magnetostriction $\lambda_{100} = \lambda_{111} = \lambda$, the expression for the magneto-elastic anisotropy is:

$$E_{ME} = -\frac{3}{2}\lambda\sigma(\alpha_1\gamma_1 + \alpha_2\gamma_2 + \alpha_3\gamma_3)^2 \qquad \text{(Eq. 2.2),}$$

8

where λ is the material-dependent magnetostriction constant, σ is the strain, α_1, α_2 and α_3 are the direction cosines of the magnetization, and γ_1, γ_2 and γ_3 are the direction cosines of the bond directions, towards the crystallographic directions.

2.1.2.5. Effective anisotropy

The effective anisotropy of a particle is the sum of all contributions, often resulting in a dominant uniaxial term $E_{eff}^{uni} = KV \sin^2 \theta$ with K the effective anisotropy constant, V the particle volume and θ the angle between the magnetization and the symmetry axis. Depending on the sign of the anisotropic constant, K, the system will exhibit different magnetic behavior. When $K > 0$, the anisotropy energy describes two local energy minima for $\theta = 0$ and $\theta = \pi$ separated by an energy barrier of KV. The magnetization lies along the positive (parallel) or negative (antiparallel) direction of the easy axis with no preferential orientation [Fig. 2.2(a)]. On the other hand, when $K < 0$ the energy is minimized for $\theta = \pi / 2$, meaning that any direction in the (x, y) plane corresponds to an easy direction [Fig. 2.2(b)].
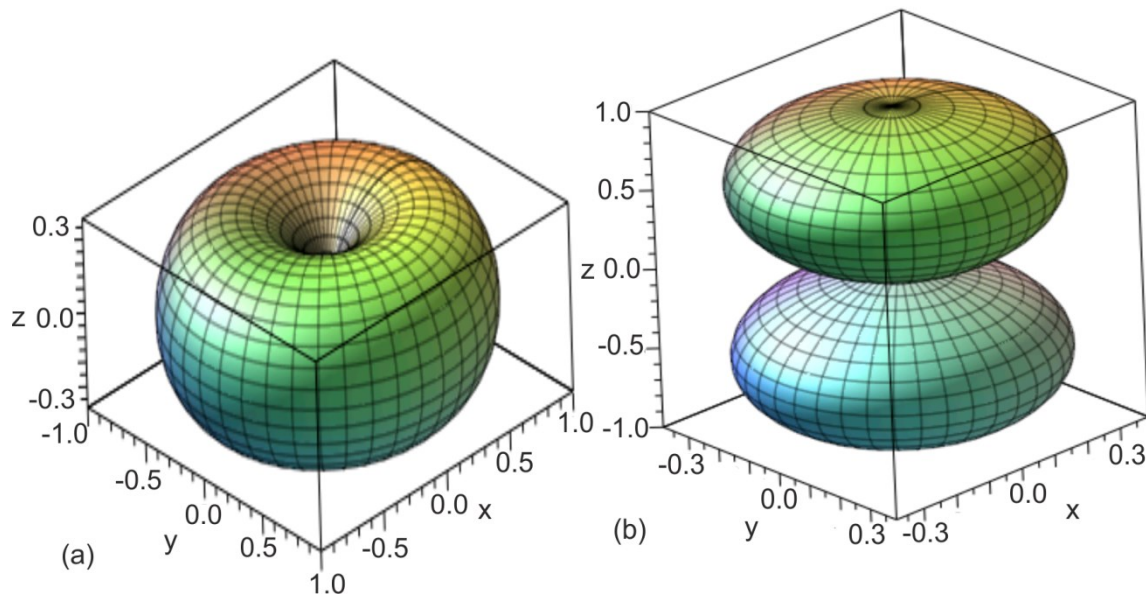

FIGURE 2.2. Uniaxial anisotropy energy density E_{eff}^{uni}/V in case of (a) easy axis anisotropy with $K > 0$ and (b) easy plane anisotropy with $K < 0$.

2.1.3. Magnetic domains and domain walls

The magnetic moments of individual atoms interact strongly with each other. In a ferromagnet, adjacent spins are aligned parallel by the strong interatomic exchange interaction. In large magnets the alignment can locally vary from one direction to another. A region with parallel aligned spins is called a magnetic domain [See Fig. 2.3(a)] [39,40]. The orientation of the magnetization in a domain and the size of the domain is determined by the local magnetic anisotropy, the exchange interaction and by the minimization of the magnetic stray field energy (i.e. magnetostatic energy). The transition from one domain to another domain is not abrupt but occurs via a continuous spin reorientation over the length of the so called domain wall [See Fig. 2.3(c)]. The width of the domain wall is, to first order given by the competition of magnetic anisotropy energy and exchange interaction and is typically of the order of nanometers (on average spans across around 100–150 atoms). The magnetization rotates through the plane of the domain wall in case of Bloch wall while in the Néel wall the rotation is within the plane of the domain wall. The Bloch wall is expected in the bulk because it leads to a smaller dipolar energy while the Néel wall tends to be formed in thin films, where there is a dipolar energy cost to rotate the spins out of the plane of the film [28]. In bulk-like samples the mobility of magnetic domain walls dominates the magnetization reversal when applying a magnetic field.
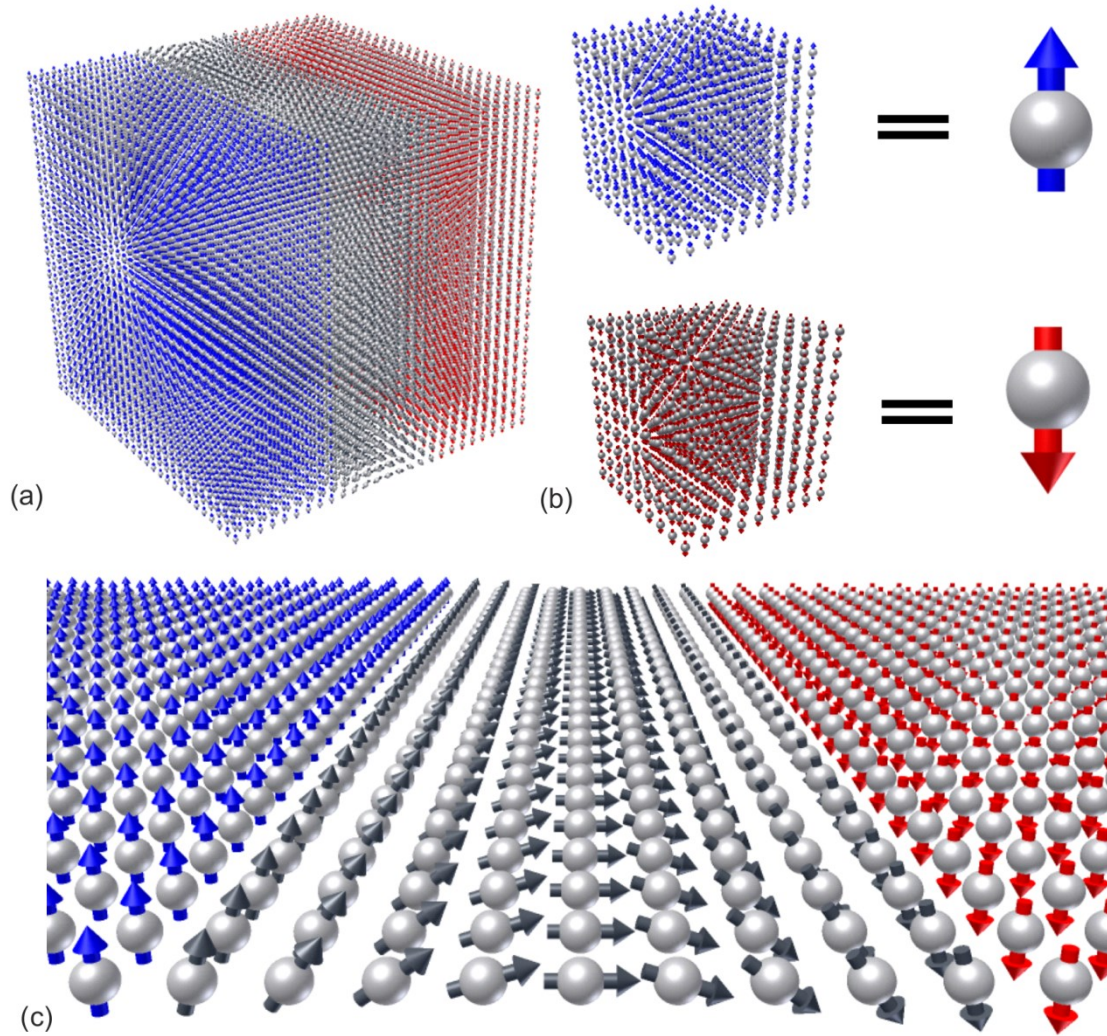
FIGURE 2.3. (a) Multidomain sample which consist of two domains (blue and red for up and down orientation) separated by a domain wall (grey region) along which the spins change gradually from up to down orientation. (b) By reducing the size of a magnet one can achieve monodomain particles where all the spins are oriented in the same direction and behave like a single macrospin. (c) Néel type domain wall (grey region) between two domains (blue and red for magnetization up or down). Reproduced from [41].

2.1.4. Single domain state

When reducing the size of a magnet, a stable single domain state with unique properties can be achieved [4,5]. Usually this happens when the particle size becomes comparable to the magnetic domain wall width. Below this critical dimension it is energetically favorable to

avoid formation of a domain wall in the structure (i.e. the total energy is minimized when no domain walls exist) so that the sample consists of a single domain, which means that all the spins are oriented in the same direction and behave like a macrospin [Fig. 2.3(b)]. This was first predicted by Frenkel and Dorfman [42] and estimates of the critical particle sizes were given by Kittel [43]. In the case of uniaxial anisotropy, the critical radius r_c below which a particle is in the single domain state is given by $r_c = 9 \dfrac{(AK_u)^{1/2}}{\mu_0 M_s^2}$ [44], where A is the exchange constant, K_u is the uniaxial anisotropy constant and μ_0 is magnetic permeability constant of vacuum. Typical values for r_c are about 14 nm for bcc Fe, 20 nm for fcc Co and 33 nm for fcc Ni [32].

2.2. Magnetization reversal

In single domain magnets it is found that, in the simplest case, the magnetization reversal process happens via coherent rotation of the magnetization vector between two equilibrium positions at 0K. However, the influence of the shape, temperature and applied magnetic field on the magnetization reversal can change this simple picture, e.g. cf. [45-47]. Rather than observing coherent rotation of the spins, it was observed that, in very small nanoislands, the applied field could favor a domain nucleation and subsequent the magnetization reversal occurs via domain wall propagation and that the Arrhenius attempt frequency prefactor v_0 is not constant as in the Néel-Brown model, but depends strongly on the size and shape of the system [46] (see Appendix 1).

2.2.1. Field-induced magnetization reversal at T = 0 K. Stoner – Wohlfarth model.

The Stoner - Wohlfarth model [48] is a frequently used theoretical description of the magnetization switching processes for monodomain ferromagnetic particles with uniform magnetization, which is strictly valid only at 0 K.

In the absence of an external field, a single domain particle will have the magnetization oriented along one of the easy axes. This is shown in Fig. 2.4 for the case of uniaxial anisotropy. Under the action of an external magnetic field, the Zeeman term E_Z alters the magnetic energy barriers (which result from the magnetic anisotropy energy) and can flip the magnetization depending on the relative orientation of the easy axis and the magnetic field. Stable orientations of the magnetic moments are given by the equilibrium between the magnetic anisotropy energy and the magnetostatic energy of the magnetization in an external magnetic field (Zeeman energy):

$$E_Z = -\mu_0 V \vec{M}_S \cdot \vec{H} = -\mu_0 V M_S H \cos(\phi - \theta) \quad \text{(Eq. 2.3),}$$

with ϕ being the angle between the external field and the easy axis, μ_0 the permittivity of vacuum and $\vec{M}_S$ the magnetization saturation vector.

The total energy of the particle is:

$$E = E_{eff}^{uni} + E_Z = KV \sin^2 \theta - \mu_0 V M_S H \cos(\phi - \theta) \quad \text{(Eq. 2.4).}$$
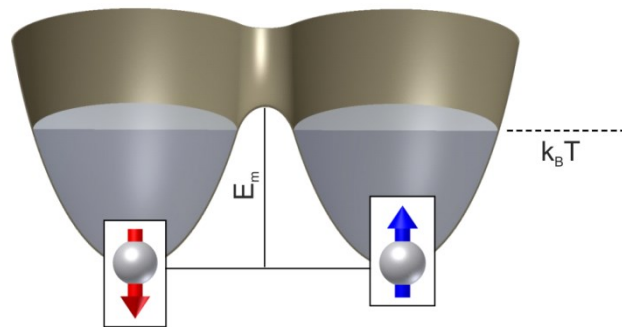

FIGURE 2.4. A single domain particle with uniaxial magnetic anisotropy has two magnetic ground states - magnetization up or down – separated by an energy barrier E_m, which depends on the properties of the material, volume and shape of the particle. Reproduced from [41].

The Stoner - Wohlfarth model describes the magnetization reversal of a single domain particle by finding the equilibrium positions of the magnetization as a function of the external field and plotting the projection of the magnetization along the direction of H. The resulting magnetization curves for different directions of the applied field are shown in Fig. 2.5. While our experiments are carried out at $T \gg 0K$, the Stoner-Wohlfarth model allows us to determine the maximum field needed to saturate the particles, which is the only parameter which is not sensitive to the temperature change.
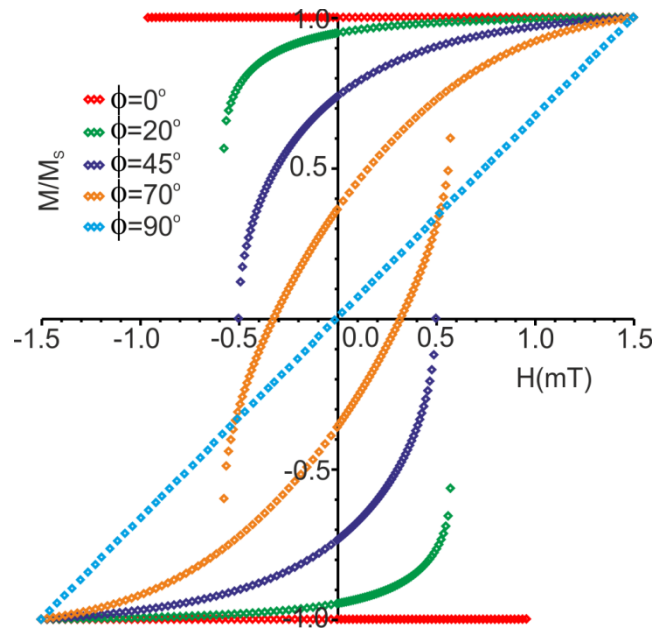
FIGURE 2.5. Hysteresis curves of a spherical single domain particle for different angles between anisotropy axis and external field in the framework of Stoner - Wohlfarth model.

2.2.2. Thermally driven reversal at zero field

At any finite temperature, there is a non-zero probability that thermal activation can overcome the anisotropy energy barrier, leading to switching of the particle magnetization. In this case, without any magnetic field, the orientation of the magnetic moment of a nanoparticle varies as a function of time in a stochastic manner due to thermal excitations. The rate of these fluctuations ν depends on the temperature T and the magnetic energy barrier E_m according to Néel-Arrhenius relation of the form:

$$\nu = \nu_0 \exp(-E_m / k_B T)$$

<div align="right">(Eq. 2.5),</div>

where $k_B T$ is the thermal energy and ν_0 the attempt frequency [47]. Typically values are about $\nu_0 = 10^{10} s^{-1}$, but the precise value of ν_0 depends on the size of the particles, the nature of the magnetic anisotropy and the temperature [47,49,50] and can be found in detail in Appendix 1. Since this relaxation process was first proposed by Néel in 1949 [51], the mean time between two flips is called the Néel relaxation time $\tau = 1/\nu$. This time can have any value from a few nanoseconds to years or much longer [52].

If the experimental time τ_{exp} required to measure the magnetization of a single nanoparticle is much larger than the relaxation time, $\tau_{exp} \gg \tau$, the nanoparticle magnetization will flip many times during the measurement [Fig. 2.6(b)], and the measured magnetization will average to zero. In this case, the nanoparticle is called superparamagnetic. If $\tau_{exp} \ll \tau$, the magnetization will not flip during the measurement, so the measured magnetization will reflect the instantaneous magnetization at the beginning of the measurement [Fig. 2.6(a)]. In this case the particle is considered as magnetically blocked or for simplicity, as ferromagnetic. The observed state of the nanoparticle (superparamagnetic or blocked) depends therefore on the measurement time. A transition between superparamagnetism and blocked state occurs when $\tau_{exp} \le \tau$. If the measurement time is kept constant but the temperature is varied, the magnetic behavior of the particle is characterized by the so-called "blocking" temperature $T_B = \dfrac{E_m}{k_B \ln(\nu_0 \tau_{exp})}$ below which the particle moments appear frozen on the time scale of the measurement. According to Eq. 2.5 the relaxation time depends on both E_m and T.
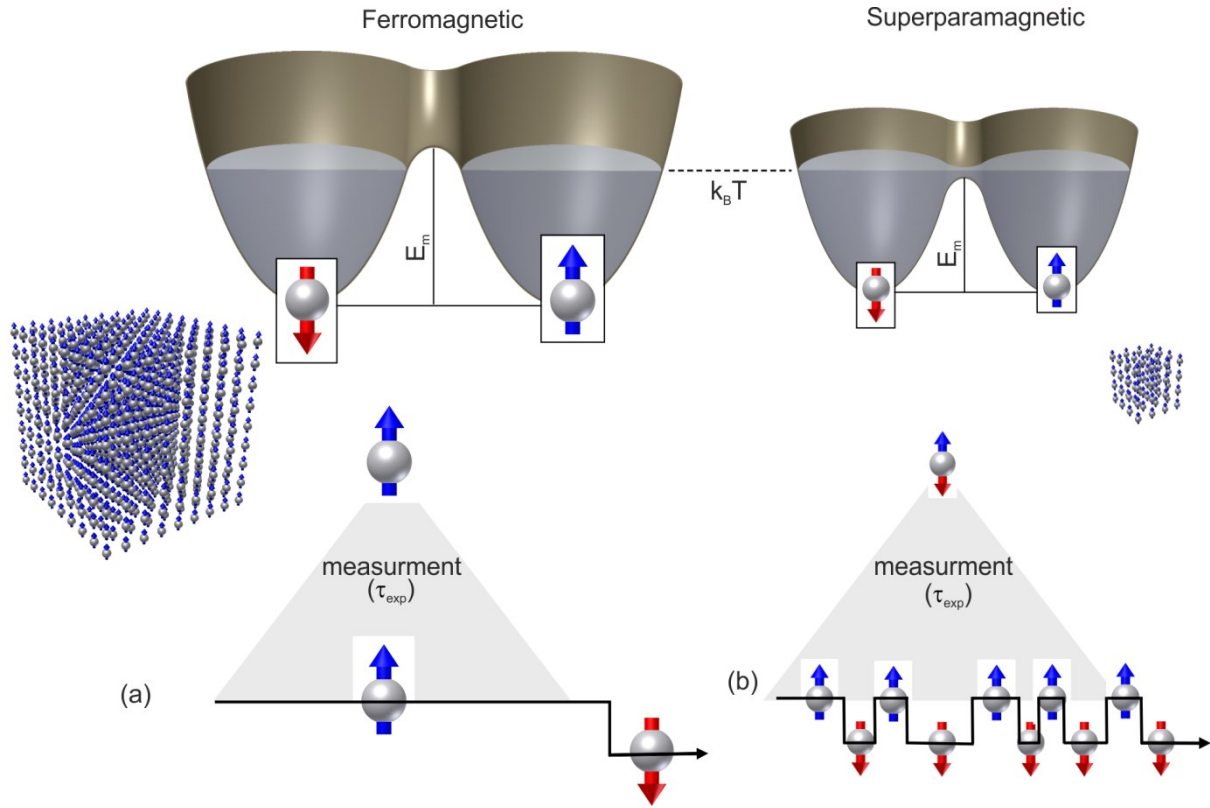
FIGURE 2.6. Magnetic blocking versus superparamagnetism. Depending on the competition between the energy barrier of the particle (which in first order is proportional to the volume) and the thermal energy, the sample can be either (a) ferromagnetic ($k_B T < E_m$) or (b) superparamagnetic ($k_B T > E_m$), when measuring with the same experimental time resolution $\tau_{\exp}$. Reproduced from [41].

2.2.3. Field-induced magnetization reversal at finite temperatures

When applying a magnetic field to a nanoparticle, the Zeeman energy (Eq. 2.3) modifies the magnetic energy barriers (See Fig. 2.7) and favors transitions from the state oriented antiparallel to the field to the state parallel with the magnetic field. The respective energy barrier for the state aligned with the field becomes larger, and in this way switching of the magnetization from this state back to the antiparallel state is less probable.

16
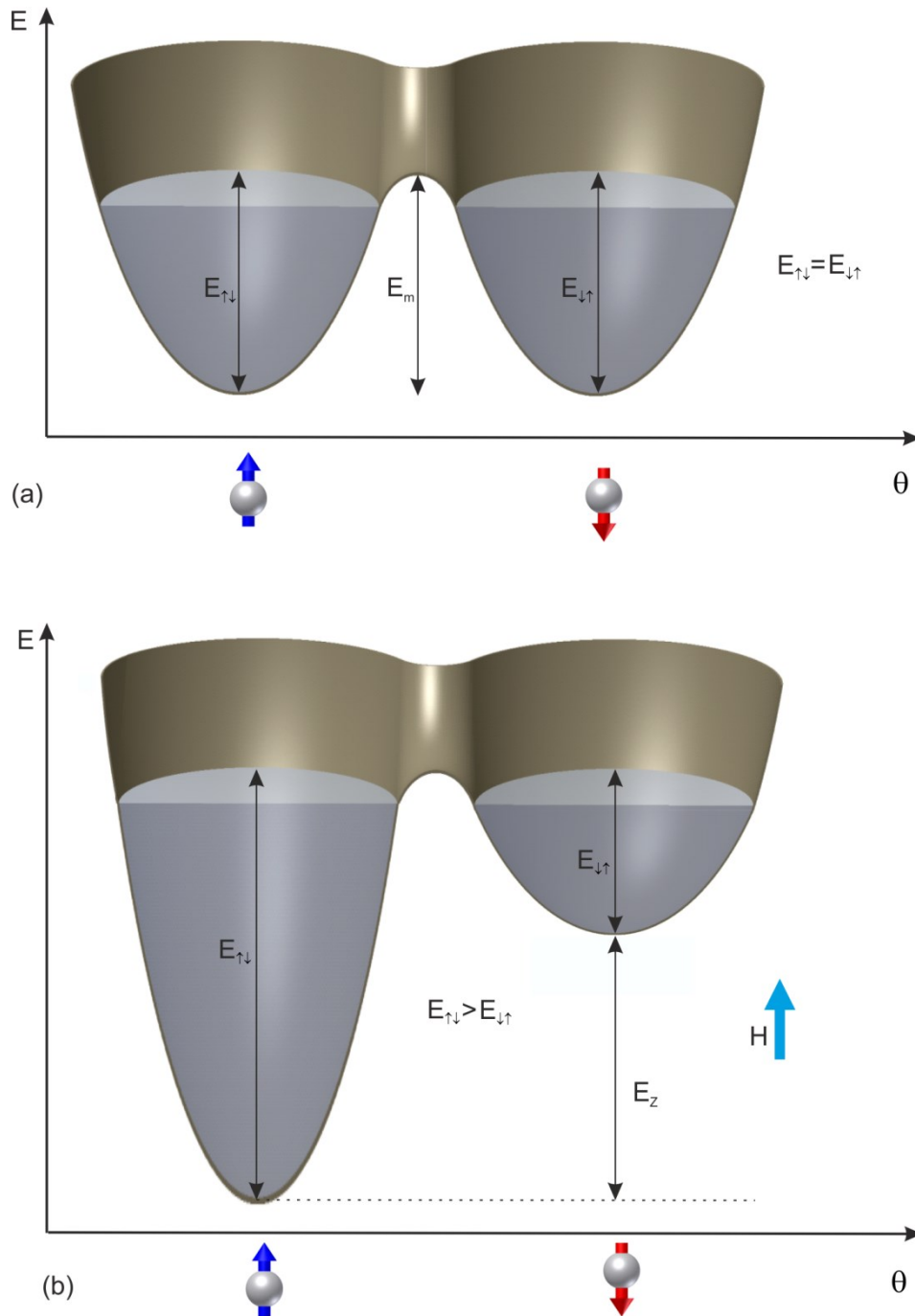
FIGURE 2.7. Schematic picture of the energy barriers of a single-domain particle (macro-spin approximation) with uniaxial anisotropy (a) without magnetic field and (b) in applied magnetic field. By comparing the energy barriers in (a) and (b) one can observe the influence of the Zeeman term.

For $k_B T >> E_m$ the magnetization curve of the particle is given by $M(H) \approx \mu L\left(\dfrac{\mu_0 M H}{k_B T}\right)$, where $L(x) = 1/\tanh(x) - 1/x$ is the Langevin function [See Fig. 2.8]. In this case no hysteresis (i.e., zero coercivity and no remanent magnetization) is observed. The low field slope of the curve increases with the size of the particle (See Fig. 2.8) showing that to saturate smaller particles one needs to apply larger magnetic fields.

FIGURE 2.8. Langevin curves representing Fe NPs with a diameter of 10 nm (red curve), 15nm (blue curve) and 20 nm (green curve) at RT.

Chapter 3

Experimental details

This chapter contains general information about the sample preparation and characterization, describing the different experimental methods and techniques used to study the structural and magnetic properties of individual nanoparticles. The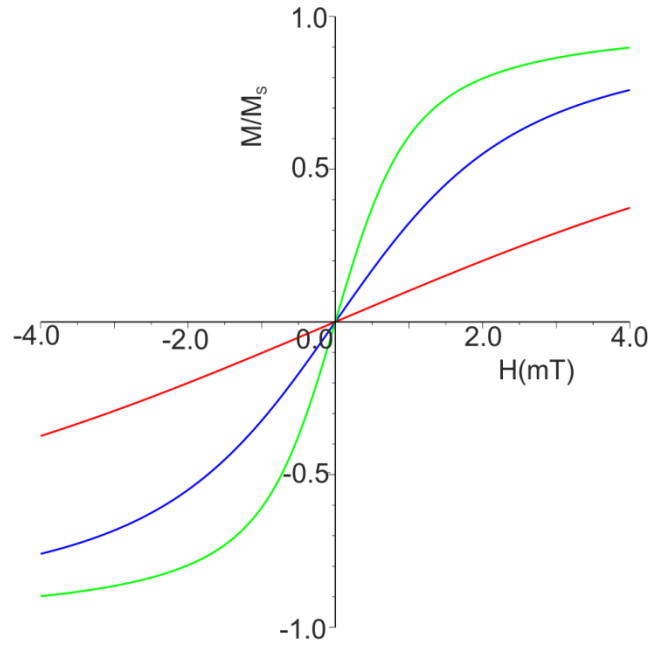 first part of this chapter gives an overview of the sample preparation process, explaining how the particles are generated in an arc cluster ion source and deposited in situ onto different substrates. The second part presents all experimental techniques used for structural characterization of the particles such as TEM, RHEED, SEM and AFM. The magnetic properties are investigated by real-space magnetic imaging with a photoemission electron microscope based on absorption spectroscopy using circularly polarized x-rays and exploiting the x-ray magnetic circular dichroism effect. Since a good understanding of this technique is crucial to the analysis of nanoparticle magnetic behavior, the last part of this chapter includes a short introduction to synchrotron radiation focusing on imaging with x-ray PEEM. The theoretical principles of XMCD will also be described.

3.1. Sample Preparation

The samples are prepared in three steps: Firstly, an array of chromium-gold markers [Fig. 3.1] are lithographically prepared on Si (100) wafer substrates passivated with a native SiO_x

layer [53]. The markers are needed for unambiguous particle identification during subsequent complementary microscopic measurements. Secondly, upon introduction of the substrates into the ultrahigh vacuum (UHV) environment, the substrates are treated to remove adsorbate layers such as water which originate from exposure to the ambient atmosphere. For the PEEM experiments, the substrates are either cleaned by mild sputtering with argon (Ar) ions (kinetic energy: 500 eV, Ar pressure: 5×10^{-5} mbar, duration: 20 min) or by thermal annealing in UHV in the preparation chamber attached to the PEEM located at the Surface/Interface: Microscopy (SIM) beamline of the Swiss Light Source (SLS) [See Fig. 3.2(a)]. For the *in situ* RHEED studies, the substrates are annealed in the UHV RHEED chamber (not shown) at the Surface/Interface: Spectroscopy (SIS) beamline of the SLS, at a temperature of about 250°C until the pressure in the chamber decreased towards its base pressure ($< 5 \times 10^{-9}$ mbar) after an initial out gassing of the sample and holder, and the RHEED pattern indicated a clean and flat SiO_x surface as discussed below. Finally, the NPs are deposited onto the clean substrates using the ACIS connected to the preparation system (Fig. 3.2) [54].
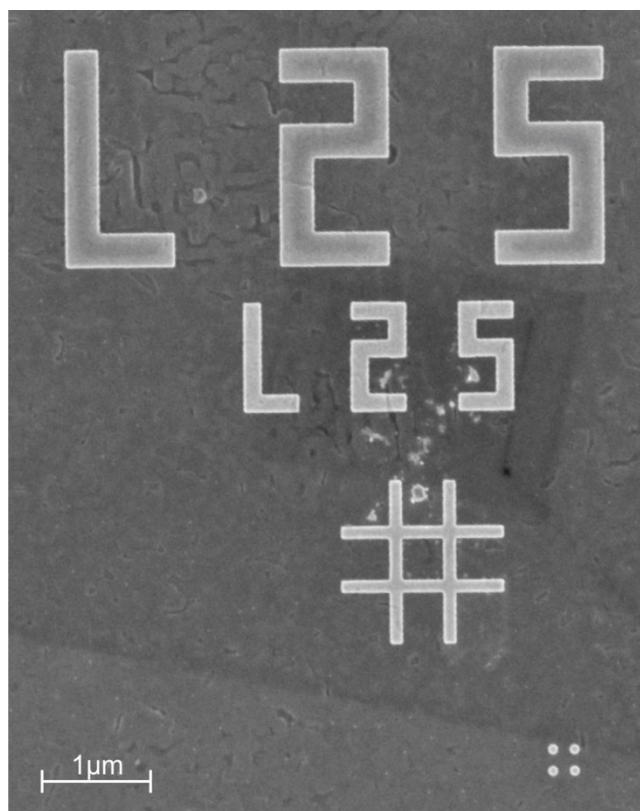

FIGURE 3.1. SEM image with lithographic Au/Cr markers which enable an unambiguous identification of the same particles in the different microscopes.
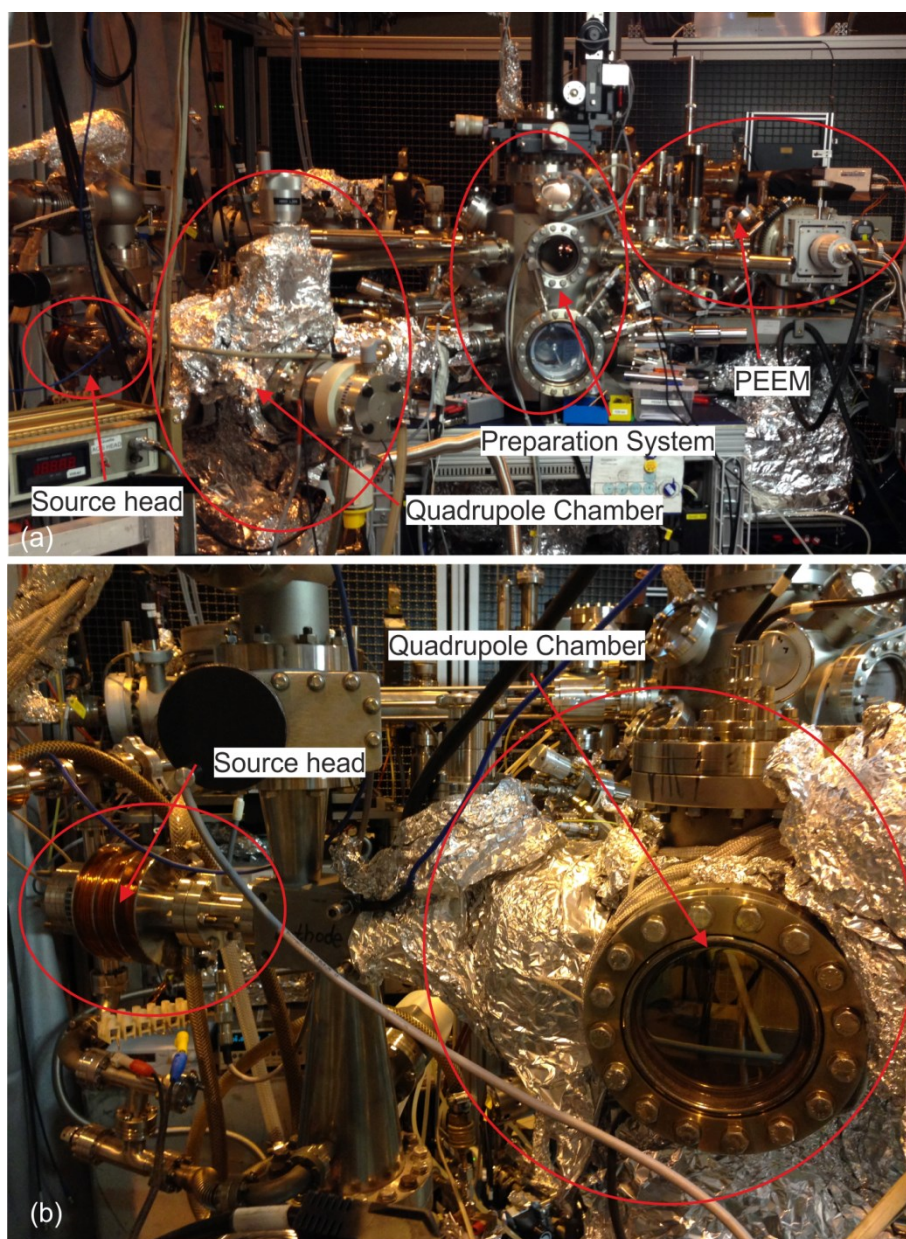
20

FIGURE 3.2. Arc cluster ion source. (a) Experimental setup: ACIS attached to the Preparation System and PEEM. (b) Source head and quadrupole chamber of the ACIS.
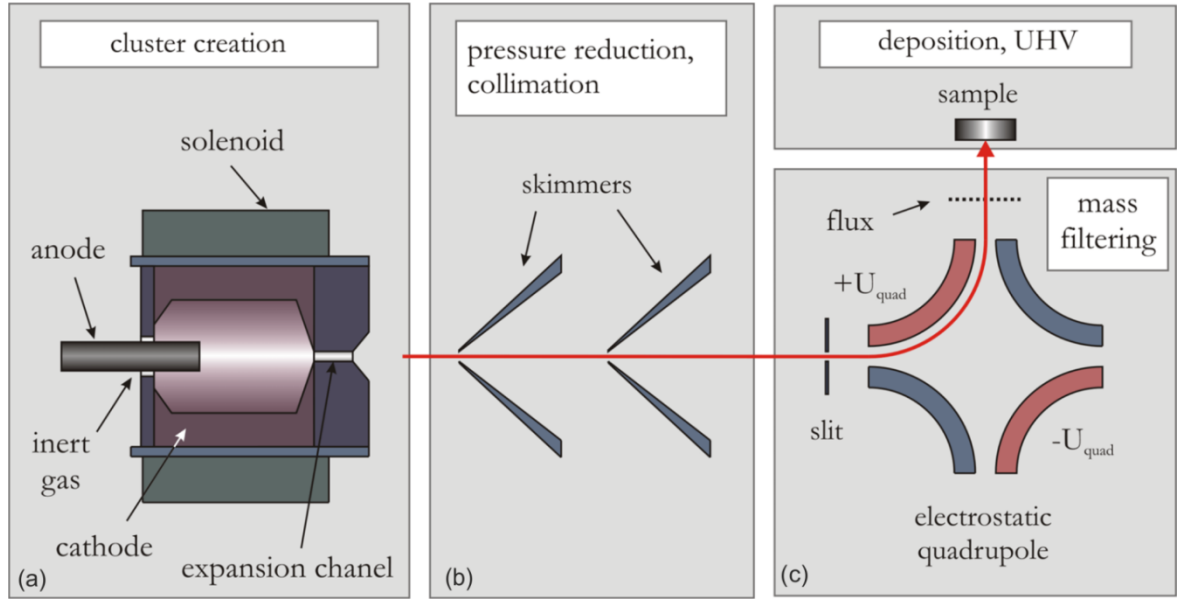
FIGURE 3.3. Schematic of the arc cluster ion source. Adapted from [55].

In the ACIS (Fig. 3.3), the NPs are formed by condensation of metal vapor in a carrier gas consisting of a Helium (He)/Argon mixture, each with a flow of 80 sccm, at a base pressure of 20 mbar. The metal ions are formed in the head of the source [Fig. 3.2, schematic in Fig. 3.3(a)] after an electrical discharge between the cathode and anode. The discharge dissipates 400 W across the cathode-anode gap. The elemental composition of the particles is given by the elemental composition of the cathode. An electrostatic quadrupole deflector [Fig. 3.2, schematic in Fig. 3.3(c)] is then used to mass-filter and to deflect the NPs onto the prepared Si substrate, which is held either in the surface preparation chamber (base pressure $\leq 5 \times 10^{-10}$ mbar) for the PEEM experiments or in a vacuum suitcase (base pressure $\leq 5 \times 10^{-9}$ mbar) used for the RHEED studies. A specific mean size of the particles is selected by setting an appropriate voltage to the quadrupole. A gold mesh placed in the nanoparticle beam path is used to measure the flux of the electrically charged particles within the beam, which is used to control the particle density on the substrate. For the PEEM experiments we choose a low particle density (a few NPs/μm^2) to avoid magnetic dipolar interactions between the NPs and to enable single particle detection in the experiments; typically, the average particle-particle distance is larger than 200 nm [17]. For the RHEED experiments we choose a higher particle density (of about 30 NPs/μm^2) to obtain a sufficiently high diffraction intensity from the NPs. At this coverage, agglomeration of the particles on the substrate is still avoided as confirmed

by subsequent SEM analysis, so that the RHEED data reflect the properties of an ensemble of isolated NPs. In both cases the pressure temporarily increases to about 5×10^{-6} mbar during the deposition due to the Ar and He carrier gas, and recovers few minutes after stopping the particle deposition.

Mass-filtered Fe, Co, and Ni particles are deposited onto clean SiO_x substrates. The deposition results in a nearly random spatial distribution of a few particles per μm^2 with random crystallographic orientation [56]. For all samples presented here, the cluster source operation parameters as well as the mass-filter settings are held constant. This ensures similar growth and landing conditions in all studies, with the kinetic energy of the particles prior to the impact on the substrate being smaller than 0.1 eV / atom [54]. Thus, the deposition takes place under the so-called soft landing conditions and no fragmentation of the particles or damage of the substrate is observed [57,58].

3.2. Structural characterization

3.2.1. *Ex situ* TEM characterization of the NPs

In order to experimentally probe the structure and morphology of the NPs, *ex situ* high resolution scanning transmission electron microscopy (HRSTEM) has been used. The particles were deposited onto SiN membranes and measured with HRSTEM by Armand Béché and Jo Verbeeck at the research center EMAT at the University Antwerpen [59]. These measurements confirm the previous studies on particles prepared with the same cluster source. Upon exposure to ambient air the particles form an oxide shell with a thickness of about 2-3 nm. The core of the particles remains metallic and demonstrates a faceted shape close to that predicted by a Wulff construction [54]. All measured Fe particle show single crystalline cores with no visible structural defects. The Fe_xO_y shell is polycrystalline.

3.2.2. *In situ* RHEED investigation

RHEED measurements were performed *in situ* in order to investigate the crystallographic structure and orientation of the deposited NPs with respect to the substrate, as well as the thermal stability of the particles and the substrate. For these investigations, the clean substrate is transferred from the RHEED UHV system, located at the SIS beamline of the SLS, to the surface preparation chamber which is attached to the PEEM located at the SIM beamline of the SLS for deposition of the particles, and back to the RHEED system using a vacuum suitcase. The RHEED experiments are carried out with electrons with a kinetic energy of 35 keV at grazing incidence with respect to the substrate. This geometry provides a surface sensitive probe which allows us to investigate the quality of the substrates and the deposited NPs simultaneously [56]. When introduced into the UHV system, the substrates give rise to a diffuse scattering pattern due to the presence of adsorbates from ambient air [Fig. 3.4(a)]. When annealing the substrates to 250°C in vacuum, a reduction of the diffuse scattering and the formation of Kikuchi lines can be observed [60,61] revealing a clean and flat surface with a preserved SiO_x layer upon this treatment [see Fig. 3.4(b)].
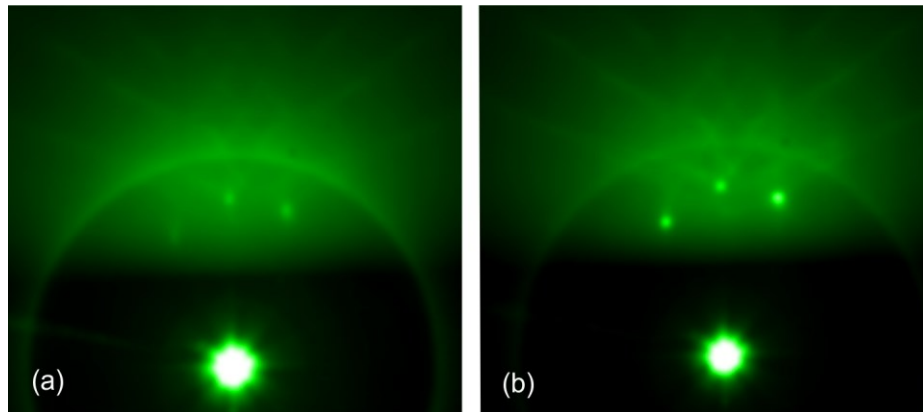
FIGURE 3.4. RHEED pattern of the Si substrates (a) at RT and (b) 250°C.

3.2.3. *Ex situ* AFM and SEM characterization of the NPs

Since the spatial resolution of the PEEM is typically 50 - 100 nm, more detailed investigations on particle morphology and sizes are carried out *ex situ* by means of SEM and AFM. As illustrated in Fig. 3.5(a)-(d), the lithographic marker structures allow an identification of the same particles in PEEM, SEM and AFM [17]. This approach enables to correlate the magnetic character of individual particles with their shape and size.
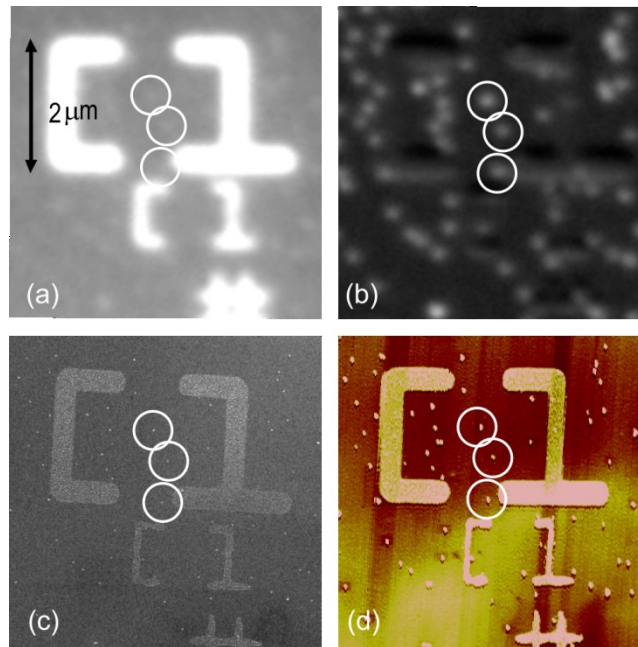
FIGURE 3.5. (a) Raw PEEM image recorded with the photon energy tuned to the L_3 Fe edge (708 eV). (b) Elemental contrast images obtained upon pixelwise division of (a) with a reference image recorded at a pre-edge energy (703 eV). (c) SEM and (d) AFM images of the same region as in (a) and (b). Lithographic Au/Cr markers enable an unambiguous identification of the same particles in the different microscopes. This is illustrated with three particles which are highlighted with circles. Adapted from [62].

Ex situ high resolution scanning electron microscopy [Fig. 3.5(c)] is used to investigate the morphology of the individual particles and to exclude particles that are too close or that agglomerate from the analysis. Only well-shaped and well-separated particles were considered for investigation. Fig. 3.6 displays typical SEM micrographs of iron nanoparticles that have been exposed to ambient air. No indication for particle fragmentation is found. Typically, we find nanoparticles with a compact shape, as shown in Figs. 3.6(a) and (b), as well as small agglomerates as shown in Fig. 3.6(c). Note that the lateral size of the particles in SEM is difficult to determine due to (i) the formation of an oxide shell upon transport of the sample at ambient air and (ii) the limited spatial resolution of the microscope which is about 2 – 3 nm. In this sense, SEM enables to study only the particle shape. Thus, AFM [Fig. 3.5(d)] was further employed in order to determine the size of the selected particles by measuring their height with respect to the substrate surface upon exposure to ambient air. Note that while AFM provides an accurate measure of particles heights, tip convolution effects hinder a reliable determination of their lateral dimensions [63].

Previous studies on similar nanoparticles showed that the height of the supported particles corresponds well to the lateral diameter of the particles being determined from transmission electron microscopy [64]. Thus, the shape of the present particles is largely conserved under the landing conditions and here a small flattening of the particles by about 1 nm might be possible within the experimental uncertainties, which could lead to a preferred in-plane magnetization of the particles due to the resulting shape anisotropy. However, the magnetic data shows that any possible shape anisotropy contribution seems weak compared to the uniaxial magnetic anisotropy of the particles, as discussed later in this thesis.
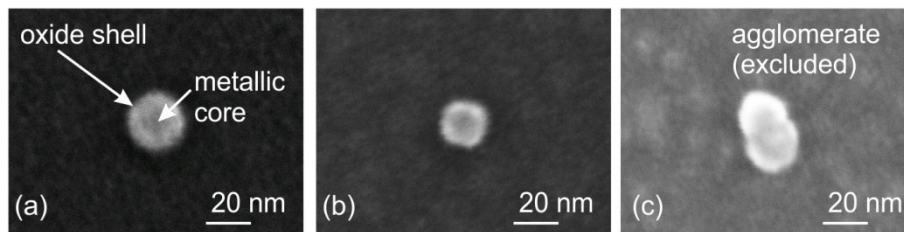

FIGURE 3.6. (a), (b) SEM images of highly symmetric and compact iron nanoparticles with an AFM height of (a) 18 nm and (b) 13 nm. Agglomerates as shown in (c) are excluded from the analysis.

3.3. Magnetic characterization

Magnetic imaging based on spatially resolved absorption spectroscopy was carried out at the SIM beamline, Swiss Light Source, Villigen, Switzerland. Using x-ray magnetic circular dichroism together with photoemission electron microscopy, one can visualize the magnetic moment (direction) of the particles in real time. This section presents the concepts and experimental details of x-ray absorption spectroscopy and x-ray magnetic circular dichroism together with photoemission electron microscopy.

3.3.1. Synchrotron radiation

Due to their unique properties, such as wide spectral continuity ranging from infrared (10^{-3} eV) to hard X-rays (10^5 eV), high flux (up to 10^{13} photons per second in third generation storage rings), high intensity, high brightness, low divergence, variable polarization, and pulsed time structure, synchrotron radiation has been generated in storage rings for decades and has been widely used to study both fundamental questions in physics and to characterize a plethora of materials at the atomic, molecular and/or condensed matter levels. The principle of synchrotron radiation generation is simple: when low mass charged particles (e.g. electrons or positrons) describe a curved path at near relativistic speeds, they undergo an acceleration. This results in loss of energy that is manifested in the form of emitted electromagnetic radiation. The electron beam at the source is generated using an electron gun. This beam is first accelerated to relativistic speeds using a linear accelerator (LINAC), which is a several-meters long linear device, and then is injected in the booster ring, in which the electron energy is ramped up to a few GeV before injection into the storage ring. The SLS booster has a circumference of 270 m and consists of a variety of items such as a radio frequency (RF) cavity acceleration station, vacuum components, diagnostic tools and a total of 237 magnets. Located in the same tunnel as the storage ring, is an especially designed ring used to produce a high-quality electron beam for the so-called top-up injection. In this mode the booster injects periodically "bunches" of electrons into the storage ring, keeping the intensity of the circulating electron beam constant.

In the storage ring, the electrons are maintained in a closed path using bending magnets. These magnets generate a strong magnetic field (typically 1 Tesla) which is oriented perpendicular to the electron trajectory and deflects the electrons. At these bending magnets, the electrons undergo a centripetal acceleration which results in the emission of electromagnetic radiation. This polychromatic photon radiation is emitted tangentially to the path of the electrons. At SLS there are 19 beamlines which use radiation emitted from accelerating electrons passing through different insertion devices (IDs), placed in the straight sections between the arc segments containing the bending magnets. Undulators consist of permanent magnets, arranged in a periodic array with a variable gap. In these IDs the electrons are forced to move in an oscillatory path in the plane of the storage ring and concentrate, in this way, the synchrotron light into discrete lines in the spectrum. The distance between each slalom turn and the strength of the magnetic field determines the desired wavelength. For the longest wavelength the magnetic field in the undulator is produced with electromagnets instead of permanent magnets. The light is emitted in a very narrow cone, similar to a laser beam. The light spot diameter can be reduced to less than a micrometer using focusing mirrors. The intensity is about a factor of 1000 higher than the light from a bending magnet, with a corresponding reduction in the time needed to perform an experiment.

The energy range of photons delivered by the synchrotron is directly related to the diameter of the ring, the stored energy of the electrons (2.4 GeV at SLS) and the insertion device. The photon energy of the SIM beamline ranges from 90 eV up to 2000 eV [65]. The beamline consists of two 3.8 m Apple II type undulators, a collimating mirror, a plane grating monochromator SX-700 with gratings from 300 l/mm to 1200 l/mm, and focusing mirrors [65]. Switching the polarization can be done fast, within a few seconds [66] due to the tune/detune mode: changing the gap by a few millimeters will shift the center of the emitted photon energy away from the energy bandpass of about 100 meV of the monochromator (detune mode) as shown in Fig.3.7. At specific energy, the Fe L_3 edge for example, the shift of one of the IDs is set to generate C^+ polarization while the shift of the other ID is set to generate C^- polarization (See Fig. 3.7). With two undulators, it is now possible to switch between them by having one tuned and the other detuned as only photons from the tuned undulator will hit the sample, while the photons from the detuned undulator will not pass the

monochromator. This way of changing polarization is faster than changing the polarization of the undulator.
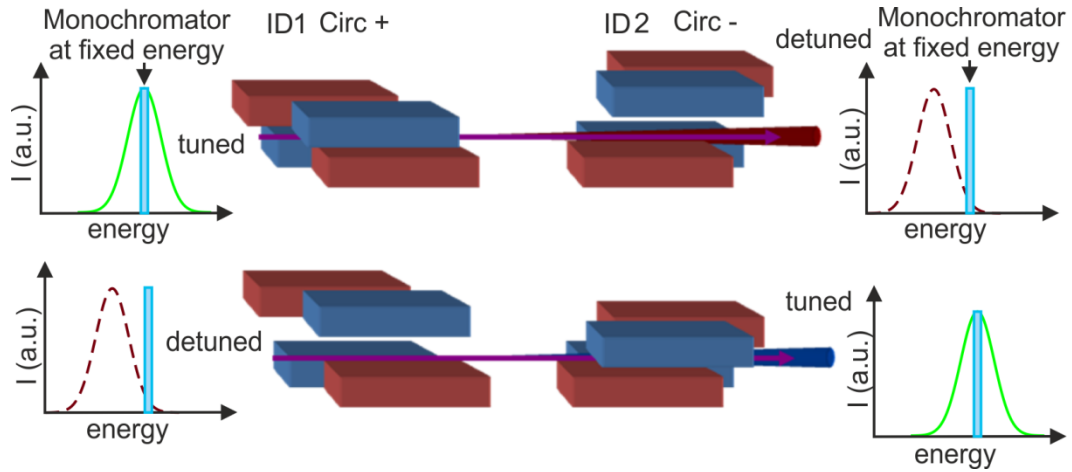

FIGURE 3.7. Switching scheme of the undulators in the tune/detune mode at the SIM beamline. The photon energy generated from an undulator has a specific, finite width in the range of a few electron-volt (eV), which must be tuned to the energy of the monochromator to get photons on the sample. If the energy of the undulator is detuned and does not match the energy of the monochromator, no photons will arrive at the sample. The tune/detune process of the undulators is done by changing the gap distance. With two undulators, it is possible to switch between them by having one tuned and the other detuned as only photons from the tuned undulator will hit the sample, while the photons from the detuned undulator will not pass the monochromator. If the first undulator is set to circular right polarization and the second to circular left polarization, one can switch the polarization within a few seconds. Adapted from [66].

3.3.2. X-ray absorption Spectroscopy (XAS)

When matter is irradiated with x-rays, the incident photons can be absorbed or scattered by the constituent atoms. In the case of absorption, a core electron is excited into an unoccupied state above the Fermi level and can decay by emitting a fluorescence photon or Auger

electrons, which can excite secondary electrons. The escape depth of the emitted photons and electrons is illustrated in Fig. 3.8.
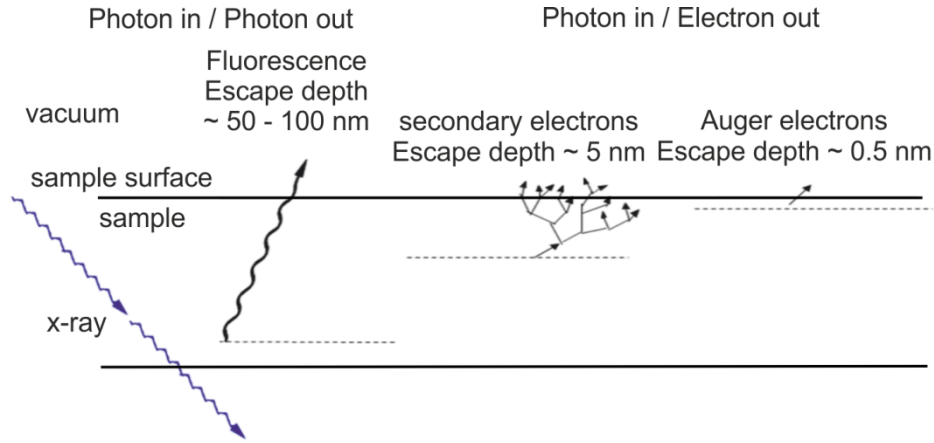

FIGURE 3.8. The escape depth of emitted photons and electrons in the absorption process of the x-rays.

When tuning the photon energy to a core level, the absorption process becomes resonantly enhanced. This is known as near edge x-ray absorption fine structure (NEXAFS) [67,68], where the transition is between a core and a valence state and contains information about the density of unoccupied electronic states. Non-resonant absorption in the energy region above the rising absorption edge, known as extended x-ray absorption fine structure (EXAFS), contains information about the type and the spatial arrangement of the neighboring atoms [69,70].

The intensity of the incident beam I_0 passing through the sample is attenuated exponentially with the depth z and the absorption coefficient μ of the sample. The local intensity in the sample is described by the Beer-Lambert law:

$$I(E,z) = I_0(E)e^{-\mu(e)z} = I_0 e^{-\rho\sigma z}$$ (Eq. 3.1),

with ρ - the atomic density of the sample and σ - the absorption cross section, which is given by the number of photons absorbed per atom divided by the number of incident photons per unit area. Since the process of x-ray absorption depends on the properties of initial and final

electronic states, one can obtain information on the local electronic structure (oxidation state, spin state, nature of the chemical bond) and the local structure (site symmetry) by measuring the absorption coefficient. Dipole selection rules provide that transitions are possible only between states for which $\Delta m_s = 0, \Delta m_l = \pm 1$. For instance, at the $L_{3,2}$ transitions from the 2p states to unoccupied 3d states are allowed. The change in the absorption as a function of the photon energy and polarization can yield detailed information about the chemical composition of the materials, the relative positions of the constituent atoms and magnetic properties of the material [71]. Since the atomic levels are characteristic of the elements, elemental sensitivity is achieved by tuning the photon energy to the excitation energy as illustrated in Fig. 3.9 for the 2p to 3d atomic transition of Fe, Co and Ni.
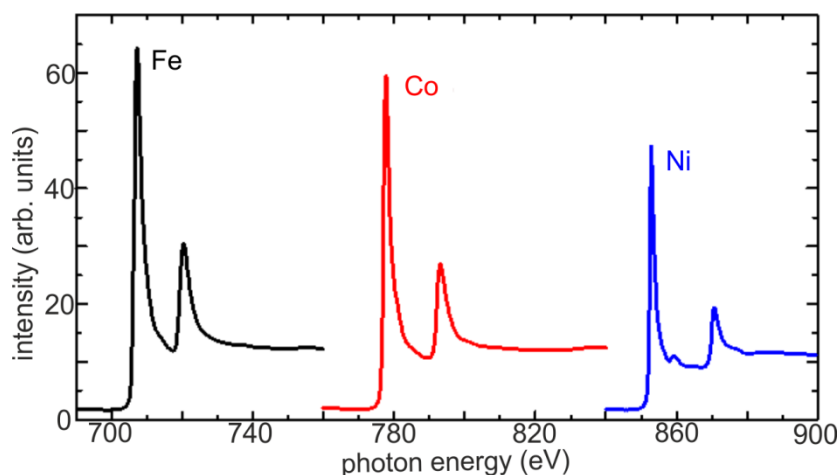
FIGURE 3.9. X-ray absorption spectra for Fe, Co and Ni samples illustrating the chemical specificity of X-ray absorption spectroscopy. In the X-ray absorption process an electron is excited from a core level to an empty valence state. This results in pronounced resonances at the absorption threshold, as illustrated here for the $2p_{3/2}$ to 3d (L_3 edge) and $2p_{1/2}$ to 3d (L_2 edge) excitations in Fe (black), Co (red) and Ni (blue).

There are different methods to measure the x-ray absorption spectra depending on the nature of the processes used for x-ray absorption detection: transmission, fluorescence, electron emission in Auger electron mode or total electron yield (TEY) mode measuring the current resulting from the ejection of all electrons emitted by the sample (Auger electrons, secondary

electrons) [70]. The TEY signal drops exponentially with the distance from the sample surface [72] due to the small mean free path of electrons in solids at these energies. For L-edge absorption of Fe, Co and Ni, the TEY probing depth is about 5-10 nm, although about 60% of the signal originates from the topmost 2nm of the sample [68].

3.3.3. X-ray magnetic circular dichroism

X-ray magnetic imaging is based on the x-ray magnetic circular dichroism effect, which can be understood as polarization-dependent absorption of x-rays in spin-polarized materials. The use of circularly polarized synchrotron light allows the use of magnetic dichroism as a contrast medium for imaging magnetic materials [73]. The magnetic circular dichroism is, by definition, the difference in absorption for the right and left circularly polarized light in a magnetic material. In a ferromagnetic material, the density of unoccupied states at the Fermi level is different for the two spin directions due to the exchange interaction. For the absorption process to take place, it is necessary that the absorption satisfy the so-called "selection rules ", not all the transitions are allowed. A unique feature of XMCD is its ability to separate spin and orbital moment. If the material has no magnetization, there is no difference between the "spin up" or "spin down" densities of states in the valence band, so there is no XMCD signal. Strong XMCD effects appear at the L-edges ($2p - 3d$ transition) of the transition metal ferromagnets Fe, Co and Ni. The XMCD effect is opposite in sign at the L_3 and L_2 edge because of the opposite sign of the spin-orbit coupling in the 2p states (J=L+S at the L_3 and J=L-S at the L_2 edge).

X-ray PEEM is a full-field photon-in/electron-out imagining technique, pioneered by spectroscopic imaging near edge x-ray absorption with secondary electrons by Tonner et al [74]. It combines high resolution electron microscopy with x-ray absorption spectroscopy, giving it the ability to perform spatially, elementally, chemically and magnetically-resolved studies. A recent review was given by Ernst Bauer in Journal of Electron Spectroscopy and Related Phenomena [75].
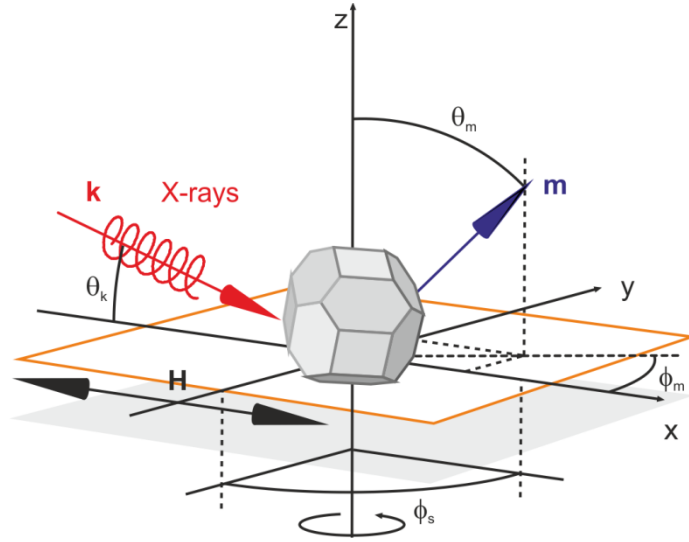
32

FIGURE 3.10. Schematics of the experimental geometry of the X-ray PEEM experiments and the equilibrium shape of the nanoparticles. θ_k is the angle of incidence of the x-ray beam propagation vector k with respect to the sample surface, and θ_m and φ_m are the polar and azimuthal angles of the nanoparticle magnetization m with respect to the lab frame. ϕ_s is the azimuthal angle which gives the sample orientation. The direction of the applied field H is also indicated in the figure. Adapted from [18].

3.3.4. Photoemission electron microscopy

The x-ray magnetic circular dichroism effect [73] can be used to measure the local magnetic moment and the direction of magnetization of the particles by means of x-ray PEEM. To visualize and determine the magnetic orientation in single domain ferromagnetic particles, the XMCD effect is combined with PEEM. In x-ray PEEM the XMCD effect gives rise to a magnetization dependent intensity according to

$$I(C^{\pm}) = I_0 \pm \gamma(\vec{k} \cdot \vec{m})$$ (Eq. 3.2),

where I_0 is the isotropic (non-magnetic) contribution, k is the X-ray propagation vector with an angle of incidence $\theta_k = 16°$ (Fig. 3.10), $\vec{m}$ is the magnetization vector of the particle, γ is

a material and photon energy dependent constant, and $C^{\pm}$ denote circular right- and left-handed polarization. If the orientation of the helicity and the magnetization are parallel or antiparallel to each other, the contrast is maximum, while it is zero in the perpendicular case. Magnetic contrast images are obtained by pixelwise division of two images recorded successively with circular right- and left-handed polarization at the L_3 edge. The division enhances the magnetic signal and minimizes all other contributions such as the topography or the chemical signal. The acquisition of an image with one polarization needs typically 10 s. Thus, about 20 s are required to obtain a magnetic contrast image, which gives the typical time resolution of our experiment of $\tau_{\mathrm{exp}} = 20\,\mathrm{s}$.

To obtain a low noise magnetic contrast, 20 XMCD image pairs are averaged after correction for sample drift (See Chapter 4). In this work, quantitative XMCD values are defined as the asymmetry of absorption between circular right and left polarization, and a measure of the magnetization of an individual particle is given by the normalized XMCD contrast, defined as:

$$A = \frac{I(C^+) - I(C^-)}{I(C^+) + I(C^-)} \qquad\qquad \text{(Eq. 3.3).}$$

We present next the characteristics of the PEEM setup located at the SIM beamline [65,66,76] at the Swiss Light Source, were the experimental measurements for this thesis were performed. The PEEM is a commercial instrument from Elmitec, operating in UHV conditions. The PEEM imaging column is schematically illustrated in Fig. 3.11.

The sample is illuminated with mono-chromatic, polarized synchrotron radiation at an angle of 16° with respect to the sample surface, resulting in a focused spot on the sample with a full width at half maximum of about 220 μm. The vertical size of the spot can be adjusted by the exit slit size of the beamline which is typically 50-150 μm for PEEM measurements. To assure a uniform illumination of the sample and to avoid edge effects, the spot size was kept larger than the 20 μm field of view for the PEEM measurements used here. The photon energy resolution is determined by the X-ray monochromator which is equipped with the plane mirror and three gratings and the spatial resolution by the electron optics in the PEEM [66]. As a result of the absorption process, a broad energy spectrum of emitted electrons is

produced in the sample, with energies varying from zero up to the energy of the incoming photons. Emitted electrons are accelerated to the microscope objective lens by applying a negative potential of 20 kV between the sample and objective lens (see Fig. 3.11) and their lateral distribution is then magnified by a set of electromagnetic lenses. Located in the back focal plane of the objective lens, the contrast aperture selects only those electrons for imaging that originate from a certain range of emission angles. The size and lateral position of this aperture can be changed by moving a slider assembly carrying several apertures of different diameters. Deflectors and stigmators are used to optimize the electron path through the microscope and to correct image distortions.
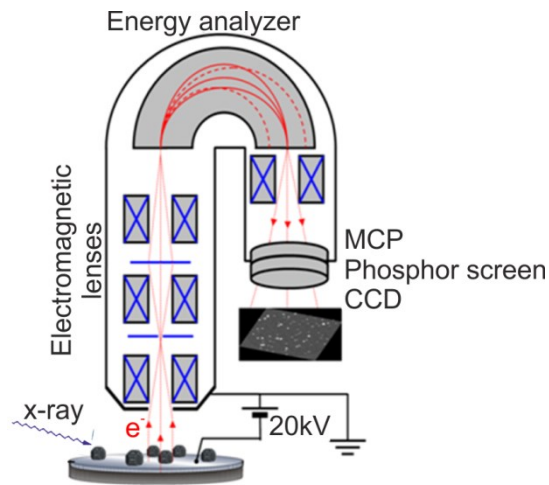

FIGURE 3.11. Sketch of configuration of a PEEM consisting of the sample, accelerating voltage, lenses, energy analyzer, and detector.

A hemispherical energy analyzer, which can be tuned to specific electron energies by changing the "start-voltage", is used to reduce the energy spread and to limit the secondary electrons reaching the intensifier to a kinetic energy of 1-2 eV for the best combination of spatial resolution and intensity of measured signal. After passing the energy analyzer the electrons go through a multi-channel plate intensifier and after multiplication are converted to visible light via a phosphor screen, from which the light is then detected by a charge-coupled device (CCD) camera giving a full field image of the sample in real time with up to 16 Hz frame rate. The image being projected on the screen is a magnified spatial map of the

electrons which have left the sample surface. To obtain focused and undistorted images, one has to align all the lenses, typically using a sample with flat and well defined lateral features. This process starts with the alignment of the sample normal with the optical axis of the objective lens by correcting for any tilt in the sample at decreasing fields of view, and subsequently the alignment of all of the electromagnetic lenses is performed by varying each lens current by a small amount (i.e. "toggling the lenses"). To image particles which are smaller than the approximately 50 nm spatial resolution of the PEEM, it is crucial to have a low density of the particles on the sample [17]. The particles appear blurred, but the magnetic and elemental information reaches single particle level.

The Elmitec PEEM III situated at the SIM beamline is equipped with a 360° rotary manipulator, which gives the possibility of varying the azimuthal angle of the sample ϕ_s. Since the XMCD contrast is proportional to both magnitude and direction of magnetization, images at three different angles are sufficient to determine precisely in 3D space the orientation of the magnetic moments of individual nanoparticles. The PEEM manipulator provides four electrical connections to the sample holder and several sample holders are available for carrying out different types of *in situ* experiments, such as applying a current through a coil to create a magnetic field or to a filament to increase the sample temperature from ambient up to 2000 K, and measuring the temperature with a thermocouple using the others two contacts. The sample can also be cooled to about 120 K using liquid nitrogen. The sample holders (made of titanium, molybdenum or copper doped with beryllium) used for the PEEM measurements need to be able to sustain high voltages and be compatible with ultrahigh vacuum conditions and have to minimize any unwanted stray fields that could affect the emitted electrons trajectories. The whole sample holder is set at -20 kV, while the feed through contact points can be held at a small offset to the high voltage. For the heating experiments, the holder has a tungsten filament situated few millimeters under the sample. A tantalum plate above the filament is used to maintain a homogeneous sample temperature. To perform magnetization reversal experiments, the magnetic field was produced by passing a constant current through a copper wire wound in a coil with an iron yoke. More details about the characteristics of the sample holders can be found in [77].

3.3.4.1. *In situ* PEEM investigations

In order to prevent oxidation of the nanoparticles, the deposition and the X-ray PEEM investigations have been carried out under ultrahigh vacuum conditions. To perform *in situ* studies of the magnetic properties of the NPs under UHV conditions, the ACIS is attached to the PEEM preparation chamber. The base pressure in the PEEM is $< 5 \times 10^{-9}$ mbar for the Fe NP experiments and $< 5 \times 10^{-10}$ mbar for the measurements on Co and Ni particles. During deposition, the pressure rises temporarily to about 3×10^{-6} mbar due to the presence of the Argon/Helium carrier gas. After deposition the pressure drops within a few seconds down to the base pressure. The sample is then transferred *in situ* to the PEEM microscopy chamber with a base pressure of $\leq 5 \times 10^{-9}$ mbar. For the measurement of magnetization curves and for the thermal annealing experiments, the sample holders have been carefully degassed at 500 K for about 20 minutes before the nanoparticles were deposited and no pressure rise was detected during the experiments. Previous spectro-microscopy experiments on individual iron nanoparticles carried out with the present setup revealed pure, metallic iron nanoparticles when operating under these conditions [53]. The chemical cleanliness of iron particles prepared with the ACIS cluster source has been further confirmed in earlier spectroscopy experiments [78]. Thus, there is no indication that the particles are initially oxidized in our experiment.

The photon energies used for resonant excitation of the L_3 edges are 708 eV for Fe, 778 eV for Co and 852 eV for Ni. Elemental contrast images are obtained by recording two images for each sample: First, an image is recorded with the photon energy tuned to the respective L_3 X-ray absorption edge, e.g., to 708 eV for the Fe particles. In such images, the lithographic markers are clearly visible, but the particles are difficult to recognize due to their low signal to background ratio, cf. Fig. 3.5(a). Then, a second so-called pre-edge image is recorded with the photon energy set a few eV before the absorption edge (703 eV for Fe) (not shown). A pixelwise division of the edge and pre-edge images ensures that the observed contrast truly arises from the Fe particles, while removing any background contribution, as can be seen in Fig. 3.5(b) [53]. In this image, most of the bright spots correspond to individual NPs, as determined by subsequent SEM observations of the same areas [Fig. 3.5(c)]. Elemental contrast images of the Co and Ni particles are obtained in an analogous way.

Chapter 4

Data analysis

In this chapter a short introduction to data analysis will be given. Three MATLAB program codes used to identify, select, and extract the XMCD contrast of the particles from the magnetic images will be briefly presented and explained.

To obtain quantitative information from magnetic contrast images, it is required to record PEEM images with the highest possible image quality by aligning the microscope and fast recording of the images. As mentioned before in Chapter 3, in order to minimize the time to switch the X-ray light polarization to within few seconds and effectively reduce drift effects when recording magnetic contrast images, two insertion devices providing intense radiation with variable polarization are operated in the so-called tune/detune mode [66] (See Fig. 3.7). A general intensity difference of about 10% in images recorded with both ID's at opposite polarization obtained in this way, has to be taken into consideration when attempting to determine the XMCD asymmetry of the nanoparticles as discussed below. To obtain high quality images, first the image intensifier unit of the PEEM is set to give an overall image intensity value to about 2100 counts for an exposure time of $t_{exp} = 1$ s, corresponding to about one half the 4096 maximum possible counts in the 12 bit CCD camera. Second, in order to

reduce noise in the image, a number of $N_{ave} = 10$ such images are recorded one after each other and averaged. Third, to remove any background which can arise from the microscopy transfer function or morphological features and inhomogeneities of the sample, or illumination effects in the averaged image, normalization images are recorded in the same conditions either (i) at the pre-edge energy or (ii) in a defocuse condition to obtain flat field images. After changing the polarization (or the photon energy, depending on the experiment) another set of $N_{ave} = 10$ images is recorded and averaged. This cycle is then repeated $N_{cyc} = 20$ times to achieve satisfying statistics, which means 20 images for C^+ and C^- polarization with a total acquisition time of about $t_{tot} = 2 \cdot N_{cyc}(t_{exp}N_{ave} + t_{sw}) = 520$ s, considering a switching time of about $t_{sw} = 3$ s. In case of faster changes, the individual averaged images $C_i^{\pm}(N_{ave})$ are also analyzed separately. This gives a typical time resolution of 20 seconds (for the two images C^+ and C^-), neglecting few seconds required for switching the polarization.
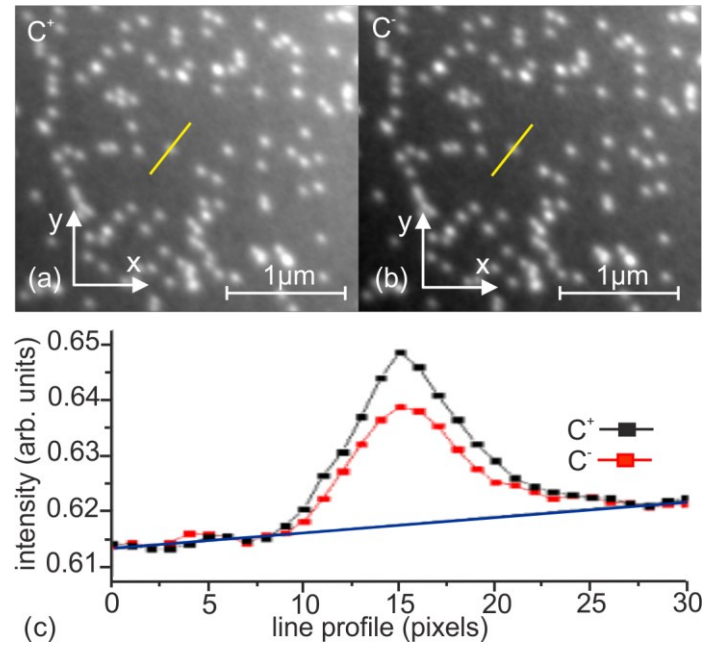

FIGURE 4.1. Normalized (a) C^+ and (b) C^- magnetic contrast images of iron nanoparticles deposited on a Si substrate. (c) The intensity line profile from (a) and (b) of the selected particle after correcting for drift and using a scaling factor of $k = 0.943$. The solid line

denotes the estimated base line. The data yield then $I_{NP}^{+} = 0.031$ and $I_{NP}^{-} \cdot k = 0.021$, which gives $A = 0.19$.

The normalized images reveal an element specific contrast map as shown in Fig. 4.1(a) and (b) for C^{+} and C^{-} polarization. As one can clearly observe in Fig. 4.1(c) the signal of the particles is very small compared to the background intensity (blue line). In addition, the background is not constant but has a flat intensity gradient. This is why in this work the substrate induced background is determined locally, selecting an area of 13x13 pixels^2 around the particle spot. Thus to obtain a precise signal from the particles a plane background plus an elliptical Gaussian are fitted to the particle spots in the images for the automatic analysis of the PEEM data. The Gaussian is given by $I_{Gauss}(x,y) = I_{NP} \exp\left\{ -\frac{x'-x_0'}{2(\sigma_{x'})^2} \right\} \exp\left\{ -\frac{y'-y_0'}{2(\sigma_{y'})^2} \right\}$, with I_{NP} being the magnitude of the nanoparticle spot and $\sigma_{(x,y)'}$ describing the width of the Gaussian in the x' and y' direction, respectively. The latter do in general not coincide with the x and y directions of the image frame. To take a possible rotation by an angle θ into account, the coordinates need to be transformed by $x'-x_0' = \cos\theta(x-x_0) - \sin\theta(y-y_0)$ and $y'-y_0' = \sin\theta(x-x_0) + \cos\theta(y-y_0)$, with x_0 and y_0 being the position of the spot in the image frame. The background is described by a tilted plane according to $I_S(x,y) = a(x-x_0) + b(y-y_0) + c$ with a and b being the slope along the x and y directions, respectively, and c is a constant. The intensity distribution in a suitable small region around the particle spot – normally (13 pixel × 13 pixel) – is then well described by the sum of both contributions as discussed below in the context of Fig. 4.2. We consider $I_0 = I_S(x_0, y_0)$ as a measure of the local incoming light intensity and use this value for normalization purposes.

This fitting procedure is used in three Matlab codes for image drift corrections, particle selection and quantitative data analysis. Here we give a brief introduction into the principles behind these codes.

4.1. Image drift correction

First, the above procedure is applied to a number of intense particles (usually five) in both the individual elemental contrast images obtained from the $C_i^+(N_{ave})$ and the $C_i^-(N_{ave})$ images, respectively. From these fits, the positions x_0 and y_0 of the nanoparticles are determined and the shift relative to the first image in the series is then evaluated. Using suitable interpolation methods all raw images are then shifted with sub-pixel accuracy according to the fits resulting in a drift-corrected stack of $C_i^{\pm}(N_{ave})$ images. The success of this step is visually checked and yields usually a perfectly stable image stack. The drift-corrected images are then averaged and yield $C^{\pm}$ images with a quality similar to panels (a) and (b) of Fig. 4.1. Once the averaged images are corrected for drift, the same method is used once again to correct the drift between the different averaged images, so that at the end the particles have the same position for all images from one experiment.

4.2. Particle selection

Once all the images are corrected for drift, the second Matlab tool, which is based on the same fitting model, is used to select the particles of interest and to determine their positions in the images. The Matlab tool enables to analyze many particles sequentially. The output is a data file with the position of all selected particles which will be used for the quantitative analysis. This is important for automated data analysis of large image stacks.

4.3. Quantitative analysis

To obtain the magnetic asymmetry of the particles, one needs to determine I_{NP}^+ and I_{NP}^- by applying the above mentioned model to both C^+ and C^- images. First, both images are normalized with the same pre-edge image (defined in Chapter 3). Since edge and pre-edge images have similar intensity values, this normalization gives a value close to 1 and has to be scaled up to match the 16 bit value range as shown for a given particle in Fig. 4.2(a) and (b).

The divided image is shown in Fig. 4.2(c). In order to determine the exact values of the particle intensity it is assumed that all parameters regarding the particle shape ($\sigma_{(x,y)'}, \theta$) and the particle position (x_0, y_0) are the same for both images and that the flat intensity gradient given by a and b are the same in the C^+ and C^- images. In order to correct the above mentioned intensity difference between both images and obtain a good correction factor k, the C^- image is scaled by k, such that the calculated difference image $XMCD = C^+ - k \cdot C^-$ yields a Gaussian with an intensity $I_{diff} = I_{NP}^+ - k \cdot I_{NP}^-$ and the same shape parameters as the individual spots, but on a flat background with zero intensity. This is illustrated in Fig. 4.2, where the experimental C^+ image is shown in panel (d), the scaled experimental image $k \cdot C^- = C_{corr}^-$ in (e), and the respective difference image in (f). The respective fit results are given in Fig. 4.2(g)-(i). The success of the fit routine is checked by plotting the calculated residuals, i.e. the difference between the experimental and the fitted data. As seen in Fig. 4.2(j)-(l) they reveal just white noise without signatures of a systematic deviation from the fit model. The Matlab routine used for these fits allows sharing various parameters among up to 32 particles at a time. The correction factor is always about $k \sim 0.9$ and reflects the above mentioned intensity differences of the both IDs. It varies only little between different particles or experiments. The fit procedure results in mean values of the particle intensity with relatively small statistical error bars of about 30 counts compared to the general image intensity which corresponds to about 32,000 counts in Fig. 4.2, which suggests an accuracy of about 0.1% in an intensity measurement with the current setup.
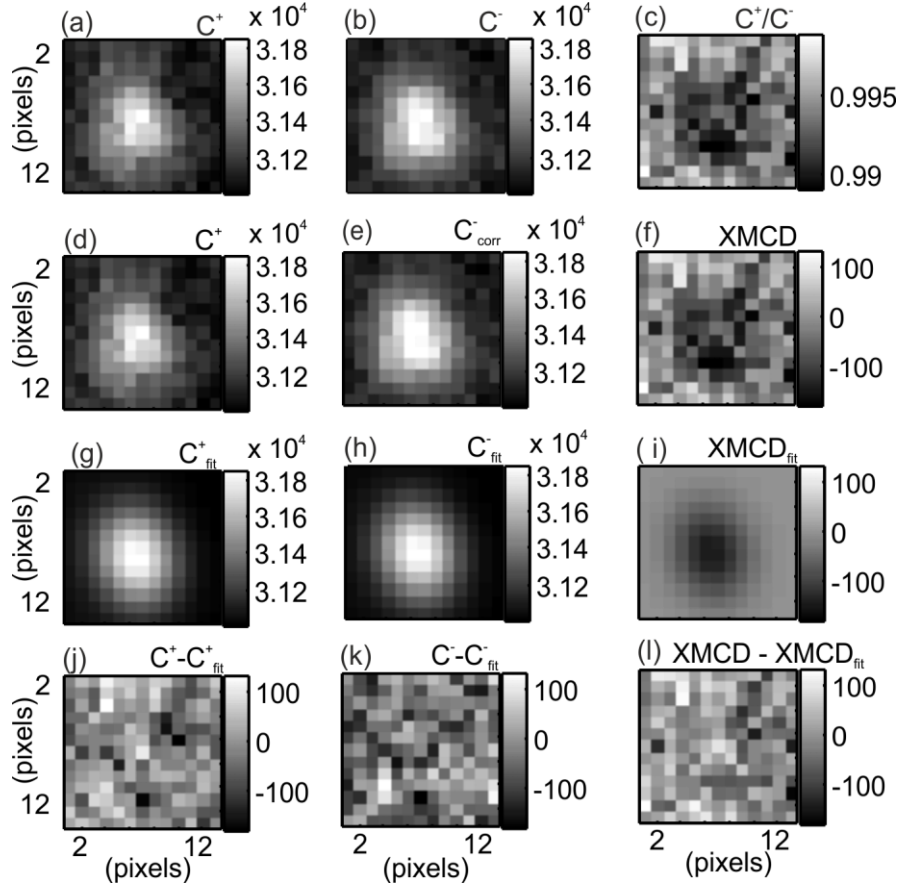
FIGURE 4.2. (a) Pre-edge normalized C^+ image of the selected Fe NP in Fig. 4.1. (b) Pre-edge normalized C^- image of the selected Fe NP in Fig. 4.1. (c) Divided (C^+/C^-) magnetic contrast image of the selected Fe NP in Fig. 4.1. (d) same as (a). (e) corrected C^- image scaled by a factor k which is obtained from the fit of (b), and (f) the respective divided image [(d) divided by (e)]. (g) – (i) fits to the data in (d) – (f). (j) – (l) differences between the fits [(g) – (i)] and the experimental data [(d) – (e)].

However, a better estimate of the statistical error associated with these measurements is obtained when taking multiple measurements of the same particle under identical conditions. This is illustrated in Fig. 4.3, where a sequence of 50 measurements of one particle is plotted. The data reveal a normalized intensity of the order of 0.05, i.e. the particle gives rise to an intensity of about 5 % above the background level. With the given data quality, the fit yields a statistical error of only 0.0005, i.e. of the order of 1% of the particle signal, which corresponds to the size of the plotted symbols. However, the scattering of the data points is clearly much larger than the individual statistical error. The scattering data can be fitted with

43

a Gaussian being plotted as the red line in the Fig. 4.3 (b). The Gaussian width is of the order of 0.003, i.e. about 6 times larger than the statistical error in the individual data point. In fact, it is this scattering which limits the accuracy in our data analysis. When analyzing the respective image stacks we found that these variations are related to weak meandering patterns, which might be attributed either to X-ray induced surface reactions or temporal variations in the image intensifier unit. While this could be improved in the future, we want to remark here that these variations contribute to much less than 1% to the total image intensity, and thus are hardly observed in many common PEEM studies. For the present work we just multiply the standard deviations of our data with a factor of five in order to reflect a realistic accuracy of our experiments.
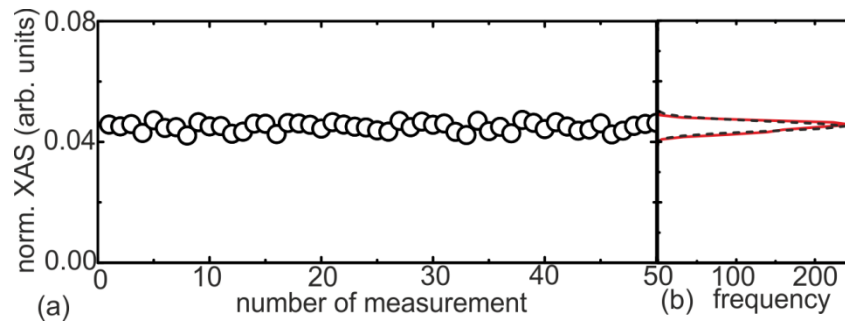
FIGURE 4.3. (a) Normalized intensity measurements of one particle with linearly polarized x-rays. The acquisition time for one data point is 30 seconds. (b) Histogram (dashed line) and fitted Gaussian (solid red line).

Chapter 5

Fe nanoparticles on Si

Adapted from [18,62], this chapter presents a detailed study on the structural and magnetic properties of individual Fe nanoparticles deposited on a passivated Si substrate. Studying the magnetization of individual Fe nanoparticles by magnetic spectro-microscopy as a function of the applied magnetic field, temperature and at different angles determining the exact orientation of the magnetic moments of the particles, resolves the apparently contradictory observations found in literature revealing that superparamagnetic and ferromagnetic blocked nanoparticles can coexist in the investigated size range of 8-20 nm. Spontaneous transitions from the blocked state to the superparamagnetic state are observed in single particles and suggest that the enhanced magnetic energy barriers in the ferromagnetic particles are due to metastable, structurally excited states with unexpected long life times. A detailed overview on the all possible magnetic anisotropy contributions is also presented.

Magnetic NPs can show a variety of unusual magnetic phenomena when compared to the bulk materials, such as enhanced magnetic moments and magnetic anisotropies, mostly due to the large role played by surface/interface and finite-size effects [8,9]. With respect to Fe NPs in the size range from 8 to 20 nm, enhanced magnetic energy barriers have been reported in

literature by several authors [10,79-81], while others have found bulk-like magnetic anisotropy energies (MAE) [82-84]. Whether the ferromagnetic or the superparamagnetic form is predominantly found in an experiment may depend on the details of sample preparation, e.g. on whether the samples have been annealed at higher temperatures or not. The reported magnetic properties may vary due to different factors such as integrated ensemble versus single particle measurements, isolated in a non-interacting matrix versus deposited particles or oxide/iron versus pure Fe particles, all of which have to be considered in order to make a general statement about these particles. Interestingly, regarding the structure of these particles, most studies report that the iron particles possess the bcc lattice structure known from bulk iron, irrespective of the magnetic properties found. This suggests that rather subtle, local distortions of the bcc lattice are sufficient to significantly alter the magnetic properties of the iron nanoparticles. Indeed, large uniaxial anisotropies have recently been predicted for iron when breaking the cubic symmetric of the bcc lattice [85]. Possible candidates for such distortions could be metastable dislocation structures that arise to accommodate local strain induced when bringing a nanoparticle into contact with a substrate – even when mild conditions such as 'soft landing' deposition are warranted [86,87].

In order to have a direct experimental access to structural higher energy states and check their impact on the magnetic properties, it is mandatory to do experiments with single particle resolution. Monodisperse nanomagnet ensembles are not enough, since even they can show considerable particle-to-particle variations in their properties either due to size effects, inter-particle interactions, their individual interfaces with the environment or surface effects [82]. Experiments with single particle sensitivity enable one to disentangle the different contributions, and thus, distinguish lower or ground state properties from higher energy states [14,17].

Another aspect which has to be considered when studying Fe NPs concerns their chemical reactivity with oxygen [88]. In some early experimental studies which consider the oxidation of Fe particles, the properties of iron oxide/iron core particles [89] indicate an increased intrinsic complexity when compared to pure Fe particles due to strain and possible magnetic interactions with the polycrystalline iron oxide shell [90].

46

Considering all these aspects, this chapter is focused on the *in situ* study of the magnetization of individual iron (Fe) nanoparticles by magnetic spectro-microscopy, trying to elucidate the source of the controversies found in literature. Gas-phase prepared Fe NPs that are soft-landed under UHV conditions onto chemically inert substrates, as described in Chapter 3, provide chemical cleanliness and a structure which is close to that of thermal equilibrium. These Fe particles deposited *in situ* onto Si substrates are considered as prototypical model systems, giving insight into the properties of undistorted, isolated nanoscaled systems. We will demonstrate that these particles can show an unusually high magnetic anisotropy as compared with bulk Fe, displaying both ferromagnetically blocked or superparamagnetic states at room temperature, irrespective of their size, in contrast to the anticipated size-related scaling laws. The high anisotropy state was found to be metastable and was assigned to a structurally excited state.

5.1. Structural characterization of Fe particles

5.1.1. TEM

In earlier reports, the structure and morphology of Fe NPs in the present size range have been studied experimentally with TEM. Pure Fe particles in a non-interacting environment confirmed the expected ground state configuration: bcc Fe with {100} and {110} facets according to a Wulff construction [91,92]. This is consistent with the expected Fe NPs structure when prepared with the ACIS described in Chapter 2 [54,78]. Deviations from this structure have been found for particles smaller than 2 nm [93], or when kinetic barriers or interfaces govern the growth, such as in chemical synthesis techniques, where cubes with {001} facets are frequently synthesized, cf. [94], or due to sintering when pre-formed NPs come in contact with each other and form agglomerates [95].

TEM measurements on Fe NPs embedded in an Al matrix [54,78] show that the particles have a Wulff shape. Recent high resolution scanning transmission electron microscopy (HRSTEM) measurements on ACIS Fe particles deposited onto 10 nm thick SiN membranes carried out at EMAT [59] reveal single crystalline Fe cores without visible structural defects.

5.1.2. RHEED

The RHEED pattern of Fe NPs deposited on the passivated Si substrates [Fig. 5.1(a)] reveals Laue diffraction rings which indicate randomly oriented Fe particles with a bcc lattice.
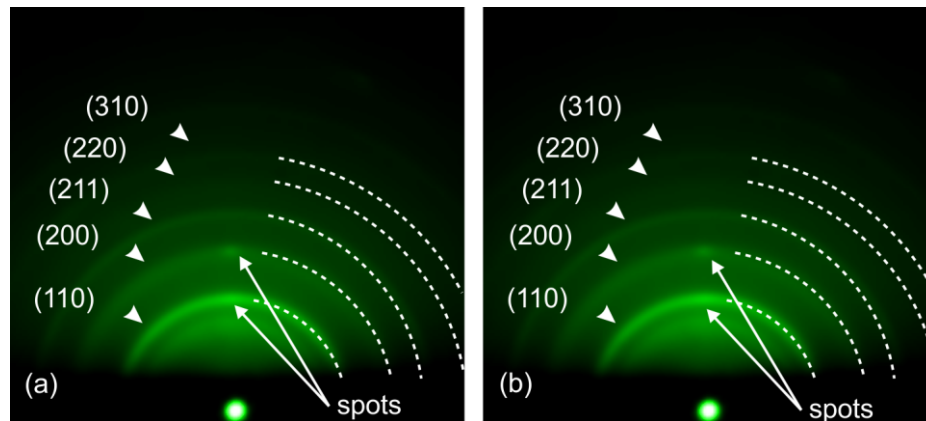

FIGURE 5.1. (a) *In situ* RHEED diffraction patterns of supported Fe NPs with a mean size of about 12 nm on a Si wafer at room temperature and (b) at 500°C. Adapted from [62].

A detailed discussion of the diffraction pattern of supported NPs in the RHEED geometry can be found in Ref. [56]. Similar to previous investigations on Fe NPs deposited onto a single crystalline W(110) surface [56], it is found that a preferred texture exists for the (200) and the (110) ring. This indicates that the NPs preferentially rest with their {001} and {110} facets parallel to the substrate surface. The full RHEED pattern reveals further an intact, flat, and amorphous SiO_x surface layer (See Fig. 3.7).

The thermal stability of this configuration on the surface is investigated by increasing the temperature of the sample. It is observed that the full RHEED pattern remains stable for temperatures up to 500°C [Fig. 5.1(a) and (b)]. This finding indicates a high stability of the substrate surface as well as of the crystallographic structure and the random orientation of the particles. At higher temperatures a sudden transition from Laue rings to well-defined diffraction spots [Fig. 5.2(a)] is observed. At the same time the substrate pattern changes significantly, which is assigned to the thermal decomposition of the SiO_x layer. This decomposition enables a significant chemical reaction of the particles with the Si substrate [Fig. 5.2(b)], which results in an epitaxial relation of the particles with the bare Si(001) surface. These observations suggests that when depositing Fe NPs at room temperature, the

SiO$_x$ layer is indeed preserved and chemical interactions of the particles with the Si substrate are suppressed, so that our samples represent nanoparticles in contact with a chemically inert substrate. Also, no deviation from the random orientation and the bcc lattice structure of the particles is detected up to 500°C [See Fig. 5.1(b)].
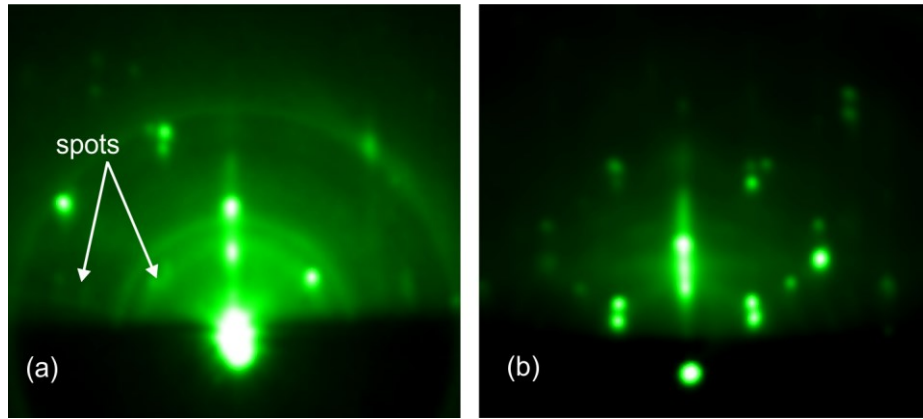

FIGURE 5.2 *In situ* RHEED diffraction patterns of supported Fe NPs with a mean size of about 12 nm on a Si wafer at 800°C and (b) at room temperature after annealing to 800°C.
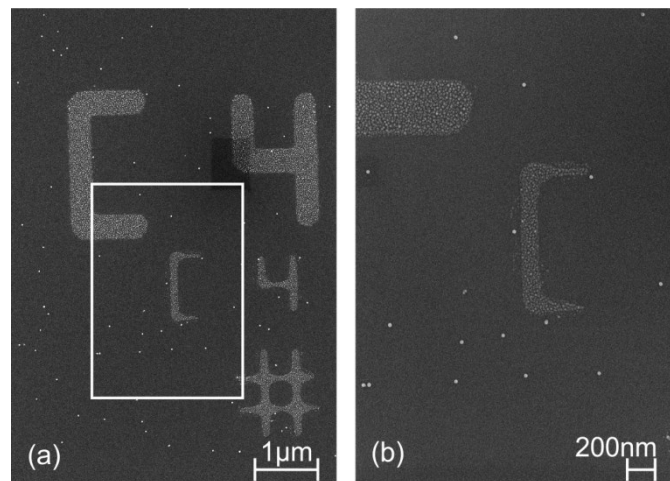
5.1.3. SEM

FIGURE 5.3 (a) E*x situ* SEM overview image of supported Fe NPs on a Si wafer. (b) The highlighted area in (a).

The SEM image in Fig. 5.3 presents a typical deposit of the Fe particles. The particle density for the PEEM experiments amounts to a few NPs per μm^2. The deposition parameters were

set such that the particle-to-particle distances are about a few hundred nm to ensure the absence of magnetic dipolar interactions between the particles. SEM further confirms a nearly random spatial distribution of the particles, which reflects the stochastic nature of the deposition process and a reduced particle mobility on the surface.
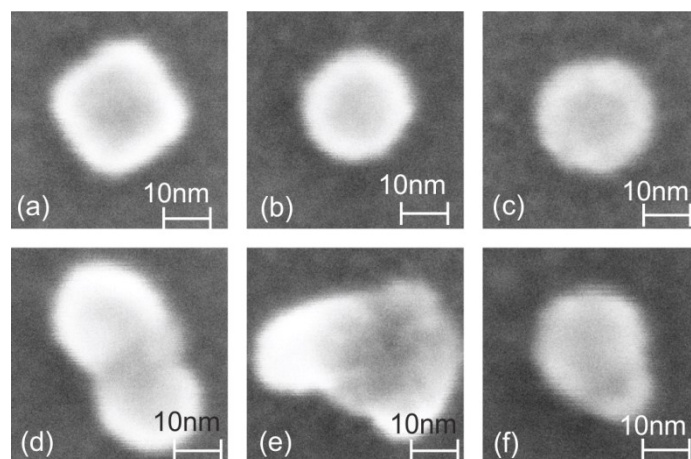

FIGURE 5.4. High resolution SEM images of individual Fe NPs (a)-(c) typical well-shaped particles, which are selected for further analysis. (d)-(f) non-ideal-shaped particles, which are excluded from further analysis.

At higher magnification, SEM reveals the co-existence of (i) compact, well-shaped particles as shown in the Fig. 5.4(a)-(c), and (ii) non-ideal-shaped particles as illustrated in Fig. 5.4(d)-(f). As expected from the soft-landing deposition conditions, no indication of particle fragmentation is found.
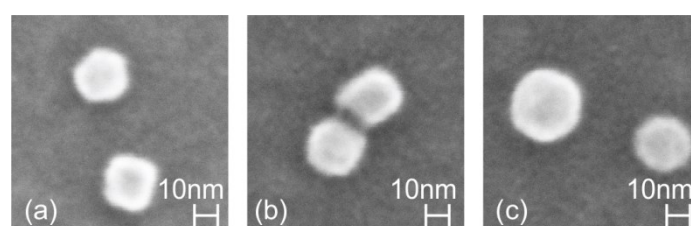

FIGURE 5.5. (a)-(c) High resolution SEM image of close-lying Fe NPs, which are excluded from further analysis.

For the magnetic analysis we only consider particles with a well-defined, compact shape [Fig. 5.4(a)-(c)]. Close-lying (Fig. 5.5) and odd-shaped particles [Fig. 5.4(d)-(f)] as well as agglomerates of smaller particles are excluded from the analysis.
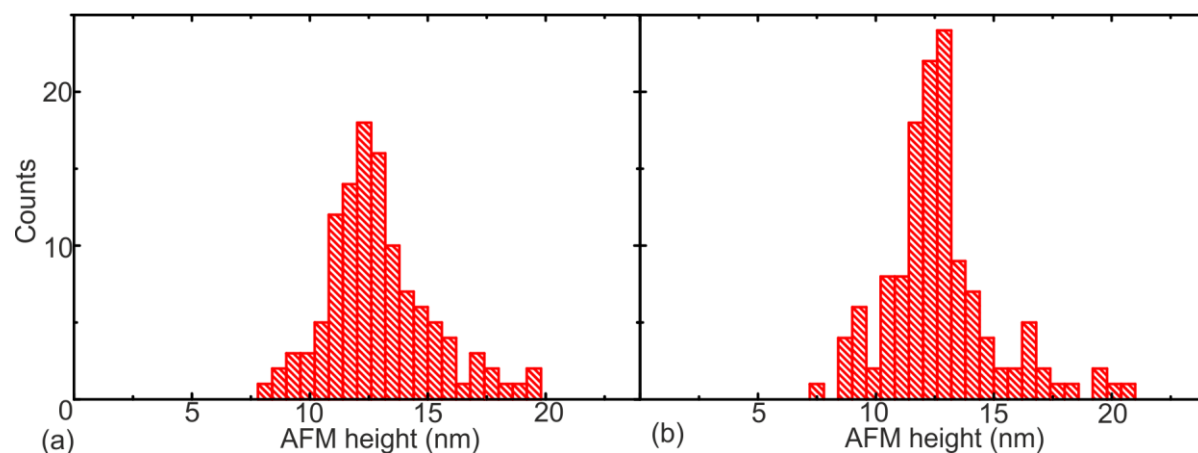
5.1.4. AFM

FIGURE 5.6. AFM height distributions of the well-shaped Fe particles for two different samples, (a) and (b), revealing the same mean particle height of 12 nm.

AFM measurements of the selected, well-shaped particles of different samples reveal a mean particle height of 12 nm (See Fig. 5.6), without correction for the oxide shell, which has a typical thickness of about $2 - 3$ nm and forms upon exposure to air [91]. Thus, the actual Fe particle size might be somewhat smaller. The size of the particles is determined from a Gaussian fit to the measured height profile of each individual particle in AFM (Fig. 5.7). The full distribution of particles sizes (heights) ranges from 8 to 20 nm (Fig. 5.6).
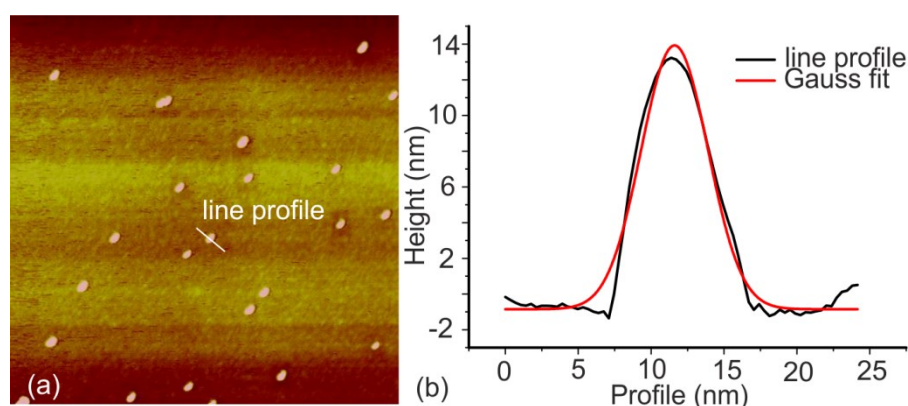

FIGURE 5.7. (a) *Ex situ* AFM overview image of supported Fe NPs on Si. (b) The AFM height profile of the selected particle in (a) with the corresponded Gaussian fit.

5.2. Magnetic properties

An elemental contrast image of Fe NPs obtained with PEEM from the division of the image recorded at 708 eV with a pre-edge image at 703 eV is shown in Fig. 5.8(a). The bright spots correspond to the Fe particles on the Si substrate.
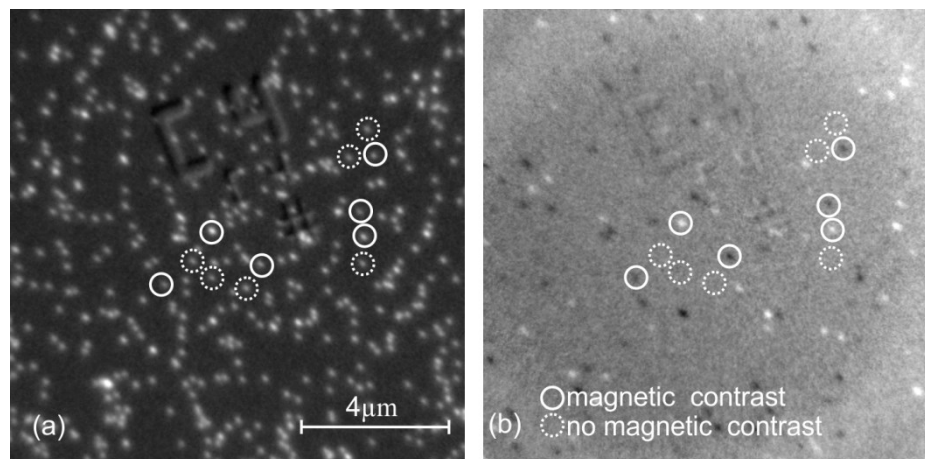

FIGURE 5.8. (a) X-ray PEEM elemental contrast image of Fe NPs (white dots) randomly deposited on a Si wafer. (b) Corresponding XMCD contrast image. One third of all the particles show visible magnetic contrast (e.g. particles with white circles) while others (dashed circles) reveal no magnetic contrast. The images are recorded *in situ* at room temperature. Adapted from [18].

Employing the XMCD effect as described in Chapter 3 one can determine the magnetization of the particles from the magnetic contrast images, as illustrated in Fig. 5.8(b), where the intensity of a particle (Eq. 3.2) depends on the projection of its magnetization $\vec{m}$ on the X-ray propagation vector $\vec{k}$. Comparing the magnetic contrast image with the respective elemental contrast image shown in Fig. 5.8(a) allows one to correlate a magnetic signal with individual nanoparticles. In this way one can observe that a number of Fe NPs exhibit stable magnetic contrast, which varies from white ($\vec{m}$ parallel to $\vec{k}$) to black ($\vec{m}$ antiparallel to $\vec{k}$), while the rest of the particles show no magnetic contrast, i.e., appearing grey similar as the background, cf. Fig. 5.8(b).
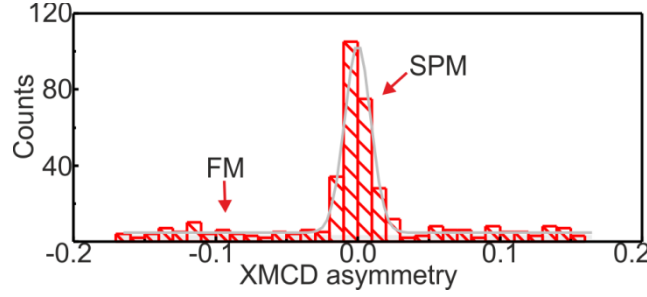
FIGURE 5.9. Distribution of normalized XMCD contrast values obtained from the data in Fig. 5.8(b). Adapted from [18].

To gain a more quantitative insight into the magnetic properties of the sample, the XCMD asymmetry (Eq. 3.3) of each particle is determined. Upon plotting these values, the distribution of the normalized XMCD contrast of the individual particles is obtained, which yields a peak at zero XMCD contrast on top of a flat distribution of finite contrast values A ranging from -0.17 to 0.17 (indicated by the gray horizontal lines), as shown in Fig. 5.9. Typically, about 60% of the particles show no magnetic contrast ($|A| \leq 0.03$).

For a better understanding of such histograms, numerical simulations of the magnetic contrast distribution in magnetic NP ensembles with different properties are performed. In these simulations, the particles are considered with static magnetization (i.e. ferromagnetically blocked). The orientation of the magnetic unit vector is given in spherical coordinates by (θ_m, ϕ_m) with $0 \leq \theta_m \leq \pi$ and $0 \leq \phi_m \leq 2\pi$. The normalized magnetic contrast of a particle in X-ray PEEM is then calculated in accordance to the actual experimental geometry, cf. Fig. 3.11. For the simulations, we have considered three different possible scenarios: (a) a fully random orientation of the magnetic moments in space (with $0 \leq \theta_m \leq \pi$ and $0 \leq \phi_m \leq 2\pi$), (b) a preferred in-plane magnetization of the particles with random orientation in the surface plane (with $\theta_m = \frac{\pi}{2}$ and $0 \leq \phi_m \leq 2\pi$), and (c) a preferred out-of-plane magnetization of the particles, where we allowed a standard deviation of 45° from full out of plane orientation (OOP) of the moment to mimic a realistic sample with deviations from perfect alignment of the magnetic moments (OOP 'up' around 0° with $0 < \theta_m < \frac{\pi}{4}$ and $0 \leq \phi_m \leq 2\pi$; or OOP

'down' around 180° with $\frac{3\pi}{4} < \theta_m < \pi$ and $0 \le \phi_m \le 2\pi$). As shown in Figs. 5.10(a)-(c) the three scenarios result in considerably different distributions of the normalized XMCD contrast and thus histograms such as in Figs. 5.10(a)-(c) contain a clear signature of specific magnetic configurations. Comparing the experimental result in Fig. 5.9 with the simulated data in Fig. 5.10 allow us to assign the flat contribution to randomly oriented magnetic moments and to exclude that possible flattening of the particles following deposition occurred which would cause noticeable shape anisotropy and a preferred in-plane magnetization. This is also confirmed by the angular measurements discussed in 5.2.1.2 section. Further, the peak at zero magnetic contrast cannot be assigned to a preferred out-of-plane orientation of the magnetic moment. As seen in Fig. 5.10(c) the experimental geometry would then lead to two distinguishable peaks for "up" and "down" oriented particles, which are not observed in our experimental data.

These considerations suggest that the experimentally observed distribution of XMCD contrast values – in particular the peak at zero contrast - is not due to a specific preferred magnetic orientation of ferromagnetically stable particles on the surface, but rather indicates two distinct classes of behavior: randomly oriented ferromagnetic and superparamagnetic particles.

The experiments reveal that the ferromagnetic NPs have at RT a magnetic relaxation time τ much longer than the experimental measurement time of 20 s and are referred to as FM particles. In fact, these magnetically blocked states were observed over many hours. The other fraction of particles shows no magnetic contrast under these conditions. As discussed in Chapter 2, the orientation of the magnetic moment of these nanoparticles might vary as a function of time in a stochastic manner due to thermal excitations. Particles with a relaxation time which is shorter compared to the time which is required to record a magnetic contrast image will show no magnetic contrast, i.e. reveal a grey tone similar to that of the background in Fig. 5.8(b), since their magnetic contrast averages out during the time period $\tau_{\exp}$. Such particles are referred to as SPM and cause a peak at zero contrast in histograms such as that shown in Fig. 5.9.
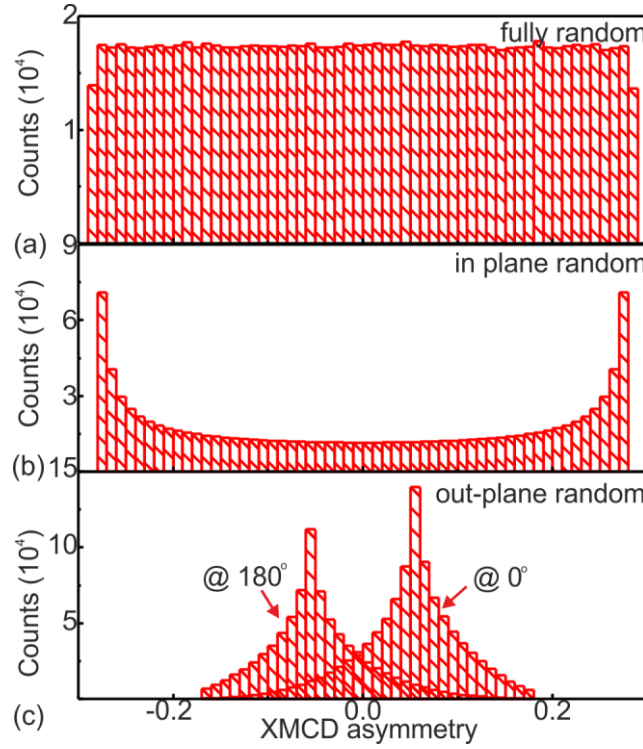
FIGURE 5.10. Numerical simulations of the XMCD asymmetry distribution for (a) isotropic, (b) in plane or (c) out of plane randomly orientated magnetic moments according to the experimental geometry shown in Fig. 3.10. Each simulation was performed for 1,000,000 particles. Adapted from [62].

5.2.1. Magnetic anisotropy energy - Experiments

5.2.1.1. Applying an external magnetic field: Magnetization curves

To obtain further insight into the properties of the particle ensemble, an external magnetic field H is applied as indicated in Fig. 3.10 and the normalized XMCD contrast as a function of H is recorded. Note that the imaging is done under an applied field. It is found that most of the particles which show initially no magnetic contrast can be magnetized by applying a few mT as shown in Fig. 5.11. This behavior confirms that these particles carry a magnetic moment. The absence of a remanent magnetization is characteristic of superparamagnetism, cf. Fig. 2.8.
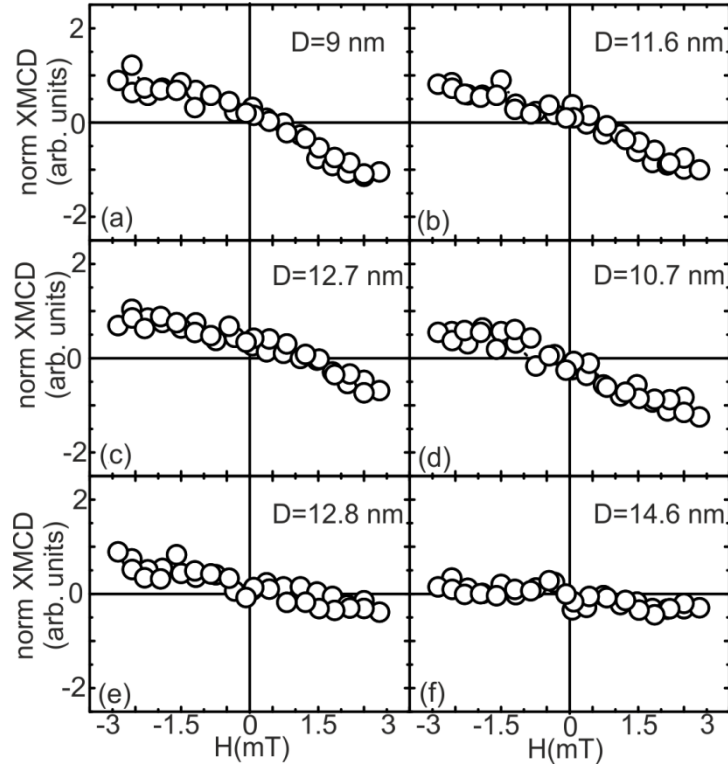
FIGURE 5.11. (a) – (f) Response of individual SPM particles with different sizes D which show no magnetic contrast at RT for $H = 0$ mT to a sequence of applied magnetic fields ($\phi_s = 0°$). The particles are magnetized by applying a small magnetic field of few mT. The full cycle is recorded over a time of about 10 hours. The magnetic response of a particle is given by its field dependent normalized XMCD contrast (circles).

Most of the particles which show magnetic contrast without magnetic field at room temperature (FM zero field state represented by red circles in Fig. 5.12), change their contrast only slightly or switch their contrast at some field values from "white" to "black" or *vice versa* [Fig. 5.12 (a)-(d)]. Switching occurs here via thermal excitation, which is promoted by a reduction of E_m due to the applied magnetic field. The Zeeman energy is less than 0.1 eV for the present particles and fields.
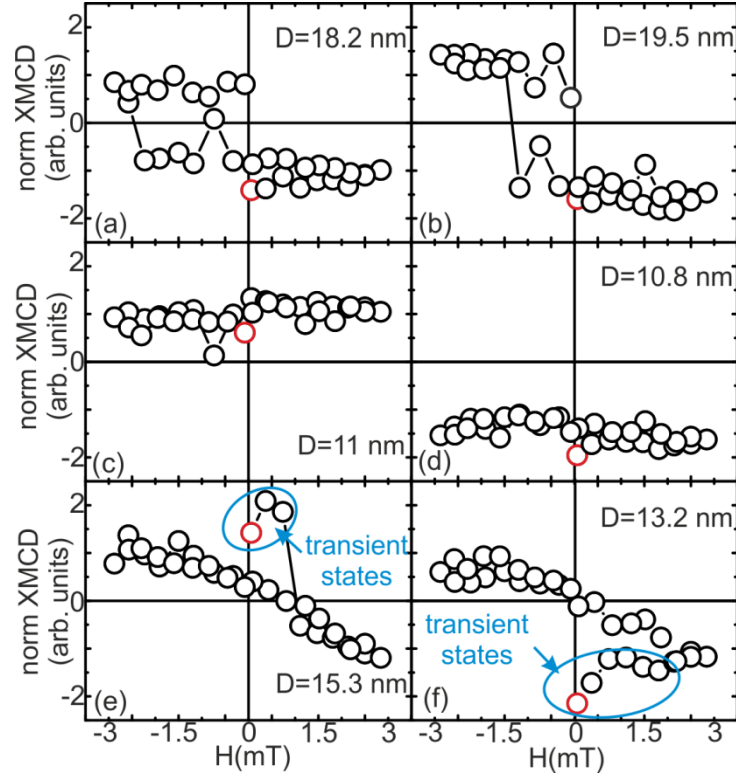
FIGURE 5.12. (a) – (f) Response of individual FM particles with different sizes D to a sequence of applied magnetic fields ($\phi_s = 0°$). The red circle is the magnetic contrast at RT for H = 0 mT. The full cycle is recorded over a time of about 10 hours. The magnetic response of a particle is given by its field dependent normalized XMCD contrast (circles). Three types of magnetization curves are found: (i) switching of the magnetization from initially "black" to "white" or vice versa (a) and (b); (ii) constant magnetization (the same as in the initial state for all the cycle) (c) and (d); (iii) spontaneous transitions from (initially "white" and "black") FM states to SPM behavior (e) and (f).

Some of the particles show a spontaneous transition from ferromagnetic to superparamagnetic behavior as seen in Fig. 5.12(e) and (f). In both cases the particles are initially ferromagnetically blocked, but after some time their magnetization starts to approach the response of the superparamagnetic particles. Magnetization curves such as in Fig. 5.12(e) and (f) reveal further that the transition occurs spontaneously, but may evolve via transient states which give rise to jumps in the magnetization curves. This suggests that the ferromagnetic phase is metastable and may spontaneously decay into to the ground state/equilibrium superparamagnetic phase. The transition appears irreversible, since in the

experimental data no initially superparamagnetic particle shows an inverse transition to ferromagnetism.

5.2.1.2. Rotating the sample: Orientation of the magnetization

The magnetic state of the particles is further confirmed by observing the normalized XMCD as a function of the azimuthal sample orientation ϕ_s at $H = 0\,$mT. The SPM particles show no contrast at any orientation as can be seen in Fig. 5.13, while the FM particles show an angular dependence according to $\gamma(\vec{k} \cdot \vec{m})$ as shown in Fig. 5.14.
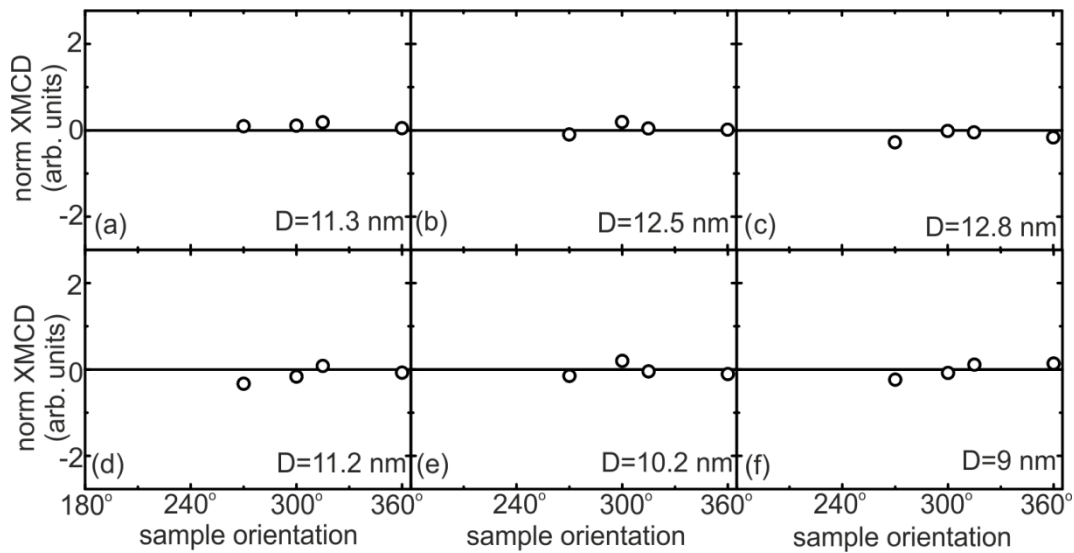

FIGURE 5.13. Normalized XMCD recorded as a function of the azimuthal sample orientation for SPM particles with different sizes D. The black circles are the experimental data which show no contrast at any orientation.
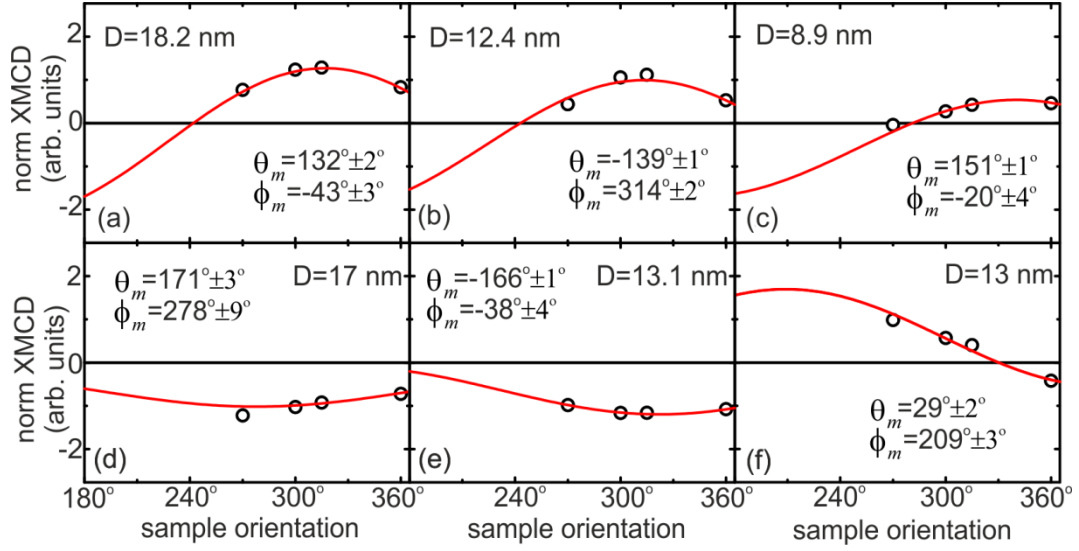
FIGURE 5.14. Normalized XMCD recorded as a function of the azimuthal sample orientation for FM particles with different sizes D. The black circles are the experimental data and the red curve is the fit which gives the orientation of the magnetic moment of the particle (See Inset).

Fitting the data for four sample orientations allowed us to obtain the orientation of the magnetic moment of the particle as can be seen in Fig. 5.14. The next step was to estimate the MAE of the nanoparticles by varying the temperature.

5.2.1.3. Heating and cooling experiments: Estimating the blocking temperature

By changing the temperature, the MAE of nanoparticles can be determined by measuring their blocking temperature T_B, the temperature at which the transition from ferro- to superparamagnetism occurs. Below T_B the particles are in a FM state with the magnetic moments fixed in a given state for periods much longer then the experimental measurement time $\tau_{\exp}$. Above T_B the magnetic moments fluctuate due to thermal excitations, leading to a relaxation time shorter than $\tau_{\exp}$. The anisotropy energy is obtained from (Eq. 2.5) as

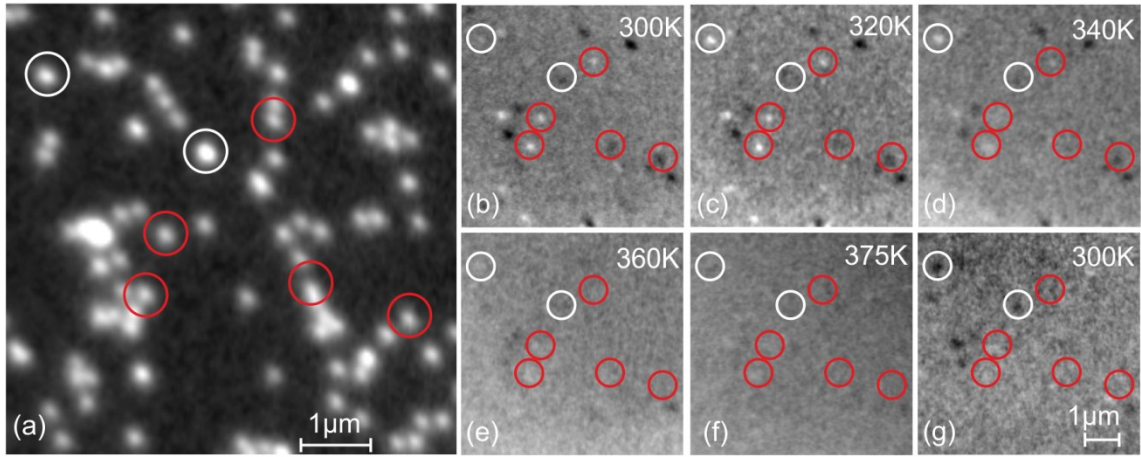$$E_m = T_B k_B \ln(\nu_0 \tau_{\exp}) .$$

FIGURE 5.15. Heating experiment I. X-ray PEEM images: (a) elemental and (b) to (g) magnetic contrast images of Fe nanoparticles on Si substrate at different temperatures. (b)-(f) Evolution of magnetic contrast with temperature. (g) Magnetic contrast upon subsequent cooling to RT. Adapted from [18].

To evaluate the actual energy barrier of the ferromagnetic particles, the sample temperature is raised in order to observe the onset of thermal fluctuations of the particle magnetization. An elemental contrast image of the sample is shown in Fig. 5.15(a). The corresponding XMCD contrast images of the heating sequence are shown in Figs. 5.15(b) – (g). Most of the ferromagnetic particles start to alter their magnetic contrast already at 340 K and lose their contrast fully between 360 K and 375 K [Figs. 5.15(b) – (f)]. The latter occurs when the relaxation time of the particles becomes comparable to or shorter than the experimental time resolution: $\tau \leq \tau_{exp}$. For a better visualization some particles are highlighted with circles in all images.

Upon cooling the sample to room temperature [Fig. 5.15(g)] only about one third of the initially FM particles (white circles) recover their magnetic contrast. The other fraction shows an irreversible phase transition from FM to SPM. This is also assigned to the metastable nature of the FM state. Some of the particles with reversible FM-SPM transition have reversed their magnetization resulting in a reversed magnetic contrast, for example from white to black, demonstrating that thermally activated reversals of the magnetization have occurred during the experiment. From the loss of the magnetic contrast (at 370 K) of the reversible NPs we can estimate their MAE of about 0.83 eV.
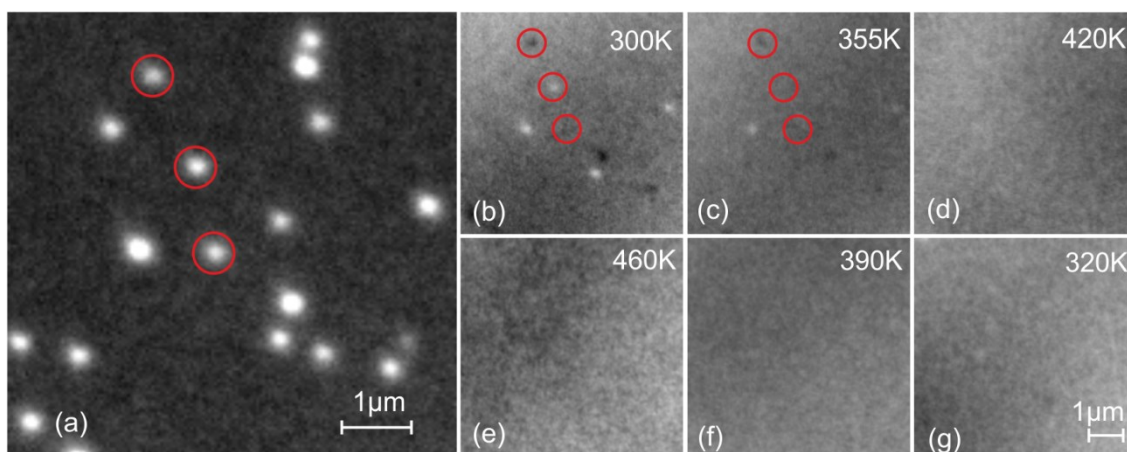
60

FIGURE 5.16. Heating experiment II. X-ray PEEM images : (a) elemental and (b) to (g) magnetic contrast images of Fe nanoparticles on a Si substrate at different temperatures.

It is further observed that when heating the sample to 460 K all initially ferromagnetic particles irreversibly loose their magnetic contrast (Fig. 5.16). This suggests that another thermally induced but irreversible structural relaxation mechanism is present in the particles which significantly alters the magnetic properties. This relaxation and its impact on the magnetic properties was also seen at room temperature in the applied field experiments [Fig. 5.12(e) and (f)]. These observations suggest that a similar transition occurs in the temperature dependent experiment above.
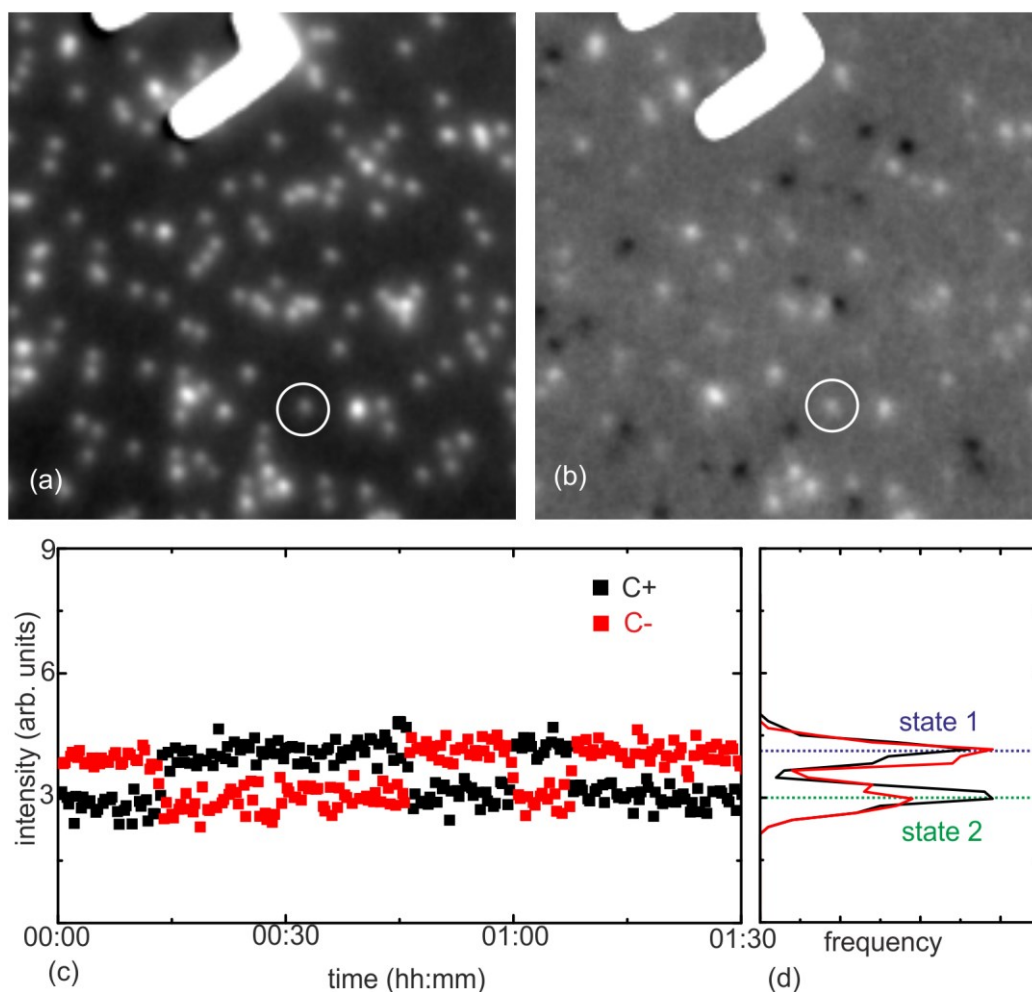
FIGURE 5.17. (a) Elemental contrast image recorded with circularly polarized light at the Fe L_3 edge. (b) Corresponding XMCD contrast image. (c) Temporal evolution of the intensity of the selected particle as denoted in (a), showing direct observation of thermally induced fluctuations between two states. The light polarization was switched sequentially as indicated by red and black symbols. Four switching events between two distinct states are clearly visible. The time resolution is about 10 seconds. (d) Histogram showing the intensity distributions for both polarizations. Both states are almost equally populated during the observation time.

The experiments above reveal the magnetic phase of the particles and give a lower estimate of the energy barriers in the reversibly ferromagnetic particles. However, they do not yield information about the character of the different magnetic states and therefore the magnetic anisotropy (e.g. uniaxial or cubic). Experimentally, the nature of the magnetic anisotropy can be elucidated upon observing thermally induced fluctuations directly in time [46]. Such

62

observations are possible when the magnetic relaxation time of a particle is larger than the experimental time resolution but shorter than the available time frame for an experiment (several hours). With sufficiently long observation times thermally induced magnetic flipping events of the particles were found at room temperature (Fig. 5.17). The majority of these particles switch clearly between two states with different XAS intensity for C^+ and C^- polarization as shown in the Fig. 5.17(c), which indicates a dominant uniaxial anisotropy contribution. Note that during the observation time in Fig. 5.17 the particle flips its magnetization only a few times.
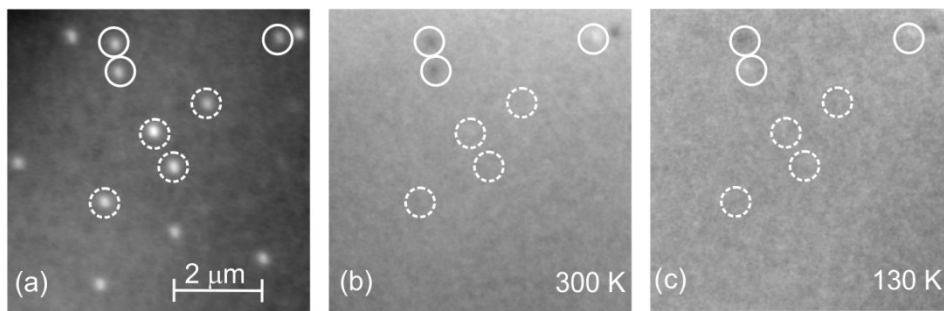

FIGURE 5.18. Cooling experiment. X-ray PEEM images : elemental (a) and corresponding magnetic contrast images (b) and (c) of Fe nanoparticles on Si substrate at RT and at 130K. Some FM (SPM) particles are highlighted by solid (dashed) circles. Adapted from [18].

To determine whether the ferromagnetic and superparamagnetic particles and the spontaneous transition from one state to the other reflects just a gradual change of the magnetic anisotropy, an estimate of the energy barriers of the superparamagnetic particles is required. To gain more insight into the MAE of the superparamagnetic particles, the sample temperature was gradually decreased in order to observe the transition from fluctuating superparamagnetic state to stable FM state. An elemental contrast image of the sample is shown in Fig. 5.18(a) with the corresponding XMCD contrast images Figs. 5.18(b) at RT and Fig. 5.18(c) at 130 K. The cooling is limited experimentally to a temperature of 130 K, at which temperature the particles are still in the SPM state. All initially superparamagnetic particles remain un-blocked within the time resolution of experiment. In this sense an upper limit of their mean energy barrier is estimated to be 0.35 eV, which is consistent with the

observed sigmoidal magnetization curves. Thus, the SPM particles possess a significantly smaller magnetic energy barrier E_m when compared to the FM particles.

Next, we correlate SPM and FM behavior with the particle size, which is known for each individual particle from atomic force microscopy. For this purpose magnetic contrast images such as Fig. 5.8(b) were analyzed and correlated with AFM image in the same sample location. Particles with asymmetries $|A| < 0.03$ are considered as SPM and particles with $|A| \geq 0.03$ as FM. The result is shown in Fig. 5.19, where the FM contribution to the total size distribution is given by the red bars. The data reveal that the particles can be ferromagnetic or superparamagnetic irrespective of their actual size in the present samples.
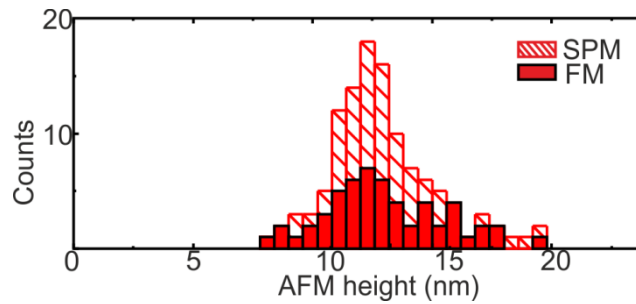

FIGURE 5.19 The same AFM height distribution of the Fe particles as shown in Fig. 5.7(a). The magnetic state of the particles is highlighted with red for ferromagnetic and shaded for superparamagnetic particles. Adapted from [18].

This finding is surprising, since the total magnetic anisotropy (and thus the magnetic energy barrier) of a particle is expected to scale with the particle size, and in a sample with a given size distribution the larger particles should be preferentially ferromagnetic while the smaller particles should be superparamagnetic. In contrast to this, the data suggests a size-independent mechanism which establishes the magnetic energy barriers in the FM nanoparticles. Clearly, in the size regime below 20nm there is no preferred size for the existence of FM particles. As will be discussed below, only iron particles with a diameter larger than about 27 nm are expected to possess a relaxation time longer than the experimental time resolution of 20 s. The latter condition is the minimum required for a particle to show magnetic contrast at room temperature when no external magnetic field is

applied in our experiments. Thus, the observation of ferromagnetism in much smaller particles hints to a significantly modified magnetic anisotropy energy landscape.

5.2.2. Magnetic anisotropy energy - Calculations

Systems of gas phase grown NPs deposited onto a substrate might be more complex than ideal free isolated clusters, due to the actual growth mechanism, the deposition process and interface energies between cluster and substrate. In addition to the magneto-crystalline, surface, and shape anisotropies, one has therefore to consider also the magneto-elastic contributions, dislocations or structural defects that could appear due to the growth [96] or the landing process [58] or contact forces due to interactions with the substrate [86] to obtain a realistic estimate of the total MAE.

In what follows, various calculations are quantitatively discussed in order to elucidate the origin of the FM state in the particles irrespective of their sizes and to determine the most relevant magnetic energy contributions that could explain the different MAEs observed in the Fe particles. Most of the calculations have been performed by Rocio Yanes Diaz and Uli Nowak from the Department of Physics, University of Konstanz [97].

5.2.2.1. Magnetocrystalline anisotropy

Iron possesses a bcc lattice with a cubic magnetocrystalline anisotropy, whose energy is given by Eq. 2.1 with MCA constants $K_1 = 4.8 \times 10^5 \, \text{erg/cm}^3 = 3.3 \mu\text{eV/atom}$ and $K_2 \approx 0$. Since $K_1 > 0$ and $K_2 \approx 0$, the MCA energy has minima ($E_{MCA} = 0$) at six orientations along <100>. It has maxima ($E_{MCA} = K_1 V / 3$) at eight orientations along <111> and saddle points at twelve azimuths <110> [See. Fig. 2.1(a)]. In order to switch from one easy axis to another, the magnetization has to traverse a path over an energy barrier which is the difference between the energy in the easy direction [100] and that in the saddle point direction [110].

The associated energy barrier is $E_{m,MCA} = K_1 V / 4$ and the contribution of K_2 to the energy barrier is negligible here.

To evaluate the role of the MCA contribution by means of the Arrhenius relation, the attempt frequency v_0 needs to be determined. As stated in Chapter 2, v_0 depends on the temperature, the NP's magnetic moment, and the nature of the MAE (cubic or uniaxial) as discussed in Refs. [52] and [50]. For $M_s(T)$ we consider the temperature dependent magnetization of bulk Fe and the damping constant $\alpha = 1.0$, i.e. the high damping limit. For spherical particles with a diameter of 20 nm which is the largest in our samples and a cubic MCA with bulk-like atomic density we obtain $v_0 = 6.32 \times 10^9$ s^{-1} at room temperature (See Appendix 1). Using the magnetocrystalline saddle point energy as the relevant energy barrier, the Arrhenius law gives $\tau = 7 \times 10^{-4}$ s at room temperature. This value indicates the SPM phase for particles with a diameter of 20 nm at room temperature. Since the MCA contribution scales with the particle volume, cf. Fig. 5.20, the MCA predicts SPM behavior for all particles under investigation, and therefore the experimentally observed FM state must correspond to properties which significantly deviate from the MCA of bulk iron. Finally, we can estimate the minimum magnetic energy barrier required to obtain FM behavior of Fe NP at room temperature. For cubic anisotropy we obtain 0.68 eV, while for uniaxial anisotropy we obtain 0.67 eV, since $v_0 = 2.07 \times 10^{10}$ s^{-1} for this case.
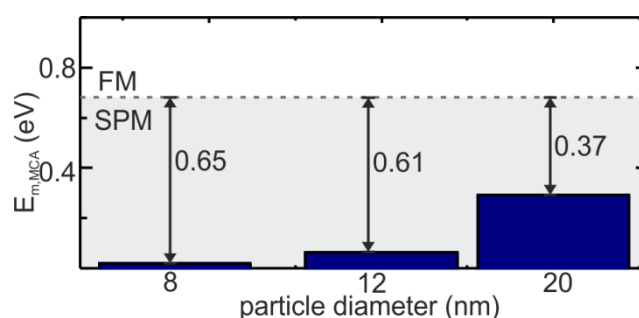

FIGURE 5.20. Magnetic energy barriers given by the magneto-crystalline anisotropy energy for bcc Fe particles as a function of the particle size. The dashed line represents the minimum magnetic energy barrier required by a 20 nm Fe NP to become FM at room temperature. Adapted from [62].

5.2.2.2. Surface anisotropy

The surface contribution to the effective magnetic anisotropy due to non-collinearities of the spins at the surface in case of perfect symmetric (Wullf construction) nanoparticles is modeled by a Néel surface anisotropy model [35]. This phenomenological model takes into account the different strengths of the magnetic anisotropy for surface atoms with differing local environments. In order to analyze the surface contribution to the total effective anisotropy, an atomic scale simulation was performed using a semi-classical localized spin model. The magnetic properties of the NP are described by an anisotropic Heisenberg Hamiltonian considering only nearest-neighbors (NN) exchange and anisotropy interactions. The anisotropic term of the Hamiltonian contains both core and surface anisotropy contributions. The core spins (spins with full coordination) present bulk-like magneto-crystalline anisotropy and for surface spins NSA was consider. This was done for a range of NP sizes, and a Lagrange multiplier method [33] was used to evaluate the effective energy landscape of the magnetic NP. This knowledge allows us to determine numerically the magnetic energy barrier of the system and its dependence on the local surface anisotropy constant K_S [38,98], which in this case is a variable parameter.
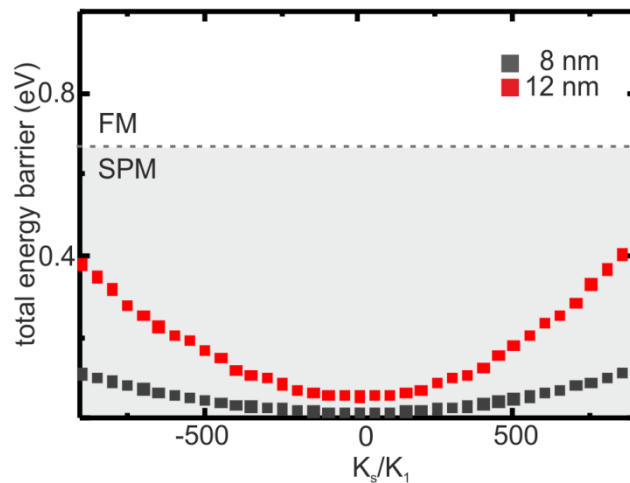

FIGURE 5.21. Total (MCA + surface anisotropy) energy barrier for a spherical Fe particle of 8, 12 nm in diameter as a function of the ratio (K_s/K_1) between the local surface anisotropy constant and the cubic anisotropy constant. The dashed line represents the minimum

magnetic energy barrier required by a 20 nm Fe NP to become FM at room temperature. Adapted from [62].

In the case of the bcc Fe particles it was observed that the surface anisotropy effectively acts as an additional cubic anisotropy with easy axes along the <100> directions. Therefore, the total magnetic anisotropy of the particle is increased with respect to the pure MCA case, see Fig. 5.21. For NP with a diameter of 8 (12) nm the total energy barrier $E_{m,MCA+surface}$ considering surface anisotropy is smaller than 0.13 (0.45) eV if $|K_S| \leq 900K_1$, i.e. in order to achieve a stable FM particle at room temperature, K_S has to be more than 900 times larger than K_1. This scenario is highly improbable, and we discard the surface anisotropy as an explanation for the FM behavior of the bcc Fe NPs at room temperature.

Diameter (nm)	8	12	20
Surface anisotropy energy barrier (eV)	0.03±0.01	0.06±0.02	0.18±0.06
Volume anisotropy energy barrier (eV)	0.01±0.01	0.04±0.04	0.2±0.2
Total magnetic energy barrier (eV)	0.04±0.02	0.1±0.06	0.38±0.26

TABLE 5.1. Surface (total) anisotropy energy barrier for 8, 12, 20 nm Fe particle.

Experimentally, an effective description of the magnetic anisotropy of the particle of the form $K_{eff} = K_v + \frac{6}{d}K_s$ is often considered, where K_v summarizes the volume contribution and K_s describes the surface contribution [83]. Note that this K_s parameter is the effective surface anisotropy constant and differs from the previous defined local surface anisotropy in the NSA model. The surface term scales inversely with the particle size d to account for the decreasing contribution of the surface to the particle properties with increasing particle size. The total anisotropy energy of the particle can be written as $E_{MAE} = K_{eff}V$. Using here the respective values determined experimentally by Bodker *et al.* [83] for Fe NPs, one can estimate the contribution of the effective surface anisotropy to the total anisotropy for

particles in the present size range cf. Table 5.1. It is obvious that the surface anisotropy gives a noticeable contribution (the surface anisotropy is three time larger than the volume contribution for 8 nm particles and almost equal with the volume contribution in case of 20 nm particles), but even the sum of surface and volume contributions is not sufficient to account for the observed FM states (for particles down to 8 nm) in the present study.

The values from Table 5.1 allow us to compare the surface anisotropy calculated with NSA model presented in Fig. 5.21 and estimate, in case of 12 nm particles, the surface anisotropy constant $K_s = \pm 400 K_1$.

5.2.2.3. Shape anisotropy

Considering that the landing process could create small deviations from the perfect spherical shape and induce different distortions in the particle, the shape anisotropy energy as a function of moment direction for different values of eccentricity were calculated, starting from a sphere which is distorted along one axis (prolate ellipsoid) and conserves its volume. This results in a uniaxial contribution to the effective anisotropy.

Although for the 20 nm diameter particles an aspect ratio of 1.02 could explain the observed magnetic stability, the smallest particles with a diameter of 8 nm would have to have aspect ratio larger than 1.8 [See Fig. 5.22(a)]. Since particles with such deformation level are excluded based on our structural characterization, one can conclude that the origin of the MAE for the entire size range is not shape-induced.

In addition, the minimization of free surface energy E_S favors a spherical shape instead of ellipsoidal. This can be seen in Fig. 5.22(b) which shows the increase in free surface energy as a function of c/a aspect ratio needed for an 8, 12 and 20 nm particle to show stable FM state, assuming the particle as a prolate ellipsoid with one semi-axis longer than the other two $a = b < c$. This is because the free surface energy can be relatively high [99] (the free surface density determined experimentally is about $2.4 J/m^2$ for bcc Fe). In Fig. 5.22(b) the difference of the surface free energy from an ellipsoid to a perfect sphere is plotted. To

overcome the SPM limit at RT by shape anisotropy, the particles will need an additional free surface energy of thousands of eV.
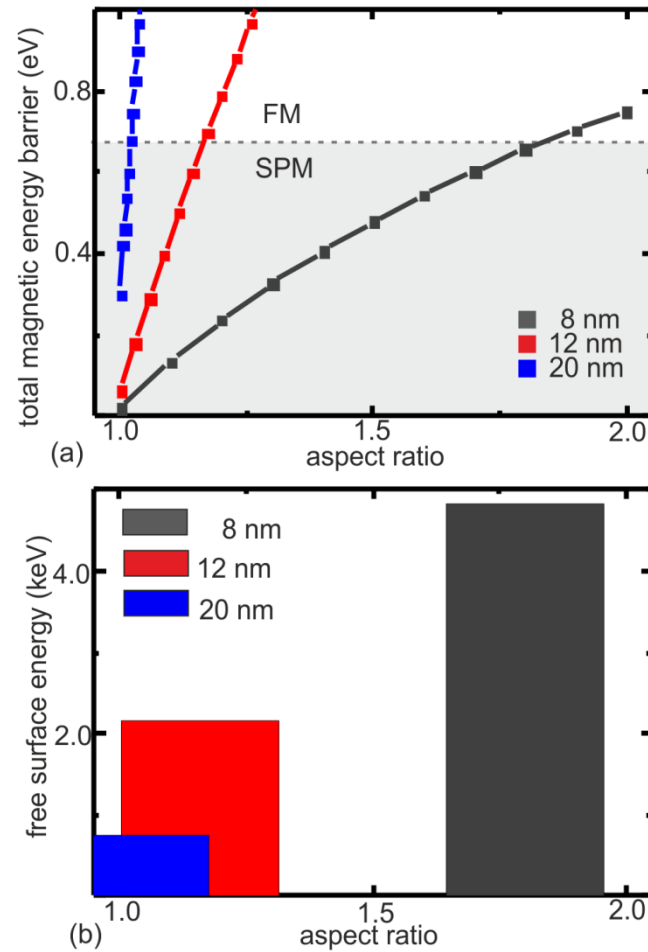

FIGURE 5.22. (a) Total (MCA + shape anisotropy) energy barrier for a prolate ellipsoid Fe particle of 8, 12, 20 nm in diameter as a function of the aspect ratio difference from a sphere. The dashed line represents the minimum magnetic energy barrier required by a 20 nm Fe NP to become FM at room temperature. (b) Difference in the free energy surface energy needed for a particle of 8, 12 and 20 nm to show FM behavior at RT due to shape anisotropy. Adapted from [62].

5.2.2.4. Strain effects

Using Eq. 2.2 for the magneto-elastic anisotropy, a strain of ~ 3% (0.9%)(see Table 5.2) would be required in the 8 (12) nm particles to obtain an energy barrier of 0.67 eV, which is the minimum needed to show magnetic stability at RT.

Diameter (nm)	8	12	20
The minimum energy barrier needed in addition to MCA to show FM behavior at RT (eV)	0.65	0.61	0.37
Strain (%)	3.20	0.90	0.12
Elastic energy (eV)	3143	839	69

TABLE 5.2. Strain required for a bcc Fe particle of 8, 12 and 20 nm to overcame at RT the minimum energy barrier to obtain FM behavior and corresponding elastic energy to maintain the strain.

The direct experimental access to such structural modifications in nanoparticles remains challenging. Only recently, techniques have been developed that enable the mapping of strain in supported single nanoparticles. These studies demonstrate that inhomogeneous strain may arise due to surface tension and defects at the particle-substrate interface [86]. Moreover, if dislocation structures within the particles were formed either during growth or upon the impact onto the substrate, such dislocations could also result in a uni-axial magnetic anisotropy [100].

However, a homogenous strain of this magnitude appears very unlikely to persist in NP of this size since the elastic energy E_E needed to maintain such a strain is of the order of 3000 (900) eV in case of 8 (12) nm particles [See Fig. 5.23]. This suggests that either the magneto-

elastic properties in NPs significantly differ from the bulk or the strain is strongly localized, e.g., via defects or dislocations.
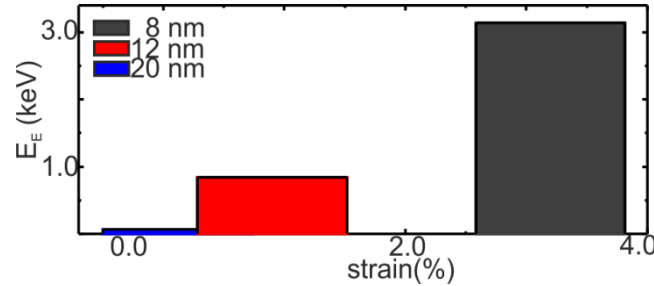

FIGURE 5.23. Elastic energy needed to maintain a strain to show stable FM state a RT in a Fe particle of 8, 12 and 20 nm diameter as a function of the strain. Adapted from [62].

5.2.2.5. Interface effects

The last contribution considered here is a possible reaction with the substrate. The deposition process depends on cluster size and material, as well as the substrate properties like surface energy, hardness, polarizability, and temperature [101]. Most of the studies available in the literature focus on the interface effects of Fe films on bare Si substrates and indicate that the interface effects will lead to an in- or out- of plane orientation of the magnetization of the metallic film depending on the thickness [102,103]. Our Fe NPs do not show any preferential orientation of their magnetization, so even if we assume that the particles interact with the substrate, the interface effects are too small to orient their magnetization. However, whether or not the interface acts as a source of the localized defects alluded to in the previous paragraph, remains an unanswered question.

Regarding the possibility of oxidation during the measurements, we note that the magnetic response of smaller particles should be more sensitive to oxidation, since the relative loss of magnetic volume would be much larger when compared to larger particles. However, we find no preferred loss of magnetic contrast nor a preferred tendency for the FM/SPM transition in smaller particles. As an example, NPs with a size of 11 nm show no indication for a loss of magnetic contrast over the measurement time [Fig. 5.12(c) and (d)]. These FM particles show no switching of the magnetization. In addition, the azimuthal scans of the particles Fig. 5.14,

72

which were recorded subsequent to the magnetization curve, show clear magnetic contrast and therefore confirm the stability of both the FM state and the magnetic contrast over a much longer period. In fact, oxidation experiments indicate that the FM state is stable upon O dosage, indicating that the origin of the large MCA contribution does not originate from the free surface of the nanoparticle [104].

5.3. Discussion and Conclusions

In summary, Fe particles in the size range from 8 to 20 nm deposited onto passivated Si(100) substrates were investigated by means of PEEM and XMCD. The experiments with single particle resolution revealed that iron nanoparticles can have substantially different magnetic properties compared with bulk iron. The distribution of magnetic asymmetries at room temperature revealed the co-existence of ferromagnetic NPs with significantly modified magnetic energy barriers and superparamagnetic NPs with more bulk-like properties at all sizes in the distribution. By increasing the measurement temperature, the blocking temperature of the ferromagnetic nanoparticles could be determined to give an estimate of the MCA of about 0.83 eV.

As shown in Fig. 5.20, to overcome the SPM limit and show FM contrast at room temperature, the particles need a magnetic energy barrier of about 0.67 eV, which is in all cases much larger than the bulk MCA. Adding surface anisotropy contributions cannot explain the observed FM states [Fig. 5.21]. For particles larger than 12 nm [cf. Fig. 5.22(a)] one finds that small deviations from the perfect spherical shape (elongated particles with aspect ratio around 1.2) could induce a stable FM state in our particles, ignoring the free surface energy needed to maintain such an elongated shape for the particles. However, since also the smaller particles, down to 8 nm, show stable FM behavior at room temperature and the corresponding values of the shape anisotropy would require unexpected aspect ratios (based on the structural characterization and selection of the particles), of about 1.8, it is concluded that the origin of increased MAE is not shape-induced. In addition, the calculations of the free surface energy support the idea that the observed increased MAE cannot be due to shape anisotropy. A strain of 0.9 % is enough to show FM behavior at RT in case of 12 nm Fe particles, but the increased MAE cannot be due to strain effects since the

elastic energies needed to maintain such strains are of order of hundreds of eV compared with 0.67 eV needed to show FM behavior at RT [cf. Fig. 5.22]. Finally, the random orientation of the easy axes of the present FM particles excludes significant contributions from interface anisotropy, since these effects would lead to a preferred in-plane (e.g. due to the slight flattening of the particles) or out-of-plane orientation of the magnetization.

Considering all anisotropic contributions one can conclude that the magnetic state of iron nanostructures is strongly correlated with their structure. The FM state of the NPs was found to be metastable [18] and can spontaneously relax to a state which exhibits the anticipated superparamagnetic behavior [cf. Figs. 5.12(e) and (f)]. This indicates that the present MAE could be governed by intrinsic properties such as structural defects due to the particle deposition process. The latter can, even under soft landing conditions, create dislocations in the nanoparticles [87]. This argument is supported by the observation of irreversible changes of the magnetic properties upon heating to higher temperatures (420 K cf. Fig. 5.17), which might be attributed to a thermal annealing of structural defects.

Chapter 6

Co and Ni particles on Si

Adapted from [62], this chapter presents a comparative study between different magnetic NPs deposited on the same type of substrate in order to determine whether the observed phenomena in Chapter 5 are restricted to that particular system, or whether it might be also observed in other nanoparticle/substrate systems. The ultimate goal is to clarify the origin of the high anisotropy state of Fe NPs presented in the previous chapter. The magnetic properties of Co and Ni NPs deposited under soft landing conditions onto passivated Si substrates are discussed in this chapter. Despite the fact they have the same atomic fcc structure, the nickel and the cobalt particles demonstrate different magnetic behavior: while the fcc Ni particles only exhibit the expected superparamagnetic behavior the fcc Co particles are ferromagnetically blocked or superparamagnetic at room temperature, irrespective of their size and the anticipated size-related scaling laws, similar with the Fe nanoparticles. The experimental findings are compared with the respective calculated magnetic anisotropy contributions of these two different types of deposited nanoparticles and confirm the assumption of the enhanced MAE due to structural defects generated in the particle deposition process.

6.1. Co NPs on Si substrate

Co NPs prepared and deposited onto passivated Si substrates under the same conditions as the Fe NPs described in previous chapter were investigated. While for gas phase prepared Fe particles in the present size range mostly cubic or spherical particles with bcc structure have been reported in the literature, the situation is more complex for Co and the nature of the particles depends critically on the cluster growth conditions, including the cluster source operation parameters and sample treatment upon deposition. This is due to a subtle balance of surface and chemical binding energies in determining the lowest energy structural configurations [96]. In Ref. [105] hcp (α-phase) Co has been found for particles larger then about 30 nm. Between 30 nm and 20 nm a mixture of hcp- and fcc (β)-phases is found, while below 20 nm only fcc particles are found. Notably, the fcc phase is not trivial (due to competition between hcp and fcc structures), but might be established by multiple twinned icosahedra, which are however metastable and can be transformed to single crystalline fcc particles by annealing to 300°C [37]. The different structural motifs are likely to show significantly different magnetic properties. For instance single crystalline hcp particles might have a strong uniaxial anisotropy due to the lower hexagonal symmetry. In contrast, the fcc particles will have a cubic MCA, which provides even smaller magnetic energy barriers when compared to soft-magnetic Fe. Finally, the multiple twinned structures may demonstrate a different behavior due to the presence of the internal interfaces. This inherent complexity is also reflected in the chemical synthesis, which allows a large variety of shapes and structures to be prepared, cf. e.g. [106], which might give rise to a rich variety of magnetic properties. Small Co particles have been found to show significantly enhanced magnetic anisotropy [10].

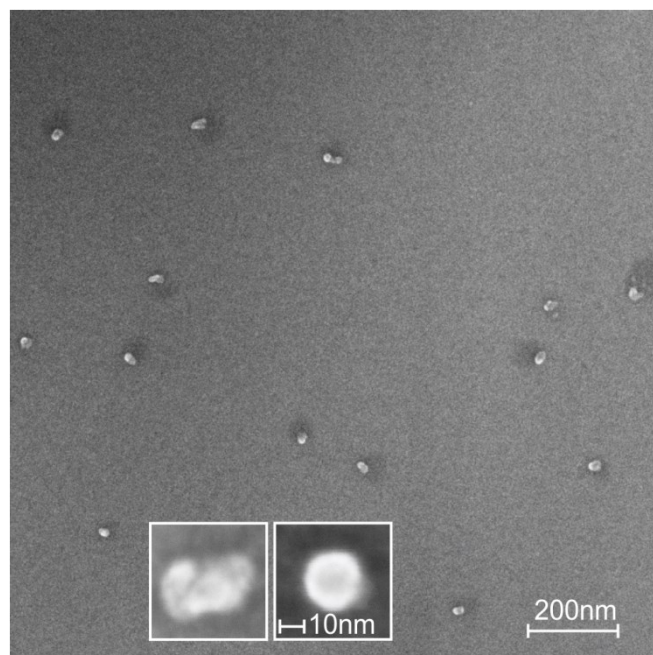## 6.1.1. Structural characterization

FIGURE 6.1. E*x situ* SEM image of Co NPs upon deposition onto passivated Si(100) wafers. Inset: High resolution SEM image of individual Co NPs (left: bad-shaped particles and right: typical well-shaped particle selected for further analysis). Adapted from [62].

Co NPs in the present size-range, prepared with the ACIS, possess bulk-like magnetic moments [107]. *In situ* structural characterization with scanning tunneling microscopy on supported Co NPs revealed indication for a faceted shape [108] in accordance with complementary *ex situ* TEM measurements, which further indicated single crystalline fcc particles [54]. *Ex situ* SEM of the present Co NPs on SiO_x reveals a significantly higher portion of imperfectly-shaped particles then that seen for Fe, as shown in Fig. 6.1. This might reflect a more complicated oxidation behavior compared to Fe. However, as in the case of Fe, only well shaped particles are selected for further analysis. The overview SEM image in Fig. 6.1 confirms a nearly random spatial distribution of the particles with a particle density of a few NPs per μm^2. AFM data taken from the well-shaped particles reveal, without correcting for the oxide shell that forms upon exposure to ambient air, a mean particle height of 14 nm (compared with 12 nm for Fe NPs, for the same parameters of the cluster source). This variation cannot be simply assigned to the different atomic density of Fe and Co, but could

reflect the different oxidation behavior. The full distribution of particle sizes ranges from 8 to 23 nm [Fig. 6.2].
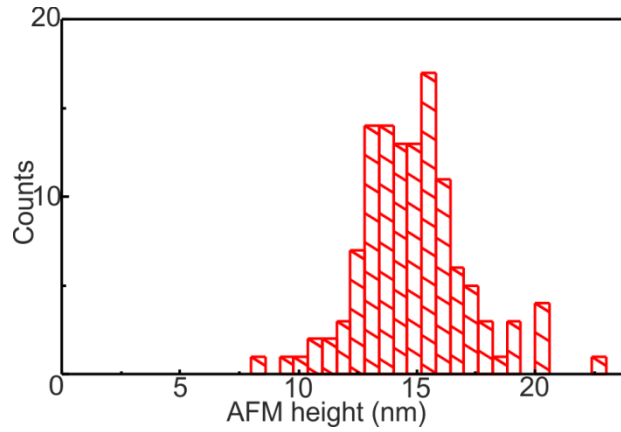

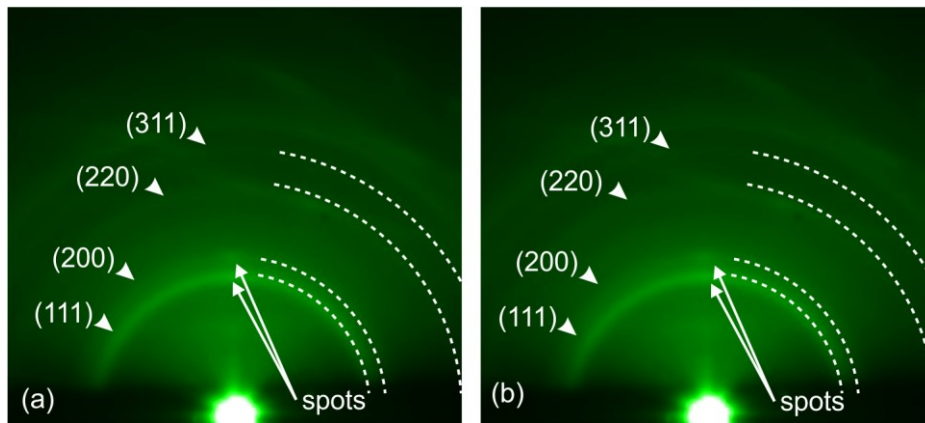FIGURE 6.2. AFM size distribution of the Co NPs. Adapted from [62].

FIGURE 6.3. (a) *In situ* RHEED diffraction patterns of supported Co NPs with a mean size of about 14 nm at room temperature as deposited and (b) at 500°C. Adapted from [62].

In situ reflection high energy electron diffraction (RHEED) investigations were done in order to reveal the crystallographic structure and orientation of the particles. The obtained RHEED measurements of the deposited Co NPs are shown in Fig. 6.3(a) and (b). The presence of Laue diffraction rings in the RHEED pattern indicates that the deposited Co NPs are randomly oriented on the Si substrate and have an fcc structure in agreement with previous

TEM characterization [54]. The texture visible in the (200) and the (111) rings indicates that the NPs are preferentially oriented with their {001} and {111} surface facets parallel to the surface. Similar to Fe, the diffraction rings for Co NPs remain stable in time and with increasing the temperature up to 500°C [cf. Fig. 6.3(a) and (b)].
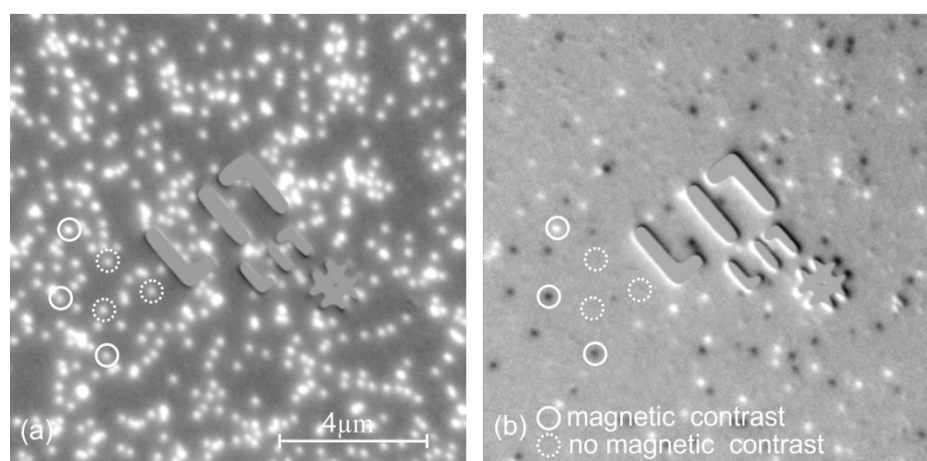
6.1.2. Magnetic properties

FIGURE 6.4. (a) X-ray PEEM elemental contrast image of Co NPs (white dots). (b) Corresponding XMCD contrast image. There are particles which demonstrate magnetic contrast (white circles) and particles which show no magnetic contrast (dashed circles). The images are recorded *in situ* at room temperature. Adapted from [62].

Elemental and magnetic contrast images of Co particles were obtained analogously to those of the Fe particles, and are shown in Fig. 6.4(a) and (b). The elemental image is obtained by dividing the image taken at L_3 Co edge of 778 eV with a pre-edge image at 770 eV. The XMCD image [Fig. 6.4(b)] recorded at the L_3 Co edge shows that some of the Co NPs show clear magnetic contrast ranging from white to black at RT.

The normalized XMCD values of the well-shaped selected NP are plotted in Fig. 6.5. The histogram of the normalized XMCD values of the individual NP reveals a peak at zero XMCD contrast (SPM particles) on top of a flat distribution of finite contrast values (FM particles) irrespective of the size of the particles [Fig. 6.6], similarly to the Fe case [Fig.

5.21]. In the following sections, the magnetic properties of Co particles will be discussed, in analogy to the Fe case in the previous chapter.
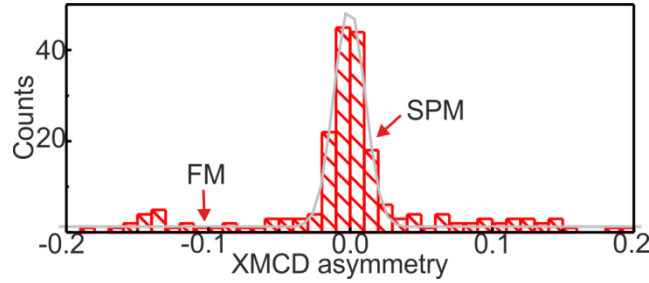

FIGURE 6.5. Distribution of normalized XMCD contrast values obtained from the data in Fig 6.4 (b). Adapted from [62].
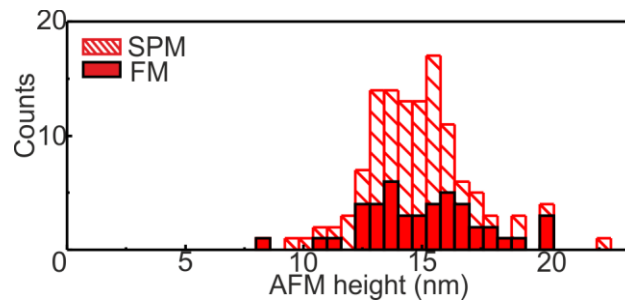

FIGURE 6.6. AFM height distribution of the Co particles. The magnetic state of the particles is highlighted with red for FM and shaded for SPM. Adapted from [62].

6.1.3. Calculations: different anisotropies contributions

6.1.3.1. Magnetocrystalline anisotropy

The RHEED measurements reveal that the Co particles crystallize in the fcc phase. Since for fcc Co $K_2 = -1.5 \times 10^5$ erg/cm^3 is a factor of 5 smaller than $K_1 = -7.4 \times 10^5$ erg/cm^3 = 3.8 μeV/atom, its contribution will be neglected in what follows and only the first term of the

anisotropy will be considered. In this case with $K_2 \cong 0$ and $K_1 < 0$, the maxima and minima are interchanged as compared to the case of Fe, the highest energy bulges are in directions perpendicular to the cubic faces (<100>) and the lowest energy dimples are along the body diagonals (<111>). The associated energy barrier to switch the magnetization between different minima directions (for example from one direction along the body diagonal to the opposite) is $E_{m,MCA} = E_{[111]} - E_{[110]} = \dfrac{K_1 V}{3} - \dfrac{K_1 V}{4} = \dfrac{K_1 V}{12}$ [52]. As mentioned above, the full distribution of Co particles heights [Fig. 6.2], measured *ex situ* by AFM, reaches from 8 to 23 nm with a broad peak around the mean value of 14 nm. The biggest particles consist of about 380,000 atoms with a total MAE of about $E_{MAE} = 1.44 \mathrm{eV}$ and an energy barrier of $E_{m,MCA} = E_{MAE}/12 = 0.12$ eV [See Fig. 6.7]. When compared to Fe NPs, the respective MCA energy barriers for Co NPs are significantly smaller. Thus, all Co particles are predicted to be SPM at room temperature, in contrast to the experimental observations. The energy barrier required to have ferromagnetic Co nanoparticles at RT is $E_m = 0.674$ eV, when using an attempt frequency $\nu_0 = 1.864 \times 10^9$ s^{-1} (See Appendix 1).
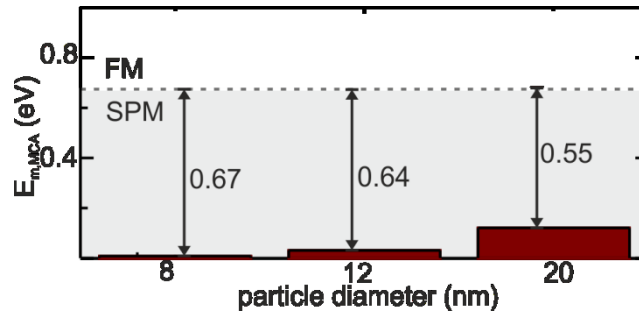

FIGURE 6.7. Magneto-crystalline anisotropy energy barriers for fcc Co particles as a function of the particle size, and difference in energy needed to stabilize FM particles at room temperature. Adapted from [62].

6.1.3.2. Surface anisotropy

The surface anisotropy in fcc Co particles with spherical shape induces an additional cubic anisotropy whose easy axes are along the cubic faces (<100>). This means that, opposite to what happens with bcc Fe NPs, the surface anisotropy in fcc Co particles competes with the core MCA. For small values of the local surface anisotropy, the effective anisotropy of the particle is reduced with respect to the bulk value. On the other hand, for high values of $|K_S| > 300K_1$ the surface contribution to the effective anisotropy is the dominant term, resulting in a re-orientation of magnetic easy axes of fcc Co nanoparticle and for $|K_S| > 400K_1$ leads to an increase of the effective anisotropy, see Fig. 6.8. As such large surface contributions are not physical, this increase cannot explain the thermal stability of the fcc Co nanoparticle at RT.
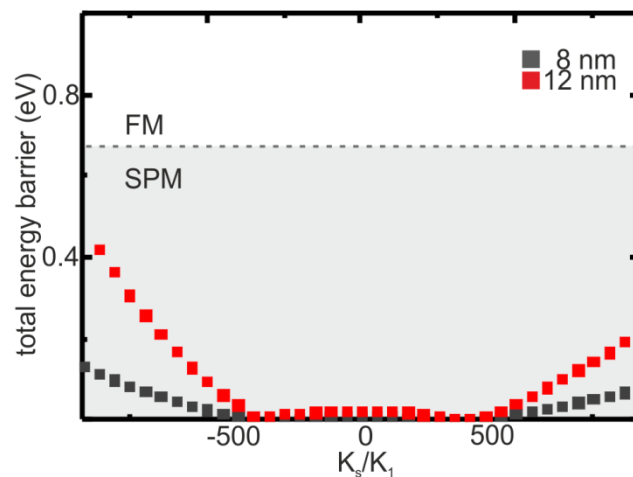

FIGURE 6.8. Total (MCA + surface anisotropy) energy barrier for a spherical Co particle of 8, 12 nm in diameter as a function of the ratio between the local surface anisotropy constant and the cubic anisotropy constant (K_S/K_1). Adapted from [62].

6.1.3.3. Shape anisotropy

Considering the same deformation factor [37] and the same volume of the particle as discussed in the previous chapter, the energy barrier given by shape anisotropy differs from one element to another by the square of the saturation magnetization. Thus, Co particles with the same shape have an energy barrier smaller by a factor of 1.65 when compared to Fe particles. Therefore, shape-induced enhanced energy barriers in Co NPs are even less likely to be responsible for the observed FM states. Nevertheless, assuming the particle is distorted along one direction and conserves its volume, we calculate the shape anisotropy energy as a function of moment direction for different values of eccentricity. Even in the most favorable configuration, for a maximum energy barrier to overcome the superparamagnetic limit at RT by shape deformation, the smallest Co particle of 8 nm diameter needs an aspect ratio of 2.6 [cf. Fig. 6.9]. As with Fe NPs, the shape anisotropy cannot explain the observed MAE in Co particles.
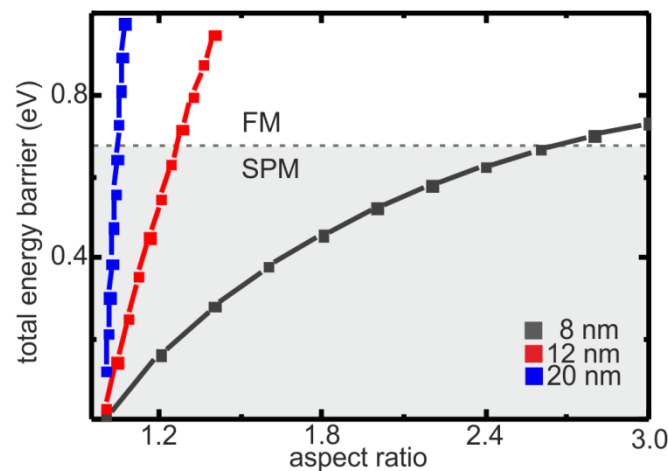

FIGURE 6.9. Total (shape +MCA) anisotropy energy barrier for a prolate ellipsoid Co particle of 8, 12, 20 nm in diameter as a function of the aspect ratio difference from a sphere. Adapted from [62].

6.1.3.4. Strain effects

An analogous treatment of the Co particles reveals that to obtain an energy barrier of about 0.67 eV a strain of ~ 1.3 % is sufficient. However, the elastic energy needed to induce such a strain is still of the order of a few hundreds of eV [cf. Fig. 6.10] and thus unlikely. Therefore, for the Co particles as well, homogenous strain is unlikely to be the cause of the increased magnetic energy barriers.
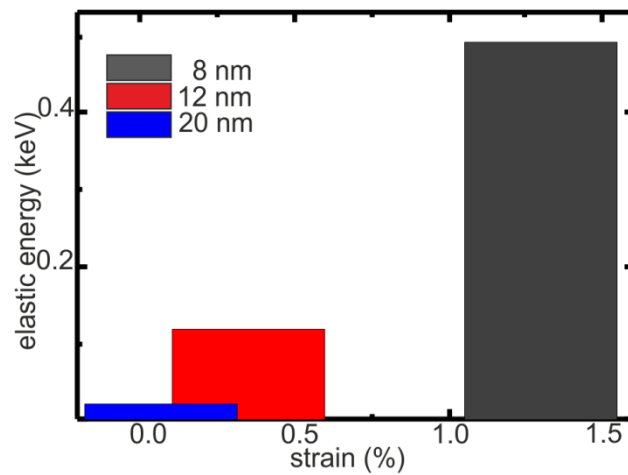

FIGURE 6.10. Elastic energy needed to induce a strain sufficient to show stable FM state at room temperature in a Co particle of 8, 12 and 20 nm diameter as a function of the strain strength. Adapted from [62].

6.1.4. Conclusion

Investigating, by means of PEEM and XMCD, Co particles in the size range from 8 to 23 nm deposited on passivated Si(100) substrates, it was found that fcc Co nanoparticles can have substantially different magnetic properties compared with bulk Co. The distribution of magnetic asymmetries at room temperature revealed the co-existence of ferromagnetic NPs with significantly modified magnetic energy barriers and superparamagnetic NPs with more bulk-like properties at all sizes in the distribution.

To overcome the SPM limit and show FM contrast at room temperature, the particles need a magnetic energy barrier of about 0.67 eV, which is in all cases much larger than the bulk MCA as is indicated in Fig. 6.7. The surface anisotropy contributions, inducing an additional cubic anisotropy whose easy axes are along the cubic faces (<100>), competes with the core MCA, for small values of the local surface anisotropy, or in the case of bigger values reorients the magnetic easy axis and cannot explain either the observed FM states (Fig. 6.8.). Regarding shape induced anisotropy, in case of fcc Co, even in the most favorable configuration, for a maximum energy barrier to overcome the superparamagnetic limit at RT by shape deformation, the smallest Co particle of 8 nm diameter needs an aspect ratio of 2.6 [cf. Fig. 6.9]. Since these deformations are excluded from our analysis, the shape anisotropy cannot explain the observed MAE in Co particles. In addition, the calculations of the free surface energy support the idea that the observed increased MAE cannot be due to shape anisotropy. A strain of 0.4 % is sufficient to show FM behavior at RT in case of 12 nm Co particles, but the increased MAE cannot be due to strain effects since the elastic energies needed to maintain such strains are of order of 100 eV (Fig. 6.10). Considering all the anisotropic contributions one can conclude that the magnetic state of Co nanostructures, similar with the case of Fe, is strongly correlated with their structure.

In conclusion, it is found experimentally that fcc Co NPs show a coexistence of FM and SPM particles irrespective of the sizes of the particles, similarly to bcc Fe particles when deposited on the passivated Si surfaces. Evaluating the most relevant contributions to the MAE, the presence of the FM state with such a high MAE is also not explained by the properties known from bulk fcc Co. Being not related with size nor with any magnetic anisotropy contributions, the remaining possibilities might again be associated with localized defects in the particles.

6.2. Ni NPs on Si substrate

As a third system, Ni NPs deposited onto the same Si substrates were investigated. The properties of Ni NPs were compared to that of Fe and Co.

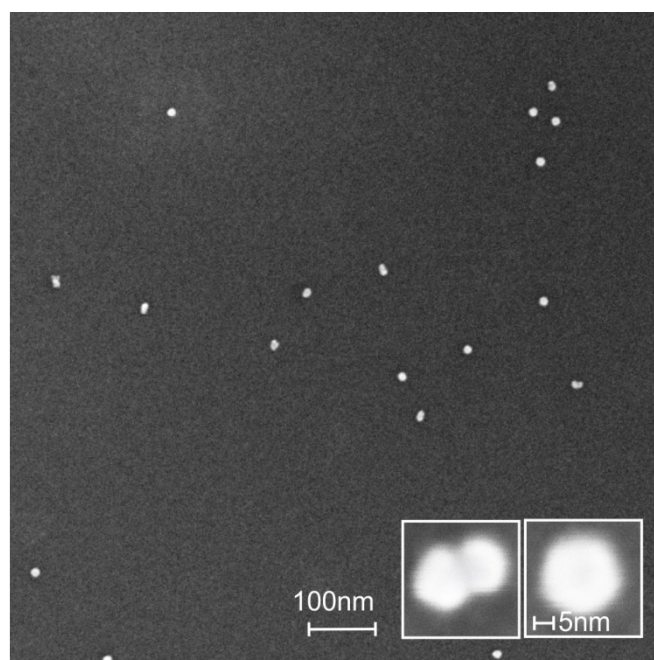### 6.2.1. Structural characterization of Ni particles

FIGURE 6.11. E*x situ* SEM image of Ni NPs upon deposition onto passivated Si(100) wafers. Inset: High resolution SEM image of an individual Ni nanoparticle (left: non-ideal-shaped particles and right: typical well-shaped particle selected for further analysis). Adapted from [62].

High resolution SEM images on individual particles reveal a high fraction of well-shaped Ni particles [cf. the inset on the right hand of Fig. 6.11], which resembles more closely the case of Fe than that of Co. The AFM size distribution of Ni particles is shown in Fig. 6.12. The height of the particles varies from 6 to 18 nm, with a mean value around 10 nm.
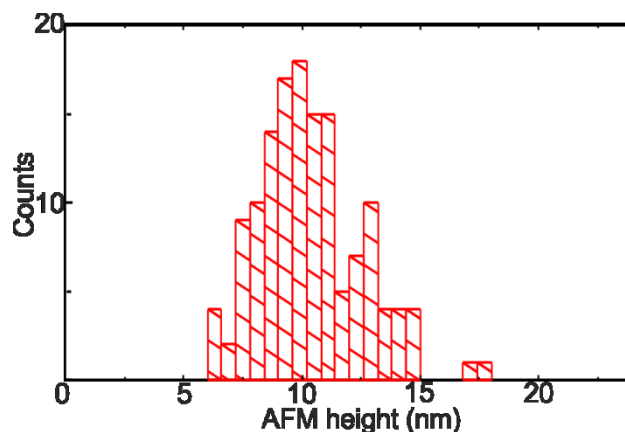
FIGURE 6.12. AFM height distribution of Ni NPs. Adapted from [62].

The *in situ* RHEED measurements reveal that the Ni particles crystallize in the bulk fcc structure [Fig. 6.13]. As for the Fe and Co cases, the Ni NPs have a random orientation on the Si substrate and again the different Laue diffraction rings remain stable in time and with increasing the temperature to more than 500°C [cf. Fig. 6.13(b)]. Similarly to the Co particles, the RHEED patterns of Ni NPs deposited on SiO_x present a texture in the (200) and the (111) rings indicating that the NPs prefer to rest with their {001} and {111} surface facets parallel to the surface.
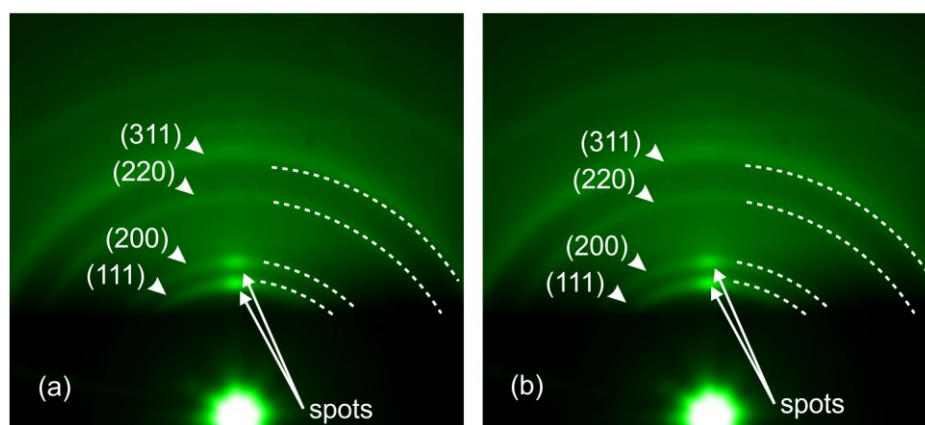

FIGURE 6.13. *In situ* RHEED diffraction patterns of supported Ni NPs with a mean size of about 10 nm at room temperature as deposited and (d) at 500°C. Adapted from [62].
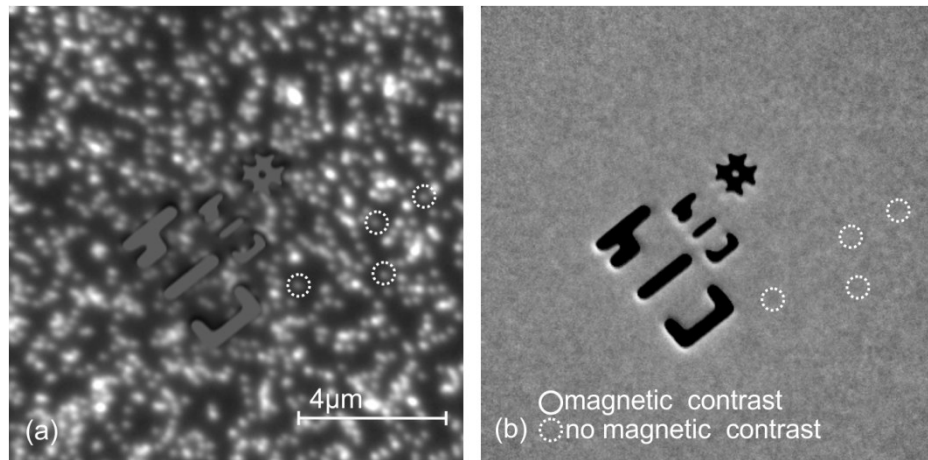
6.2.2. Magnetic properties

FIGURE 6.14. (a) X-ray PEEM elemental contrast image of Ni NPs (white dots). (b) Corresponding XMCD contrast image. The particles show no magnetic contrast (dashed circles). The images are recorded *in situ* at room temperature. Adapted from [62].
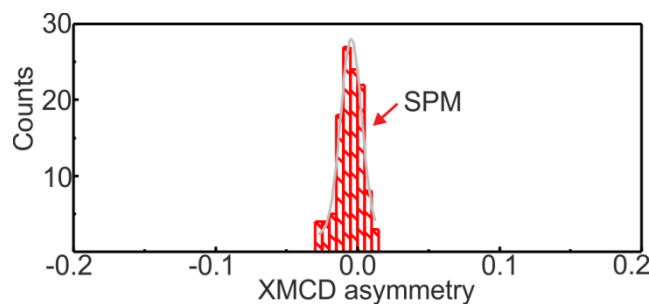
FIGURE 6.15. Distribution of normalized XMCD contrast values obtained from the data in (b) indicating that all Ni NPs are SPM. Adapted from [62].

X-ray PEEM data of the Ni NPs are shown in Fig. 6.14(a) and (b). The XMCD image Fig. 6.14 (b) reveals no FM states in this system: the particles show no magnetic contrast at room temperature. By evaluating the normalized XMCD contrast of the particles, a histogram [Fig. 6.15] is obtained which presents only a peak at zero XMCD contrast associated to the SPM character of the particles, as expected when considering Ni bulk values of the anisotropy contributions (see below) but in clear contrast to the behavior of the Fe and Co NPs. Thus for the Ni NPs, only the as-expected SPM behavior is observed for all sizes from 6 to 20 nm [See

88

Fig. 6.16]. Even though the FM state is absent, a thorough discussion of the anisotropy contributions for comparison with the cases of Fe and Co above is given next.
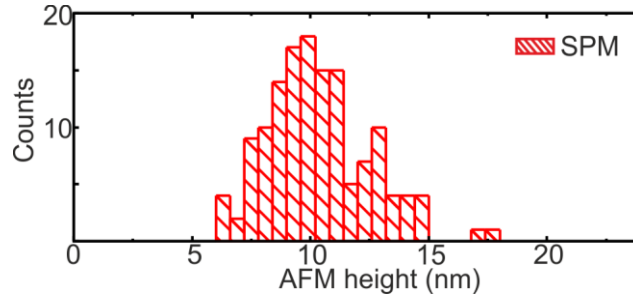

FIGURE 6.16. AFM height distribution of the SPM Ni particles. All particles are SPM (shaded) irrespective of their size. Adapted from [62].

6.2.3. Calculations of different anisotropies contributions

6.2.3.1. Magnetocrystalline anisotropy

Since for the case of fcc Ni, both anisotropy constants K_1 and K_2 are negative, with $K_1 < 0$ and $K_2 \in (+\infty, -\dfrac{9K_1}{4})$, the easy axes are orientated along the <111> directions (body diagonal - minimum energy), with hard axes (directions of greatest energy) along the <100> directions and intermediate axes (saddle points) in the energy along the <110> directions. In order to switch the magnetization from one easy axis to another due to MCA energy, the NP's magnetic moment has to overcome an energy barrier which is the difference between the energy in the easy direction ($E_{[111]} = \dfrac{K_1 V}{3} + \dfrac{K_2 V}{27}$) and that in the intermediate direction ($E_{[110]} = \dfrac{K_1 V}{4}$). As shown in Fig. 6.17 the resulting magnetic energy barriers are one order of magnitude smaller when compared to the fcc Co particles.
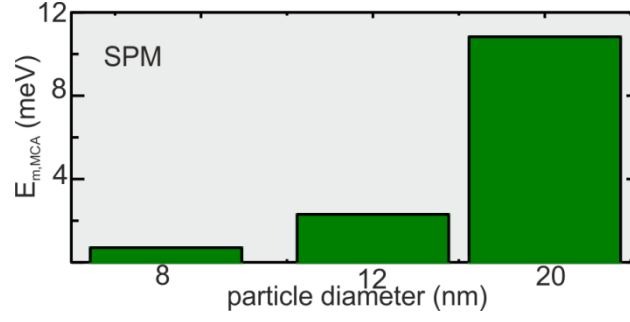
FIGURE 6.17. Magneto-crystalline anisotropy energy barrier for fcc Ni particles as a function of the particle size. Adapted from [62].

The magneto-crystalline anisotropy of $K_1 = -5.7 \times 10^4$ erg/cm^3 = -0.28 µeV/atom and $K_2 = -2.3 \times 10^4$ erg/cm^3 = -0.12 µeV/atom for fcc Ni will give an energy barrier of $E_{m,MCA} = 0.01$ eV for a particle of 20 nm [See Fig. 6.17]. This value is considerably smaller than the minimum energy needed to have FM Ni particles at RT, $E_m = 0.71$ eV, considering an attempt frequency $\nu_0 = 4.59 \cdot 10^8$ s^{-1} (See Appendix 1).

6.2.3.2. Surface anisotropy

The contribution of the surface anisotropy to the total magnetic anisotropy in fcc Ni particles was numerically evaluated following the same strategy as in the bcc Fe and fcc Co cases. Similarly to the fcc Co case, it was observed that the additional cubic anisotropy induced by the surface anisotropy compete with the Ni magneto-crystalline anisotropy. For simulations K_S is used as a variable parameter ranging from $-800K_1$ to $800K_1$, which were considered as extreme cases. For the whole range of K_S studied here, the effective magnetic anisotropy is reduced with respect to the pure MCA value, see Fig. 6.18.

FIGURE 6.18. Total (MCA + surface anisotropy) energy barrier for a spherical Ni particle of 8, 12 nm in diameter as a function of the ratio (K_s/K_1) between the local surface anisotropy constant and the cubic anisotropy constant. Adapted from [62].
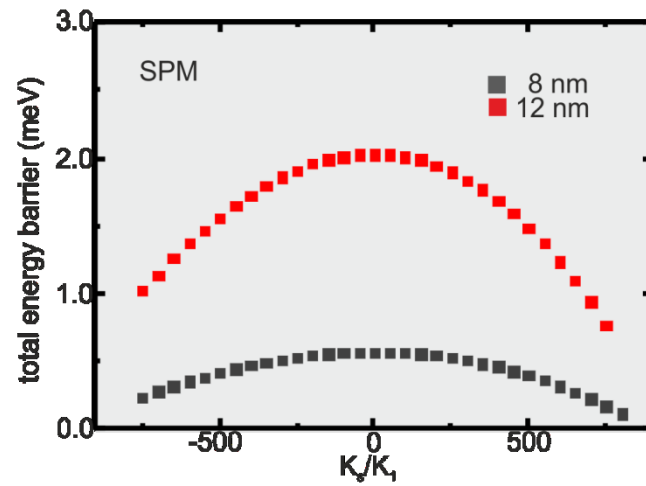
6.2.3.3. Shape anisotropy
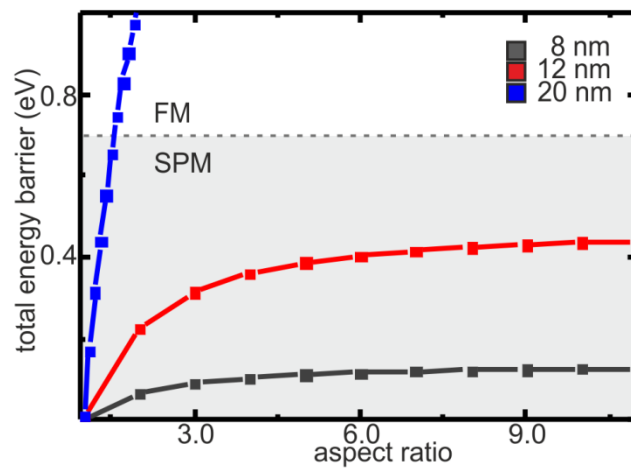
FIGURE 6.19. Total (MCA + shape anisotropy) energy barrier for a prolate ellipsoid Ni particle of 8, 12, 20 nm in diameter as a function of the aspect ratio difference from a sphere. Adapted from [62].

The shape anisotropy is proportional with the square of saturation magnetization, which is three times smaller in case of Ni compared with Co and Fe, so having stable FM Ni particles due to shape anisotropy would need even bigger elongations than for Fe and Co [cf. Fig. 6.19]. In particular, for Ni particles with diameter < 12 nm, not even an aspect ratio of 10 would be sufficient to overcome the fluctuating SPM limit.

6.2.3.4. Strain effects

In order to obtain an energy barrier of about 0.67 eV a strain of ~ 1.2 % would be sufficient to obtain a FM state for the smallest Ni particles at room temperature, and the elastic energy needed to induce such a strain is of order of hundreds of eV [cf. Fig. 6.20], similarly to the Co case.
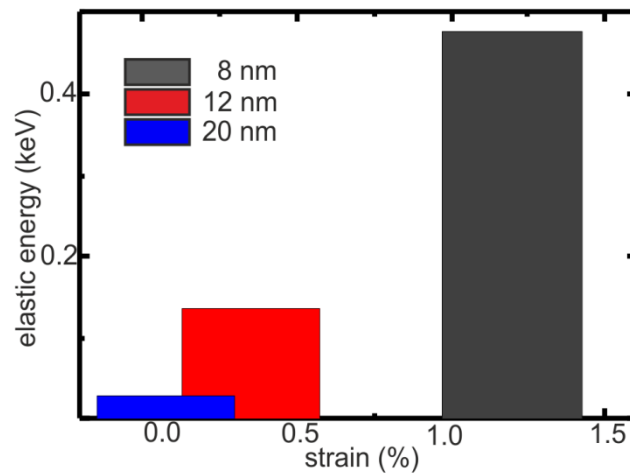
FIGURE 6.20. Elastic energy needed to maintain a strain to show stable FM state at room temperature in a Ni particle of 8, 12 and 20 nm diameter as a function of the strain strength. Adapted from [62].

6.2.4. Conclusion

Fcc Ni NPs in the size range from 8 to 20 nm deposited on passivated Si(100) substrates were investigated by means of PEEM and XMCD effect at RT. It was found that Ni particles are SPM at RT as expected from bulk fcc Ni anisotropy.

To overcome the SPM limit and show FM contrast at room temperature, the particles need a magnetic energy barrier of 0.7 eV, which is almost hundred times larger than the bulk MCA as is indicated in Fig. 6.17. Considering all the anisotropic contributions one can conclude that fcc Ni particles need much larger anisotropy contributions to overcome the SPM limit.

Chapter 7

Fe NPs on different substrates

In this chapter the results of a preliminary study of the magnetic properties of Fe nanoparticles deposited under the same conditions onto different crystalline substrates are presented. Fe particles deposited on W(110) show SPM behavior, as expected from theory, in contrast to Fe NPs deposited on Si(001), which show a coexistence of SPM and FM particles. We also attempted to study the properties of Fe NPs deposited on an antiferromagnetic NiO(001) surface; however, due to charging of the NiO surface, the magnetic state could not be resolved. For the case of Fe NPs deposited on Cu(001), we find that the particles diffuse into the Cu crystal. In conclusion, the interface effects could affect the magnetic properties of the particles.

In the previous experiments we have observed that supported 3d magnetic NPs with sizes from 8 to 20 nm, exhibit enhanced magnetic moments irrespective of their sizes [62]. Taking into consideration the different anisotropic contributions, the origin of the reported high anisotropy state was associated with a meta-stable structural state due to the presence of local defects within the NPs which can be associated with the NP-substrate interface, which is strong enough to cause ferromagnetic states in case of iron and cobalt nanoparticles, but not

in the case of nickel. To verify if the behavior and the properties of the supported nanoparticles depend on the interface between nanoparticle and substrate surface, Fe nanoparticles were deposited under the same conditions onto different substrates [Fig. 7.1].
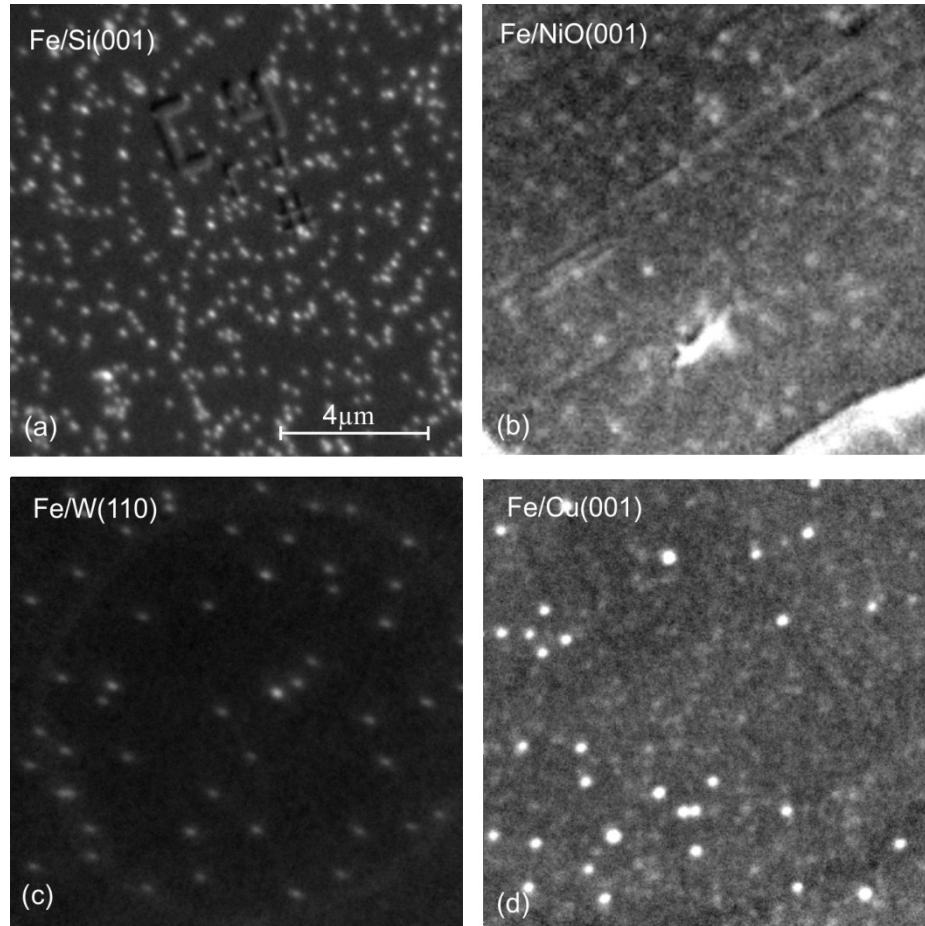
FIGURE 7.1. X-ray PEEM elemental contrast images of Fe NPs (white dots) randomly deposited on (a) Si(001), (b) NiO(001), (c) W(110) and (d) Cu(001) substrates.

7.1. Fe NPs on W(110)

In what regards Fe nanoparticles deposited at RT onto a W(110) substrate, it was reported that the particles are randomly orientated with a preferred tendency to rest on the surface with the {001} and {110} facets [109]. The orientation yield important implications when analyzing the magnetic properties of the particles. Even though in general a random

orientation of the particles should result in isotropic magnetic properties, a preferred in-plane magnetization of such a deposit was reported [64]. The measurements were an average over a large ensemble of nanoparticles. The preferred in-plane orientation was ascribed to a slight flattening of the particles upon deposition and the resulting combination of shape and interface anisotropy contributions.
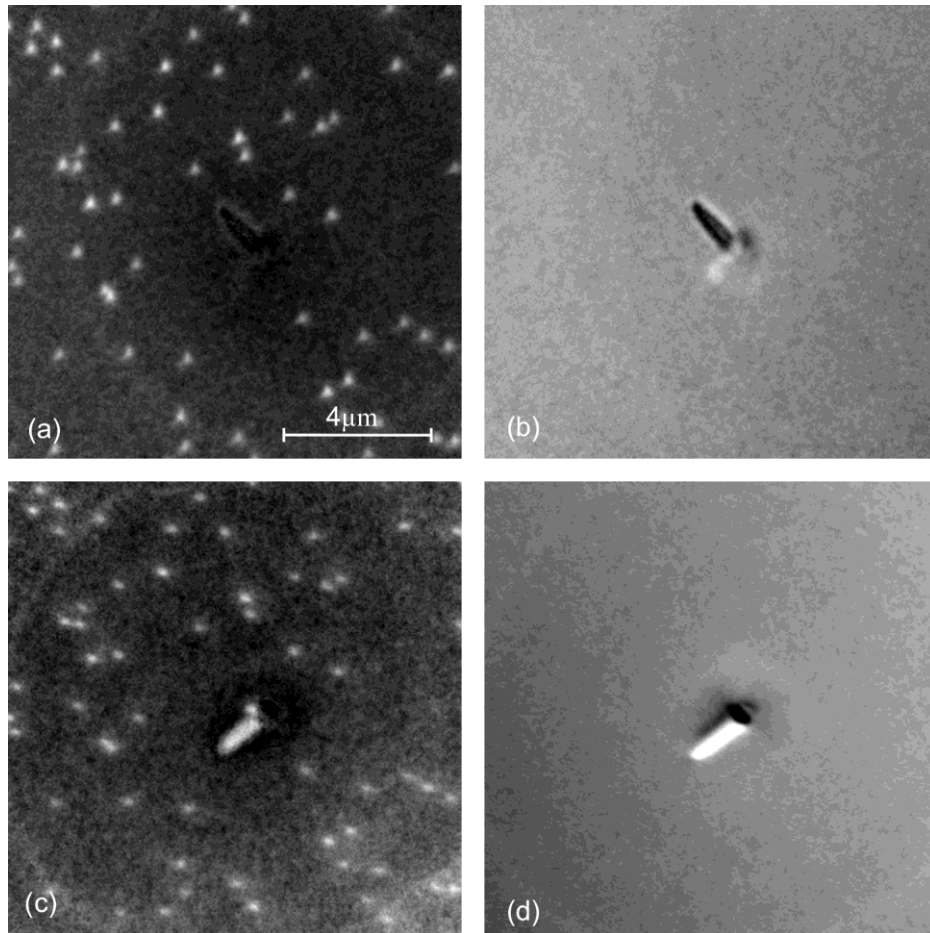
FIGURE 7.2. (a), (c) X-ray PEEM elemental contrast images of Fe NPs (white dots) randomly deposited on a W(110) substrate obtained with the x-rays incident along (a) the W[1$\bar{1}$0] and (c) the W[001] direction. (b) , (d) Corresponding XMCD contrast image. All the particles reveal no magnetic contrast. The images are recorded *in situ* at room temperature.

Fe NPs deposited on W(110) show clear visible elemental contrast in the PEEM, as one can observe in Fig. 7.2 (a), (c) for two perpendicular directions of the sample corresponding to W[1$\bar{1}$0] and W[001], but without magnetic contrast [Fig. 7.2 (b), (d)]. No dichroism was observed for any of the two perpendicular directions. The marker in the center allows us to

96

identify the same particles in different images taken with different microscopes and in this way to correlate the magnetic properties with their shapes. In SEM the particles look very similar with the particles deposited on Si(001), having the same percentage of well-shaped and badly shaped particles, with most of the particles being highly symmetric and compact [Fig. 7.3(a)-(c)]. The agglomerated particles appear just slightly elongated [Fig. 7.3(d)-(f)] compared with well-shaped ones. These particles show no dichroism either.
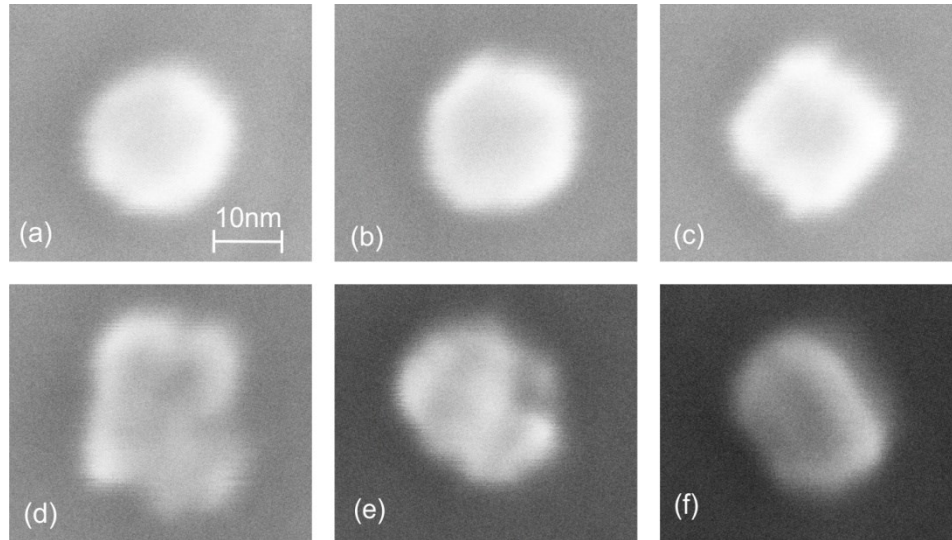
FIGURE 7.3. High resolution SEM images of individual Fe NPs deposited on W(110). (a)-(c) typical well-shaped particles. (d)-(f) non-ideal-shaped particles.

In conclusion, Fe NPs on W(110) show no dichroism, so they are SPM as expected from theory, which allow us to conclude that the magnetic blocked states of Fe particles are specific to Fe NPs on Si(001). In addition, we can exclude that the particles have a wide distribution of shapes, which could lead to ferromagnetism.

7.2. Fe NPs on NiO(001)

We attempted to study single Fe nanoparticles coupled to antiferromagnetic NiO(001) surfaces, namely, a NiO single crystal and 25 nm-thick NiO films deposited onto (001) Nb:SrTiO3. For the NiO thin films, no antiferromagnetic (AFM) domains were visible in PEEM. For the NiO single crystal, AFM domains were imaged [Fig. 7.4(a)]. We were able to

reduce the charging effects in the NiO substrate but they still strongly affected the measured signal of the deposited particles [see Fig. 7.4(b)], to the extent that the isotropic x-ray absorption at the Fe L_3 edge was reduced by a factor of about 10 compared to particles deposited on our standard Si substrates. Such a low signal-to-noise ratio precluded the detection of XMCD magnetic contrast of individual Fe nanoparticles [Fig. 7.4(c)].
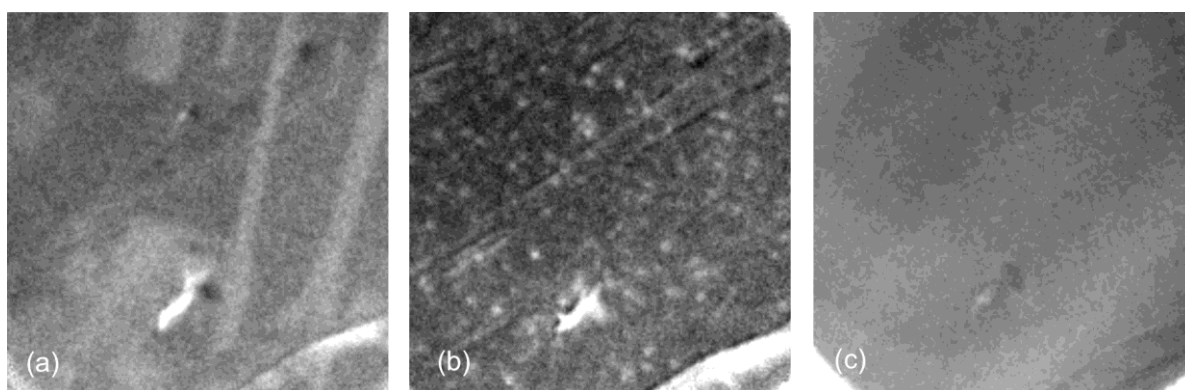
FIGURE 7.4. (a) X-ray magnetic linear dichroism (XMLD) image of NiO domains. This image is recorded at the Ni L_3 edge. (b) X-ray PEEM elemental contrast images of Fe NPs (white dots) randomly deposited on a NiO(001) crystal. (c) Corresponding XMCD contrast image.

7.2. Fe NPs on Cu(001)

We tried as well to image using PEEM Fe NPs with slightly smaller sizes deposited on Cu(001) substrates. In the elemental image two types of contrast was observed: bigger spots with clear visibile elemental contrast and smaller dots, apparently corresponding to particles burried under the Cu(001) surface [Fig. 7.5(a)]. Since this sample has no marker which allows us to identify the same particle in different microscopes, it remains unclear if the bigger spots are agglomerates of particles and the smaller dots are particles which are burried into the surface. The magnetic contrast is shown in Fig. 7.5(b). Very few particles exhibit magnetic contrast.
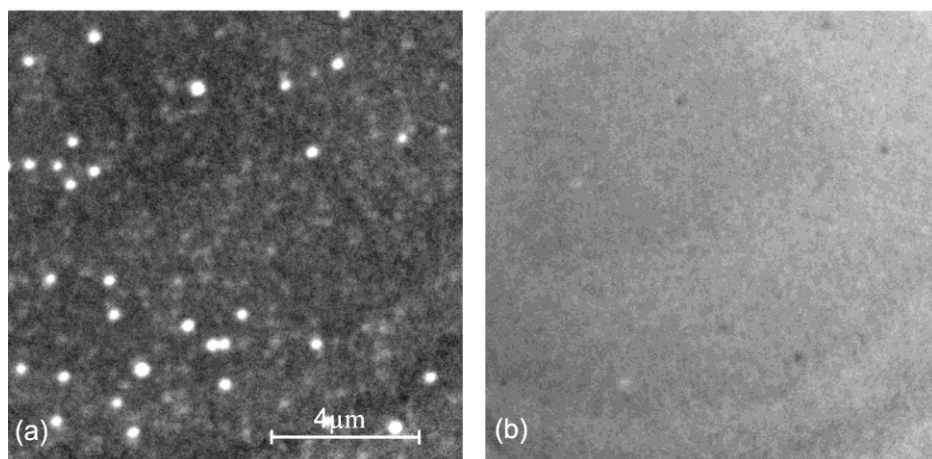
FIGURE 7.5. (a) X-ray PEEM elemental contrast image of Fe NPs randomly deposited on a Cu(001) substrate. (b) Corresponding XMCD contrast image. The images are recorded *in situ* at room temperature.

Chapter 8

Discussion and conclusion

Nanoscale ferromagnetic materials have attracted much interest for industry [1-3] and fundamental research [4,5] due to their unexpected magnetic properties when compared with bulk materials such as enhanced magnetic moments and magnetic anisotropies [8,9]. The experiments and calculations performed in this thesis aimed at understanding the fundamental physical laws governing the unusual magnetic behavior found in nanoparticle systems and elucidate the controversies found in the literature, by directly observing the behavior at the level of individual nanoparticles. The aim was to find if the magnetic properties scale with particle size at nanoscale or if there is a breakdown of the usual scaling laws linking magnetic properties to size at the nanoscale that is material dependent. This is made possible by advanced X-ray micro-spectroscopy techniques that allow the direct measurement of the magnetic and electronic properties of materials down to the nanoscale.

In this work, Fe, Co and Ni particles in the size range from 8 to 20 nm deposited on passivated Si(100) substrates were investigated. Using x-ray PEEM combined with XMCD we found that bcc Fe and fcc Co particles exhibit a similar behavior, showing a surprising coexistence of particles in ferromagnetic and superparamagnetic states at room temperature, irrespective of their size, while fcc Ni particles are superparamagnetic at all sizes. While the behavior of the Ni nanoparticles is as expected based on the bulk anisotropy values, the

presence of magnetically blocked Fe and Co nanoparticles is entirely unexpected. Fe and Co particles are FM and SPM for the same size of the particles disobeying the usual scaling laws. The FM state of Fe and Co particles at room temperature indicates significantly modified local properties when compared to the bulk counterparts. As shown in Fig. 8.1, to overcome the SPM limit and show FM contrast at room temperature, the particles need a magnetic energy barrier of about 0.7 eV, which is in all cases much larger than the expected MCA when considering the known bulk properties.
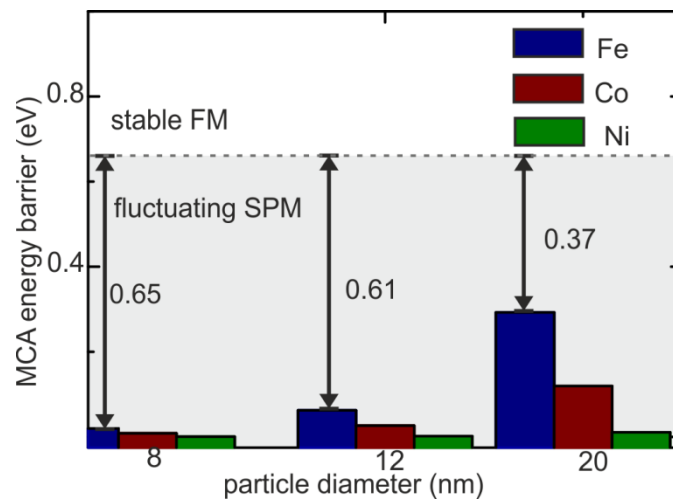
FIGURE 8.1. Magneto-crystalline anisotropy energy barrier at room temperature as a function of particle diameter in case of bcc Fe, fcc Co and fcc Ni NPs. Adapted from [62].

We have considered the possible origin for this enhanced magnetic anisotropy. We find that surface anisotropy contributions (Fig. 8.2) cannot explain the observed FM states. For 12 nm particles not even for a surface anisotropy 900 times larger than K_1, the cubic anisotropic constant for bulk, the surface contribution is enough to induce FM behavior at RT, for both Fe and Co.

For particles larger than 12 nm (cf. Fig. 8.3) one finds that small deviations from the perfect spherical shape (elongated particles with aspect ratio around 1.2 in case of Fe and Co) could induce a stable FM state in our particles, ignoring the free surface energy needed to maintain such an elongated shape for the particles. However, since also the smaller particles, down to 8 nm, show stable FM behavior at room temperature and the corresponding values of the shape

anisotropy would require unexpected aspect ratios (based on our structural characterization) of about 1.8 for Fe particles and 2.6 in case of Co particles, we conclude that the origin of increased MAE is not shape-induced.
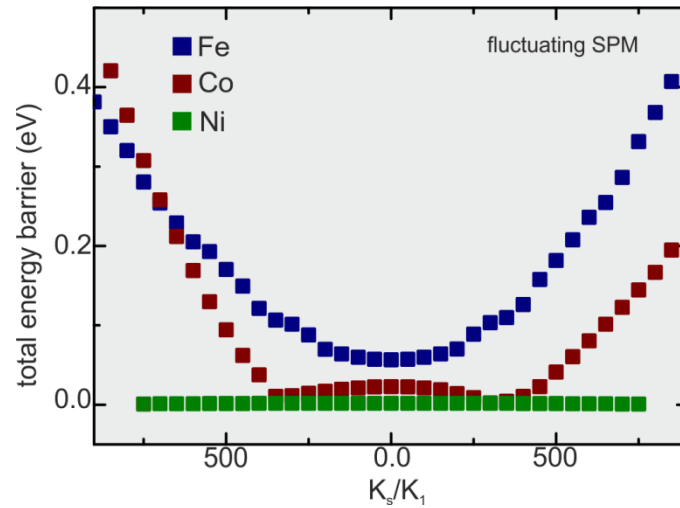
FIGURE 8.2. Total (MCA + surface anisotropy) energy barrier for a 12 nm spherical bcc Fe, fcc Co and fcc Ni particle as a function of the ratio (K_s/K_1) between the local surface anisotropy constant and the cubic anisotropy constant. Adapted from [62].

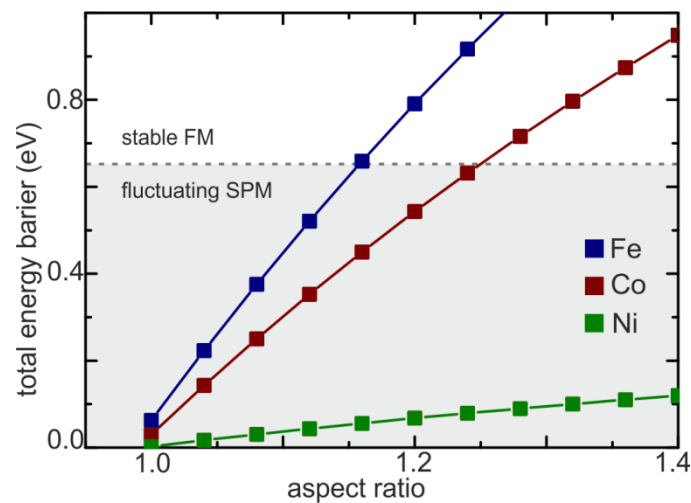FIGURE 8.3. Total anisotropy (MCA + shape anisotropy) energy barrier for a prolate ellipsoid Fe, Co and Ni particle as a function of the aspect ratio starting from a perfect 12 nm diameter sphere. Adapted from [62].

Note that the shape anisotropy contribution is very similar for Fe and Co particles, but much smaller for Ni due to the smaller magnetization. This situation is different when considering the magneto-elastic contributions, cf. Fig. 8.4. Here Ni and Co show a similarly large effect, while Fe shows a much smaller contribution, because of magnetoelastic coefficients. For example, in the case of 12 nm diameter particles (cf. Fig. 8.4), Co and Ni particles will need a homogeneous strain of 0.3 % to show magnetic contrast at room temperature, while Fe particles will need a strain three times larger. However, since the elastic energies needed to maintain such strains are of order of hundred eV, we conclude that it is unlikely that strain is the origin of the enhanced MA of the Fe and Co nanoparticles.
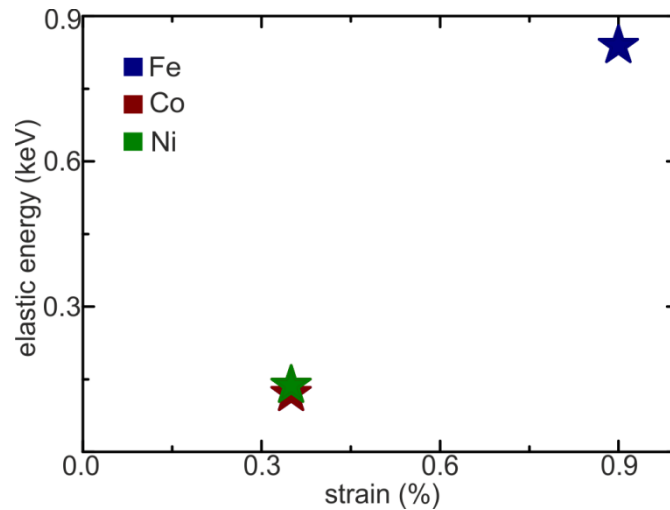
FIGURE 8.4. Elastic energy needed to maintain a strain to show stable FM state a RT in a Fe, Co and Ni particle of 12 nm diameter. Adapted from [62].

Since these different properties described above are not related either with the crystallographic structure (same behavior in bcc Fe and fcc Co), nor with the element and different MAE (Fe, Co and Ni), nor with strain (different behavior for same values of Co and Ni particles), and nor to the size of the particle (from 8 to 20 nm), we conclude that the origin of the high anisotropy state in Co and Fe is probably associated with a meta-stable structural state due to the presence of local defects within the NPs. Such defects might either be dislocations or defects associated with the NP-substrate interface, which are strong enough to

cause ferromagnetic states in case of iron and cobalt nanoparticles, but not in the case of nickel.

In summary, the co-existence of two distinct classes of magnetic behavior, magnetically blocked (which may be related to a meta-stable structural state in the nanoparticle) and superparamagnetic nanoparticles, irrespective of their size, is found to occur in bcc Fe nanoparticles and fcc Co nanoparticles but not in fcc Ni nanoparticles. Given the assertion that the meta-stable structural state responsible for the anomalous ferromagnetic behavior is due to defect content within the nanoparticles, this result suggests that the existence of such defects is independent of the bcc and fcc crystallographic structure. That ferromagnetic particles are not observed for fcc Ni need not suggest an absence of defect structures within the Ni nanoparticles, but rather an insensitivity of its magnetic properties to the defect – a proposition which is not incompatible with Ni being a "hard" ferromagnetic when compared to both Fe and Co.

As shown in Chapter 7, the high anisotropy state in Fe NPs deposited on Si substrate is related with interface effects since Fe NPs deposited on W(110) are SPM for any of the two perpendicular directions W[$1\bar{1}0$] and W[001], as expected considering bulk like anisotropy. In addition badly-shaped Fe particles deposited on W(110) are also SPM, which means that we can exclude that the shape anispotropy is the responsible factor for ferromagnetism in these particles.

Moreover, our results show that interpretation of ensemble measurements needs particular care, even when performing *in situ* studies of mono-dispersed nanoparticle samples with high chemical purity and deposited on a chemically inert substrate. Besides the variation in shape, particles of similar size can show significantly different magnetic properties or simply not obey expected scaling behaviors. The badly-shaped particles might possess significantly different properties compared to well-shaped particles and may contribute in a complex manner to ensemble measurements, an aspect that will merit further work.

Appendix 1

Arrhenius prefactor

The attempt frequency prefactor v_0 depends on the temperature, the nanoparticle's magnetic moment $V \cdot M_s(T)$ (with V being the particle volume), and the nature of the MAE (cubic or uniaxial) as discussed in Refs. [52] and [50]. In the following, the attempt frequency and energy barriers required by spherical nanoparticles to yield $\tau = \tau_{\exp} = 20\,\mathrm{s}$ at room temperature are calculated for 20 nm Fe, Co and Ni particles. These are the minimum energy barriers required to observe magnetically blocked states in our experiments.

For *uniaxial anisotropy* systems, the attempt frequency prefactor

$$\upsilon_0 = \frac{2k_B T \gamma \alpha}{VM_S(1+\alpha^2)\sqrt{\pi}}\left(\frac{E_m}{k_B T}\right)^{3/2} = \frac{2\gamma\alpha}{VM_S(1+\alpha^2)\sqrt{\pi k_B T}}\left(E_m\right)^{3/2}, \text{ with } \alpha \text{ the damping factor}$$

and γ the gyromagnetic ratio, depends on the temperature directly through $\dfrac{1}{\sqrt{T}}$ term, and indirectly through the magnetization and anisotropy, which are also temperature dependent.

In the case of *cubic anisotropy* (with $K_C > 0$) a relation for the attempt frequency used by Coffey in Ref. [52] in the case of $\alpha \geq 1$ is $\upsilon_0 = \dfrac{4\sqrt{2}E_m(\alpha + \sqrt{9\alpha + 8})\gamma}{M_S V(1+\alpha^2)\pi}$

and for *cubic anisotropy* (with $K_C < 0$) $\upsilon_0 = \dfrac{4\sqrt{2}E_m(\alpha + \sqrt{9\alpha + 8} - \alpha)\gamma}{M_S V(1+\alpha^2)\pi}$ is considered.

The particle magnetization temperature dependence can be modeled to first order as follows:

$$M_S(T) = M_S(T=0)\sqrt{1-\frac{T}{T_C}} = M_0\sqrt{1-\frac{T}{T_C}} \text{ where } T_C \text{ is the Curie temperature.}$$

The temperature dependence of the anisotropy is not considered, because the anisotropy values used in the calculation correspond to room temperature.

Since experimentally it was observed that Fe nanoparticles switch clearly between two opposite states with positive and negative XMCD contrast, indicating a dominant uniaxial anisotropy contribution, in the case of Fe particles a uniaxial case was also considered. The attempt frequencies at room temperature for spherical particles with a diameter of 20 nm, using the bulk values for the material parameter of Fe, Co and Ni, are presented in Table 1. The values of the attempt frequencies are similar for cubic Fe, Co and Ni.

Material	Uniaxial type	Cubic (K>0)	Cubic (K<0)
Fe	2.1×10^{10} Hz	6.3×10^{9} Hz	
Co			1.9×10^{9} Hz
Ni			0.46×10^{9} Hz

Table 1. The attempt frequency (at room temperature) for spherical nanoparticles with D=20 nm.

Material	Crystal structure	Lattice parameter (nm)	Magnetic moment (μ_B/atom)	Number of spins	Curie temperature (K)	Anisotropy constant (μeV/atom)
Fe	bcc	0.287	2.17	354669	1044	3.3
Co	fcc	0.355	1.72	375381	1403	-3.8
Ni	fcc	0.352	0.6	383913	631	-0.28

Table 2. Lattice parameter, magnetic moment, Curie temperature, anisotropy constant and number of spins used to simulate the energy barriers in case of 20 nm Fe, Co, and Ni.

Using the values from Table 2, the energy barriers required to satisfy the condition that the relaxation time equals the experimental time $t_{exp} = 20\,\text{s}$, is given by the following expressions:

- Uniaxial case:

$$\tau_u = \frac{VM_S(T)(1+\alpha^2)\sqrt{\pi k_B T}}{2\gamma\alpha(E_m)^{3/2}}\,e^{E_m/k_B T}$$

- Cubic (K>0) case:

$$\tau_c = \frac{VM_S(T)(1+\alpha^2)\pi}{4\sqrt{2}E_m(\sqrt{9\alpha+8}+\alpha)\gamma}e^{E_m/k_BT}$$

- Cubic (K<0) case:

$$\tau_c = \frac{VM_S(T)(1+\alpha^2)\pi}{4\sqrt{2}E_m(\sqrt{9\alpha+8}-\alpha)\gamma}e^{E_m/k_BT}$$

The corresponding values are shown in Table 3.

Material	Uniaxial type	Cubic (K>0)	Cubic (K<0)
Fe	0.67 eV	0.68 eV	
Co			0.67 eV
Ni			0.7 eV

Table 3. Simulated energy barrier required for a 20 nm particles to be ferromagnetic at RT, for $\tau_c = \tau_{exp} = 20\,\text{s}$ and a damping of $\alpha = 1.0$.

As shown in Table 3, the energy barriers that the particles require to exhibit a magnetic blocked behavior at room temperature are very similar for Fe, Co and Ni, of about 0.7 eV.

References

[1]   G. Prinz and K. Hathaway, Phys. Today **48**, 24 (1995).

[2]   P. Grünberg, Phys. Today **54**, 31 (2001).

[3]   G. A. Prinz, Science **282**, 1660 (1998).

[4]   F. J. Himpsel, J. E. Ortega, G. J. Mankey, and R. F. Willis, Adv. Phys. **47**, 511 (1998).

[5]   J. L. Dormann, D. Fiorani, and E. Tronc, Adv. Chem. Phys. **98**, 283 (1997).

[6]   J. Bansmann, S. H. Baker, C. Binns, J. A. Blackman, J.-P. Bucher, J. Dorantes-Dávila, V. Dupuis, L. Favre, D. Kechrakos, A. Kleibert, K.-H. Meiwes-Broer, G. M. Pastor, A. Perez, O. Toulemonde, K. N. Trohidou, J. Tuaillon, and Y. Xie, Surf. Sci. Rep. **56**, 189 (2005).

[7]   A.-H. Lu, E. L. Salabas, and F. Schuth, Angew. Chem. Int. Ed. **46**, 1222 (2007).

[8]   S. H. Sun, C. B. Murray, D. Weller, L. Folks, and A. Moser, Science **287**, 1989 (2000).

[9]   V. Skumryev, S. Stoyanov, Y. Zhang, G. Hadjipanayis, D. Givord, and J. Nogues, Nature (London) **423**, 850 (2003).

[10]   M. Jamet, W. Wernsdorfer, C. Thirion, V. Dupuis, P. Mélinon, A. Pérez, and D. Mailly, Phys. Rev. B **69**, 024401 (2004).

[11]   M. Ruano, M. Diaz, L. Martinez, E. Navarro, E. Roman, M. Garcia-Hernandez, A. Espinosa, C. Ballesteros, R. Fermento, and Y. Huttel, Phys. Chem. Chem. Phys. **15**, 316 (2013).

[12]   S. Rohart, V. Repain, A. Tejeda, P. Ohresser, F. Scheurer, P. Bencok, J. Ferré, and S. Rousset, Phys. Rev. B **73**, 165412 (2006).

[13]   S. A. Majetich and Y. Jin, Science **284**, 470 (1999).

[14]   W. Wernsdorfer, E. B. Orozco, K. Hasselbach, A. Benoit, B. Barbara, N. Demoncy, A. Loiseau, H. Pascard, and D. Mailly, Phys. Rev. Lett. **78**, 1791 (1997).

[15]   M. Varon, M. Beleggia, T. Kasama, R. J. Harrison, R. E. Dunin-Borkowski, V. F. Puntes, and C. Frandsen, Sci. Rep. **3**, 1234 (2013).

[16]   J. Rockenberger, F. Nolting, J. Lüning, J. Hu, and A. P. Alivisatos, J. Chem. Phys. **116**, 6322 (2002).

[17]   A. Fraile Rodríguez, A. Kleibert, J. Bansmann, A. Voitkans, L. J. Heyderman, and F. Nolting, Phys. Rev. Lett. **104**, 127201 (2010).

[18]   A. Balan, P. M. Derlet, A. F. Rodríguez, J. Bansmann, R. Yanes, U. Nowak, A. Kleibert, and F. Nolting, Phys. Rev. Lett. **112**, 107201 (2014).

[19]   C. Sun, J. S. Lee, and M. Zhang, Advanced drug delivery reviews **60**, 1252 (2008).

[20]   L. M. Parkes, R. Hodgson, T. Lu le, D. Tung le, I. Robinson, D. G. Fernig, and N. T. Thanh, Contrast media & molecular imaging **3**, 150 (2008).

[21]   C. Binns, M. Maher, Q. Pankhurst, D. Kechrakos, and K. Trohidou, Physical Review B **66**, 184413 (2002).

[22]   C. T. Black, Science **290**, 1131 (2000).

[23]   C. Antoniak *et al.*, Nature communications **2**, 1 (2011).

[24]   Andreas Moser and D. T. M. Kentaro Takano, Manfred Albrecht, Yoshiaki Sonobe, Yoshihiro Ikeda, Shouheng Sun and Eric E Fullerton, J. Phys. D: Appl. Phys. **35**, R157 (2002).

[25]   J. Y. Bigot, H. Kesserwan, V. Halte, O. Ersen, M. S. Moldovan, T. H. Kim, J. T. Jang, and J. Cheon, Nano letters **12**, 1189 (2012).

[26]   C. b. Rong, D. Li, V. Nandwana, N. Poudyal, Y. Ding, Z. L. Wang, H. Zeng, and J. P. Liu, Advanced Materials **18**, 2984 (2006).

[27]   A. Farhan, P. M. Derlet, A. Kleibert, A. Balan, R. V. Chopdekar, M. Wyss, L. Anghinolfi, F. Nolting, and L. Heyderman, Nature Physics, 375 (2013).

[28]   S. Blundell, *Magnetism in Condensed Matter* (OUP Oxford, 2001).

[29]   A. Aharoni, *Introduction to the Theory of Ferromagnetism* (Oxford University Press, 2000).

[30]   P. Bruno, in *Ferienkurse des Forschungszentrums Julich*, p. 24.15.

[31]   S. Chikazumi and C. D. Graham, *Physics of Ferromagnetism* (Clarendon Press, 1997).

[32]   C. A. F. Vaz, J. A. C. Bland, and G. Lauhoff, Rep. Prog. Phys. **71**, 056501 (2008).

[33]   D. Garanin and H. Kachkachi, Phys. Rev. Lett. **90**, 065504 (2003).

[34]   Y. Labaye, O. Crisan, L. Berger, J. M. Greneche, and J. M. D. Coey, Journal of Applied Physics **91**, 8715 (2002).

[35]   L. Neel, J. Phys. Radium **15**, 376 (1954).

[36]   R. Yanes, O. Chubykalo-Fesenko, H. Kachkachi, D. A. Garanin, R. Evans, and R. W. Chantrell, Phys. Rev. B **76**, 064416 (2007).

[37]   M. Beleggia, M. De Graef, and Y. Millev, Philos. Mag. **86**, 2451 (2006).

[38]   F. Garcia-Sanchez and O. Chubykalo-Fesenko, Appl. Phys. Lett. **93**, 192508 (2008).

[39]   C. Kittel, Rev. Mod. Phys. **21**, 541 (1949).

[40]   A. Hubert and R. Schäfer, *Magnetic Domains: The Analysis of Magnetic Microstructures* (Springer, Berlin, 1998).

[41]   A. Kleibert and F. Nolting, Physik Journal **06**, 27 (2013).

[42]   J. Frenkel and J. Dorfman, Nature (London) **126**, 274 (1930).

[43]   C. Kittel, Phys. Rev. **70**, 965 (1946).

[44]   R. C. O'Handley, *Modern Magnetic Materials: Principles and Applications* (Wiley-Interscience, 1999).

[45]   M. Bode, O. Pietzsch, A. Kubetzka, and R. Wiesendanger, Physical Review Letters **92**, 067201 (2004).

[46]   S. Krause, G. Herzog, T. Stapelfeldt, L. Berbil-Bautista, M. Bode, E. Vedmedenko, and R. Wiesendanger, Physical Review Letters **103**, 127202 (2009).

[47]   W. Brown, Phys. Rev. **130**, 1677 (1963).

[48]   E. C. Stoner and E. P. Wohlfarth, Philos. Trans. R. Soc. London **240**, 599 (1948).

[49]   I. Eisenstein and A. Aharoni, Phys. Rev. B **16**, 1278 (1977).

[50]   U. Nowak, O. N. Mryasov, R. Wieser, K. Guslienko, and R. W. Chantrell, Phys. Rev. B **72**, 172410 (2005).

[51]   L. Néel, Ann. Geophys. **5**, 99 (1949).

[52]   W. T. Coffey and Y. P. Kalmykov, J. Appl. Phys. **112**, 121301 (2012).

[53]   A. Fraile Rodríguez, A. Kleibert, J. Bansmann, and F. Nolting, J. Phys. D: Appl. Phys. **43**, 474006 (2010).

[54]   A. Kleibert, J. Passig, K. H. Meiwes-Broer, M. Getzlaff, and J. Bansmann, J. Appl. Phys. **101**, 114318 (2007).

[55]   A. Kleibert, *Doctoral thesis "Massengefilterte Eisennanopartikel auf ultradünnen Kobaltfilmen – eine in situ Studie mit weicher Röntgenstrhlung"* (Universität Rostock, 2005).

[56]   A. Kleibert, A. Voitkans, and K. H. Meiwes-Broer, Phys. Rev. B **81**, 073412 (2010).

[57]   H. Haberland, Z. Insepov, and M. Moseler, Phys. Rev. B **51**, 11061 (1995).

[58]   V. N. Popok, I. Barke, E. E. B. Campbell, and K.-H. Meiwes-Broer, Surf. Sci. Rep. **66**, 347 (2011).

[59]   https://www.uantwerpen.be/en/rg/emat/research/instrumentation/.

[60]   A. Ichimiya and P. I. Cohen, *Reflection High Energy Electron Diffraction* (Cambridge University Press, 2004).

110

[61]   J. E. Mahan, K. M. Geib, G. Y. Robinson, and R. G. Long J. Vac. Sci. Technol. A **8**, 3692 (1990).

[62]   A. Balan, R. Yanes, A. Fraile Rodríguez, P. M. Derlet, R. S. Dhaka, M. Radovic, U. Nowack, A. Kleibert, and F. Nolting, submitted (2014).

[63]   H. Hövel and I. Barke, Prog. Surf. Sci. **81**, 53 (2006).

[64]   A. Kleibert, F. Bulut, R. K. Gebhardt, W. Rosellen, D. Sudfeld, J. Passsig, J. Bansmann, K. H. Meiwes-Broer, and M. Getzlaff, J. Phys.: Condens. Matter **20**, 445005 (2008).

[65]   C. Quitmann, U. Flechsig, L. Patthey, T. Schmidt, G. Ingold, M. Howells, M. Janousch, and R. Abela, Surf Sci. **480**, 173 (2001).

[66]   U. Flechsig *et al.*, AIP Conf. Proc. **1234**, 319 (2010).

[67]   J. Stöhr, *NEXAFS spectroscopy* (Springer, Berlin, 1992), Vol. 25.

[68]   J. Stöhr and H. Siegmann, *Magnetism - From Fundamentals to Nanoscale Dynamics* (2006), Vol. 152, Springer Series in Solid-state sciences.

[69]   E. Beaurepaire, H. Bulou, F. Scheurer, and J.-P. Kappler, *Magnetism and Synchrotron Radiation* (2009), Vol. 133, Springer Proceedings in Physics.

[70]   D. C. Koningsberger and R. Prins, *X-ray absorption: principles, applications, techniques of EXAFS, SEXAFS, and XANES* (John Wiley and Sons, New York, 1988), Vol. 60, No. 14.

[71]   J. Stöhr, H. A. Padmore, S. Anders, T. Stammler, and M. R. Scheinfein, Surface Review and Letters **05**, 1297 (1998).

[72]   R. Nakajima, J. Stöhr, and Y. U. Idzerda, Physical Review B **59**, 6421 (1999).

[73]   J. Stöhr, Y. Wu, B. D. Hermsmeier, M. G. Samant, G. R. Harp, S. Koranda, D. Dunham, and B. P. Tonner, Science **259**, 685 (1993).

[74]   B. P. Tonner and G. R. Harp, Rev. Sci. Instrum. **59**, 853 (1988).

[75]   E. Bauer, Journal of Electron Spectroscopy and Related Phenomena **185**, 314 (2012).

[76]   L. Le Guyader, A. Kleibert, A. Fraile Rodríguez, S. El Moussaoui, A. Balan, M. Buzzi, J. Raabe, and F. Nolting, J. Electron Spectrosc. Relat. Phenom. **185**, 371 (2012).

[77]   E. Mengotti, ETH Zurich, 2010.

[78]   A. Kleibert, K. H. Meiwes-Broer, and J. Bansmann, Phys. Rev. B **79**, 125423 (2009).

[79]   J. Carvell, E. Ayieta, A. Gavrin, R. Cheng, V. R. Shah, and P. Sokol, J. Appl. Phys. **107**, 103913 (2010).

[80]   D. L. Peng, T. Hihara, K. Sumiyama, and H. Morikawa, J. Appl. Phys. **92**, 3075 (2002).

[81]   J. Pierce, M. Torija, Z. Gai, J. Shi, T. Schulthess, G. Farnan, J. Wendelken, E. Plummer, and J. Shen, Phys. Rev. Lett. **92**, 237201 (2004).

[82]   F. Kronast, N. Friedenberger, K. Ollefs, S. Gliga, L. Tati-Bismaths, R. Thies, A. Ney, R. Weber, C. Hassel, F. M. Römer, A. V. Trunova, C. Wirtz, R. Hertel, H. A. Dürr, and M. Farle, Nano Lett. **11**, 1710 (2011).

[83]   F. Bødker, S. Mørup, and S. Linderoth, Phys. Rev. Lett. **72**, 282 (1994).

[84]   A. V. Trunova, R. Meckenstock, I. Barsukov, C. Hassel, O. Margeat, M. Spasova, J. Lindner, and M. Farle, J. Appl. Phys. **104**, 093904 (2008).

[85]   T. Burkert, O. Eriksson, P. James, S. Simak, B. Johansson, and L. Nordström, Physical Review B **69**, 104426 (2004).

[86]   M. A. Pfeifer, G. J. Williams, I. A. Vartanyants, R. Harder, and I. K. Robinson, Nature (London) **442**, 63 (2006).

[87]   T. Järvi, A. Kuronen, K. Meinander, K. Nordlund, and K. Albe, Physical Review B **75**, 115422 (2007).

[88]   D. L. Huber, Small **1**, 482 (2005).

[89]   Gangopadhyay S., Hadjipanayis G. C., Dale B., Sorensen C. M., Klabunde K. J., Papaefthymiou V., and A. Kostikas, Phys. Rev. B **45**, 9778 (1992).

[90]   A. Pratt, L. Lari, O. Hovorka, A. Shah, C. Woffinden, S. P. Tear, C. Binns, and R. Kroger, Nat. Mater. **13**, 26 (2013).

[91]   T. Vystavel, G. Palasantzas, S. A. Koch, and J. T. M. De Hosson, Appl. Phys. Lett. **82**, 197 (2003).

[92]   G. V. Wulff, Z. Kristallogr. **34**, 449 (1901).

[93]   S. H. Baker, M. Roy, S. J. Gurman, S. Louch, A. Bleloch, and C. Binns, Journal of Physics: Condensed Matter **16**, 7813 (2004).

[94]   F. Dumestre, B. Chaudret, A. Amiens, P. Renaud, and P. Fejes, Science **303**, 821 (2004).

[95]   N. Lümmen and T. Kraska, Phys. Rev. B **71**, 205403 (2005).

[96]   F. Baletto and R. Ferrando, Rev. Mod. Phys. **77**, 371 (2005).

[97]   http://cms.uni-konstanz.de/physik/nowak/.

[98]   H. Kachkachi and E. Bonet, Phys. Rev. B **73**, 224402 (2006).

[99]   L. Vitos, A.V. Ruban, H. L. Skriver, and J. Kollár, Surf Sci. **411**, 186 (1998).

[100]   D. Pomfret and M. Prutton, Phys stat sol (a) **19**, 423 (1973).

[101]   P. M. Dinh, P.-G. Reinhard, and E. Suraud, Phys. Rep. **485**, 43 (2010).

[102]   R. Kläsges, C. Carbone, W. Eberhardt, C. Pampuch, O. Rader, T. Kachel, and W. Gudat, Physical Review B **56**, 10801 (1997).

[103]   I. I. Pronin, M. V. Gomoyunova, D. E. Malygin, D. V. Vyalikh, Y. S. Dedkov, and S. L. Molodtsov, Journal of Applied Physics **104**, 104914 (2008).

[104]   C. A. F. Vaz, A. Balan, F. Nolting, and A. Kleibert, Phys Chem Chem Phys, submitted (2014).

[105]   O. Kitakami, H. Sato, Y. Shimada, F. Sato, and M. Tanaka, Phys. Rev. B **56**, 13849 (1997).

[106]   V. F. Puntes, K. M. Krishnan, and A. P. Alivisatos, Science **291**, 2115 (2001).

[107]   J. Bansmann, M. Getzlaff, A. Kleibert, F. Bulut, R. K. Gebhardt, and K.-H. Meiwes-Broer, Appl. Phys. A **82**, 73 (2006).

[108]   K. Sell, A. Kleibert, V. v. Oeynhausen, and K.-H. Meiwes-Broer, Eur. Phys. J. D **45**, 433 (2007).

[109]   A. Kleibert, A. Voitkans, and K.-H. Meiwes-Broer, physica status solidi (b) **247**, 1048 (2010).

Publications

- Balan, P. M. Derlet, R. Dhaka, M. Radovic, A. Fraile Rodríguez, R. Yanes, U. Nowak, A. Kleibert, F. Nolting, "Magnetic and structural properties of 3d transition metal nanoparticles upon deposition onto a non-magnetic substrate", *submitted*.

- C. A. Vaz, A. Balan, F. Nolting and A. Kleibert, "*In situ* magnetic and electronic investigation of the early stage oxidation of Fe nanoparticles using X-ray photo-emission microscopy", *Phys. Chem. Chem. Phys. 10.1039/c4cp02725f (2014)*.

- A. Kleibert, A. Balan, A. Fraile Rodríguez, F. Nolting, " Investigating individual $Fe_{50}Co_{50}$ alloy nanoparticles using x-ray photo-emission electron microscopy", *J. Phys.: Conf. Ser. 521 012003 (2014)*.

- A. Farhan, A. Kleibert, P. Derlet, L. Anghinol, A. Balan, R. Chopdekar, M. Wyss, S. Gliga, F. Nolting, L. J. Heyderman, "Thermally induced magnetic relaxation in building blocks of artificial kagome spin ice", *Phys. Rev. B 89, 214405 (2014)*.

- V. Kapaklis, U. B. Arnalds, A. Farhan, R. V. Chopdekar, A. Balan, A. Scholl, L. J. Heyderman and B. Hjorvarsson, "Thermal fluctuations in artificial spin ice", *Nature Nanotechnology , 10.1038/nnano.2014.104 (2014)*.

- A. Balan, P. M. Derlet, A. Fraile Rodríguez, J. Bansmann, R. Yanes, U. Nowak, A. Kleibert, F. Nolting, "Direct observation of magnetic metastability in iron nanoparticles", *Physical Review Letters 112, 107201 (2014)*.

- A. Farhan, P.M. Derlet, A. Kleibert, A. Balan, R. Chopdekar, A. Wyss, J. Perron, A. Scholl, F. Nolting, L.J. Heyderman, " Direct Observation of Thermal Relaxation in Artificial Spin Ice", *Physical Review Letters 111, 057204 (2013)*.

- A. Farhan, P. Derlet, A. Kleibert, A. Balan, R. Chopdekar, M. Wyss, L. Anghinolfi, F. Nolting, L.J. Heyderman, "Exploring hyper-cubic energy landscapes in thermally active finite artificial spin-ice systems", *Nature Physics 9, 375-382 (2013)*.

- L. Le Guyader, A. Kleibert, A. Fraile Rodriguez, S. El Moussaoui, A. Balan, M. Buzzi, J. Raabe, F. Nolting, "Studying nanomagnets and magnetic heterostructures with X-ray PEEM at the Swiss Light Source ", *Journal of electron spectroscopy and related phenomena 185, 371-380 (2012)*.

- A. Unnar, A. Farhan, R. Chopdekar, V. Kapaklis, A. Balan, E. Papaioannou, M. Ahlberg, F. Nolting, L. Heyderman,B. Hjorvarsson, "Thermalized ground state of artificial kagome spin ice building blocks", *Applied Physics Letters 101, 112404 (2012)*.

Curriculum Vitae

Personal information:

Name: Ana-Maria BALAN

Date of birth: 19/01/1986

Nationality: Romanian

Education:

09/2010-09/2014 **Doctoral Studies**

Experimental Physics, Basel University, 4003 Basel, Switzerland
Microscopy and Magnetism Group, Swiss Light Source, Paul Scherrer Institute, 5232 Villigen, Switzerland
Thesis: "Studying individual magnetic nanoparticles with X-ray PEEM"

09/2008-07/2010 **Master Studies**

Modelling and Simulation, Faculty of Physics, Alexandru Ioan Cuza University of Iaşi, 700506 Iaşi, Romania
Thesis: „Studying the effect of interactions in ferromagnetic micro and nano systems"

09/2004-07/2008 **Bachelor Studies**

Physics, Faculty of Physics, Alexandru Ioan Cuza University of Iaşi, 700506 Iaşi, Romania
Thesis: „Preisach – Neel type models to model the magnetization"